RICE UNIVERSITY

Measurement of the W$\gamma \to \mu\nu\gamma$ Cross Section, Limits on Anomalous Trilinear Vector Boson Couplings, and the Radiation Amplitude Zero in $p\overline{p}$ Collisions at $\sqrt{s} = 1.96$ TeV.

by

Andrew W. Askew

A Thesis Submitted
in Partial Fulfillment of the
Requirements for the Degree

Doctor of Philosophy

Approved, Thesis Committee:

B. Paul Padley, Chair
Professor of Physics and Astronomy

Hannu E. Miettinen
Professor of Physics and Astronomy

David Scott
Professor of Statistics

Houston, Texas

November, 2004

ABSTRACT

Measurement of the W$\gamma \rightarrow \mu\nu\gamma$ Cross Section, Limits on Anomalous Trilinear Vector Boson Couplings, and the Radiation Amplitude Zero in $p\overline{p}$ Collisions at $\sqrt{s} = 1.96$ TeV.

by

Andrew W. Askew

This thesis details the measurement of the $p\overline{p}\rightarrow$ W $\gamma + X \rightarrow \mu\nu\gamma + X$ cross section at $\sqrt{s}$ = 1.96 TeV using the DØ detector at Fermilab, in 134.5 pb^{-1} of integrated luminosity. From the photon E_T spectrum limits on anomalous couplings of the photon to the W are obtained. At 95% confidence level, limits of -1.05 $<\Delta\kappa <$ 1.04 for λ=0 and -0.28 $< \lambda <$ 0.27 for $\Delta\kappa$=0 are obtained on the anomalous coupling parameters. The charge signed rapidity difference from the data is displayed, and its significance discussed.

Contents

List of Figures

List of Tables

Chapter 1
Introduction

1.1 Overview of the Standard Model

The Standard Model of Particle physics is a detailed description of the interaction between the fundamental particles of nature. With the inclusion of neutrino masses and mixing parameters, its predictions agree with all experiments to date.

The Standard Model states that there are only two types of particles in nature, fermions and bosons. Fermions have half-integer spins, and make up all the matter in the universe. Bosons have integer spins and mediate the fundamental forces through their emission and absorption by fermions. Gravity is not included in the Standard Model, the model describes only the interaction of the strong, weak, and electromagnetic forces.

Fermions are divided into two families, leptons and quarks, which are each separated into three generations. Tau leptons, muons, and electrons only interact through the electromagnetic and weak forces. Each charged lepton has a corresponding neutrino, which only interacts through the weak force. Table 1.1 shows the three lepton families and their properties.

Table 1.2 shows the Standard Model quarks, with their corresponding properties. Quarks possess an additional internal degree of freedom called color. Color charge affects how quarks interact with one another through the strong force, which

Lepton	Mass [MeV/c^2]	Charge [e]	Lifetime
e	0.5110	-1	$>4.2\times10^{24} yr$
ν_e	$< 15 \cdot 10^{-6}$	0	
μ	105.7	-1	$2.2\times10^{-6} s$
ν_μ	< 0.17	0	
τ	1777	-1	$2.9\times10^{-13} s$
ν_τ	< 24	0	

Table 1.1 Fundamental fermions in the Standard Model: leptons.

is described by Quantum Chromodynamics (QCD).

To date no particle with a net color has been observed. This is due to the non-Abelian nature of the strong force (*i.e.* the gluons mediating the strong force interact with each other as well as with the quarks). In QCD, this results in an increase of strength with distance. An example of this is found in quark production at colliders. At large inter-quark distances it becomes energetically favorable to create a quark-antiquark pair. The newly created pair continues on its way and interacts with the original quark pair, generating additional quarks. This 'fragmentation' process continues until the kinetic energy of the original pair of quarks has been used to create clusters of quarks, with no net color and low internal momentum. The strong color coupling then turns these clusters into hadrons. Thus the original pair of quarks has resulted in two 'jets' of particles, each with the original momentum of the initial quarks, but with no net color [1].

The process $q\overline{q} \rightarrow q\overline{q}$ accounts for a large number of the interactions at a hadron

collider. Due to the different ways the resultant quarks may hadronize, almost all smaller cross section processes can be mimicked by the jets of particles from quark hadronization. Differentiating between these jets and other particle signatures (photons, electrons, muons,*etc.*) is a key part of most analyses (at hadron colliders).

Quark	Mass [GeV/c^2]	Charge [e]
u	2–8 $\cdot 10^{-3}$	2/3
d	5–15 $\cdot 10^{-3}$	-1/3
c	1.0–1.6	2/3
s	0.1–0.3	-1/3
t	180	2/3
b	4.1–4.5	-1/3

Table 1.2 Fundamental fermions in the Standard Model: quarks.

The integer spin bosons mediate the Standard Model forces. The fermions interact with each other through exchange of these particles. Quantum Electrodynamics (QED) is an example of a description of a force in terms of a local gauge theory (electromagnetic interaction through exchange of photons). The weak interaction is also a gauge theory, but with one important difference: the mediating particles for the weak interaction possess large masses. The mass of the W and Z bosons are given by their interaction with the Higgs boson. The W boson also has charge, which means that it must also interact with photons. This is another example of the non-Abelian nature of the Standard Model. The properties of the Standard Model bosons are

summarized in Table 1.3.

Gauge boson	Mass [GeV/c^2]	Charge [e]
gluons	0	0
γ	0	0
$W^{\pm}$	80.42	± 1
Z^0	91.19	0

Table 1.3 Gauge bosons in the Standard Model.

Interaction with the Higgs boson is required, in the Standard Model, to give the W and Z bosons their masses. This has the benefit of making the theory renormalizable. It is assumed that interaction with the Higgs is also responsible for all the other Standard Model particle masses. Mass limits have been set on the Higgs in collider experiments, but there is no direct experimental evidence of the Higgs. The observation of the Higgs, along with the measurement of its mass will be an important test of the Standard Model.

1.2 Motivation for Study of Wγ

The Standard Model precisely predicts the details of Wγ interactions. Any deviation from this prediction would be evidence of physics beyond the Standard Model. For example, W boson compositeness would give rise to anomalous Wγ coupling.

Due to the gauge theory which forms the basis of the Standard Model, an interesting phenomena occurs when a photon may be attached to three separate particle legs of a Feynman diagram at tree level. The portion of the matrix element dealing with

charge, and the portion dealing with polarization factorize, leading to an angular zero in the production cross section. This is known as a radiation amplitude zero (RAZ). In Wγ, the three tree level diagrams* meet this criteria. This behavior has not yet been observed. It is interesting to note that these radiation zeroes occur in other processes (since this is a general consequence of the theory), but rarely in a physical portion of phase space.

The Wγ coupling has been studied before, both at LEP and in Run I at the Fermilab Tevatron. At LEP, the coupling was studied through W pair production, single W production, and single photon production. LEP had the advantage of a very clean experimental environment†. However, W pair production and single W production have additional diagrams that include WWZ couplings, and thus do not solely probe the WWγ coupling. Single photon production directly probes the WWγ coupling but occurs at a much lower rate, and thus was not as well characterized. At Fermilab, the production process may be studied directly, through the production of a W in association with a photon. In Run I, the DØ detector lacked charge discrimination for electrons which is required to properly combine W^+ and W^- for the radiation amplitude zero. The upgrade for Run II resolved this issue. Also the higher integrated luminosity of Run II will allow for not only better anomalous

*In the tree level diagrams for Wγ there are two in which the photon is radiated from the initial quarks, and one in which the photon is radiated from the W. See Figure 2.1.

†e^+e^- experiments are cleaner environments in general since there is no underlying event. Underlying event refers to the additional 'wreckage' of initial protons at hadron colliders.

coupling limits, but better measurement of the other kinematic parameters of Wγ production.

Chapter 2
Theory of $W\gamma$

2.1 Standard Model $W\gamma$ Production

The Standard Model predicts the cross section and kinematic properties of Wγ production. At a $p\overline{p}$ collider, a W may be produced in association with a photon as shown in the three Feynman diagrams in Figure 2.1. The upper two diagrams are initial state radiation (ISR), where the photon is radiated from the initial state quarks. The lower contains the trilinear gauge boson vertex. In this diagram the quark and anti-quark annihilate to produce a virtual W boson which then radiates a photon to become a real W boson.

In addition to these three 'production' diagrams, the photon may also be radiated from the final state lepton, in our case the muon. In general, all four of these leading order processes are included in the measurement of the cross section for Wγ production.

2.1.1 Wγ Coupling

In the Standard Model, the electroweak interaction is described by a Lagrange density (referred to as the Lagrangian) given by quantum field theory. In general, for

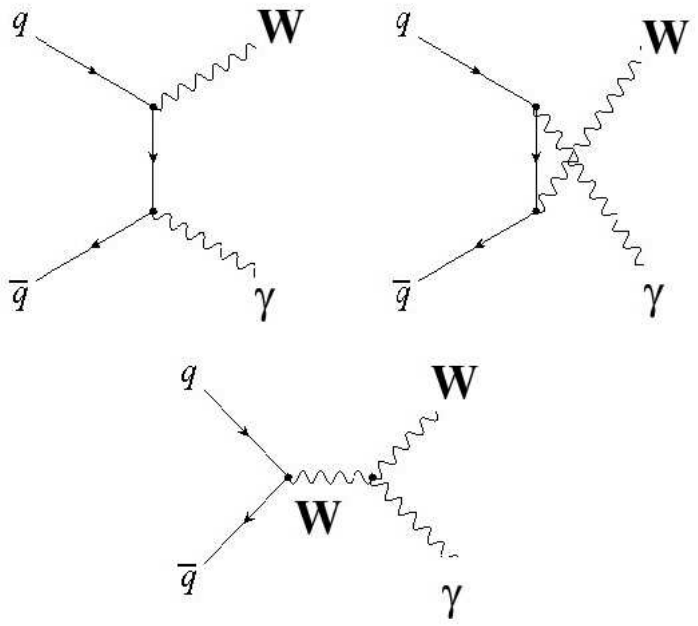

Figure 2.1 Wγ Standard Model Production Diagrams.

Wγ interactions, this Lagrangian may be written in the following way *:

$$\frac{L_{WW\gamma}}{g_{WW\gamma}} = g_\gamma(W^\dagger_{\mu\nu}W^\mu A^\nu - W^\dagger_\mu A_\nu W^{\mu\nu}) + \kappa_\gamma W^\dagger_\mu W_\nu F^{\mu\nu} + \frac{\lambda_\gamma}{M^2_W} W^\dagger_{\lambda\mu} W^\mu_\nu F^{\nu\lambda}. \quad (2.1)$$

A_ν is the photon field, and $W_{\mu\nu}$ is the non-Abelian weak field strength tensor:

$$W_{\mu\nu} = \partial_\mu W_\nu - \partial_\nu W_\mu - gW_\mu \times W_\nu, \quad (2.2)$$

where W_ν is the W field.

The Standard Model couplings correspond to $g_\gamma = \kappa_\gamma = 1$, and $\lambda_\gamma = 0$. Any observation of other values would be evidence for physics beyond the Standard Model.

*A general form of the Lagrangian for all possible couplings, as well as for arbitrary trilinear vector boson couplings, can be found in [2].

In general, since the Standard Model predicts that $\kappa = 1$, the Lagrangian is split into two parts: one containing only the predicted values and one containing only the 'extra' parts. Therefore couplings are expressed in terms of $\Delta\kappa$ and λ, both of which are zero in the Standard Model.

It is important to note that the three leading order Standard Model diagrams interfere such that the WWγ couplings are restricted to their gauge theory values at arbitrarily high center of mass energies. If anomalous couplings are introduced, the cancellation caused by this interference is ruined and the couplings are no longer restricted to their gauge theory values (and grow unphysically large). In order to introduce these couplings and still produce physical results, form factors of the following kind are introduced:

$$a(\hat{s}, q_W^2 = m_W^2, q_\gamma^2 = 0) = \frac{a_0}{(1 + \frac{\hat{s}}{\Lambda^2})^2}. \tag{2.3}$$

The parameter Λ may be interpreted as the energy at which new physics (not predicted in the Standard Model) interferes to maintain the tree level unitarity. a_0 is either λ or $\Delta\kappa$, as shown in Equation 2.1.

The presence of anomalous couplings not only increases the Wγ production cross section, but also changes the kinematic distributions of the process. In particular, anomalous couplings increase the likelihood of a high E_T photon being produced, compared to the Standard Model probability. Therefore the photon E_T spectrum may also be used for information about how the photon couples to the W boson.

2.1.2 The Radiation Amplitude Zero

As previously mentioned, the three amplitudes from the Feynman diagrams in Figure 2.1 interfere with one another. This interference is required to maintain tree level unitarity, but also introduces an angular dependence in the final state distribution of the photon and W. This is actually a consequence of the underlying gauge theory itself, when in a tree level diagram with three vector particles a photon line is added to each individually, the resultant amplitudes factorize into a term which contains all the charge dependence, and a term which involves all the polarization dependence [3]. Thus independent of the many polarization states of the system, there is a zero in the angular distribution between the incoming quark and outgoing W (ex. in the case of $\overline{u}d \rightarrow W^{-}\gamma$, the angle in question is between the incoming d quark and outgoing W^{-}).

It has been shown [4] that the amplitude for Wγ production can be cast into the form:

$$M = (\frac{Q_u}{t} + \frac{Q_d}{u})F(\sigma_i, \lambda_i, p_i), \tag{2.4}$$

where t and u are the Mandelstam variables*, Q_u and Q_d are the charges of the

*The Mandelstam variables are three quantities that are invariant under Lorentz transformations, for scattering of the form AB→CD. These are formed in the following way:

$$\begin{aligned} s &= (p_A + p_B)^2 \\ t &= (p_A - p_C)^2 \\ u &= (p_A - p_D)^2. \end{aligned} \tag{2.5}$$

Here, p_A, p_B, p_C, and p_D are the four-vectors corresponding to particles A, B, C and D respectively. It is conventional to use Mandelstam variables in expressions for amplitudes. In

respective quarks, and all other dependencies on the momentum, polarization and helicity are wrapped up in the function F. From this equation, one can see that the amplitude goes to zero for:

$$cos(\theta) = \frac{Q_d + Q_u}{Q_d - Q_u}. \tag{2.7}$$

Due to the fact that this angle is in the center of mass frame, it is difficult to disentangle at a hadron collider since the initial center of mass frame may not uniquely be reconstructed*. Thus it is advantageous to attempt to observe the angular dependence in some invariant quantity, for example the photon and lepton rapidity:

$$y = \frac{1}{2} ln \frac{E + p_z}{E - p_z}. \tag{2.8}$$

It has been shown [5] that the angular zero manifests itself in the rapidity difference between the photon and the W boson. Since this is dependent on the charge of the quarks (and thus the charge of the W), to combine both W^+ and W^- the rapidity difference must be signed by the charge of the W. In leptonic decays of the W, the

---

the center of mass frame, for massless quarks, the expressions for t and u can be written [4]:

$$t = -\frac{1}{2}(s - M_W^2)(1 - cos\theta)$$
$$u = -\frac{1}{2}(s - M_W^2)(1 + cos\theta). \tag{2.6}$$

*At hadron colliders, the hadronic decays of W bosons are difficult to distinguish from QCD jets. Thus, in general, only the leptonic decays of the W are considered (W$\rightarrow l\nu$). Since the neutrino is not observed, the center of mass frame may not be reconstructed (due to the ambiguity of the neutrino p_Z). See Section 2.2.

radiation amplitude zero may be measured in the rapidity difference between the photon and the final state lepton, since the rapidity of the lepton is correlated to the rapidity of the W. Specifically, the dip (there is an effect from the momentum fraction of the initial state partons which transforms the angular zero into a 'valley'), would occur at:

$$y(\gamma) - y(l) \approx -0.3. \tag{2.9}$$

The generator level (no resolution effects) Monte Carlo distribution for the charge signed photon lepton rapidity difference is shown in Figure 2.2.

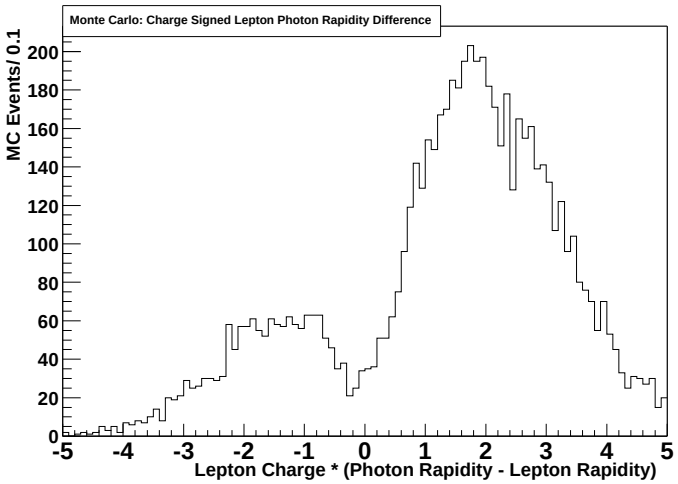

Figure 2.2 Charge Signed Lepton Photon Rapidity Difference from Monte Carlo.

2.2 Experimental Signature of Wγ

Since the energy of the colliding partons is not known precisely (due to the composite nature of the proton and the momentum distribution of the quarks within it),

the total energy in a given collision is not known. However, the momentum of the partons transverse to the proton (or anti-proton) direction is comparatively small, thus the energy (and momentum) transverse to the beam direction is used:

$$E_T = E \times sin\theta, \tag{2.10}$$

$$p_T = p \times sin\theta, \tag{2.11}$$

where E and p are the energy and momentum of the object in question, and θ is the polar angle (in a spherical-polar coordinate system) made with the beam axis (protons go in the positive z direction).

The transverse momentum at the interaction point is approximately zero, which implies that the transverse momentum of the particles produced in an interaction must sum to zero. W$\gamma \rightarrow \mu\nu\gamma$ events can be identified by searching for collisions in which there is a high transverse momentum muon, which passes through the calorimeter to be found in the outermost detector, the muon system. Next, an isolated (meaning from other calorimeter energies) electromagnetic signature in the calorimeter with no associated track is required. The neutrino will not be detected, but the energy carried away will cause a large imbalance in the measured transverse energy. This is known as missing transverse energy ($\not\!\!E_T$). This is expected for W$\gamma \rightarrow \mu\nu\gamma$, and thus a large missing transverse energy is required, representing the escape of the neutrino. The combination of the muon, photon and ($\not\!\!E_T$) leads to a distinctive experimental signature.

Even with such a clean experimental signature, there are background processes which can fake a Wγ event. By far, the largest background comes from W+j production in which the jet is misidentified as a photon. Jets can be misidentified as photons if the jet has fragmented into a leading π^0 which gives an electromagnetic cluster consistent with a photon, if the initial π was of sufficient E_T. Also, Z$\gamma \rightarrow \mu\mu\gamma$ production events in which one muon is lost also mimic Wγ. Wγ events in which the muon itself does not originate from the decay of the W boson, but from a tau lepton also constitute a background. Besides these, there are instrumental backgrounds such as when a muon, an electron and large missing E_T are present and the track for the electron is not reconstructed.

Only events that were triggered on a single high p_T muon are considered for this analysis. This yields several important advantages. The first is that the trigger can be used for both the signal and the background so that a natural normalization from the data may be obtained. The other is that the photon E_T threshold is not set at the trigger level, so that analysis may be conducted offline as low in E_T as possible so that the largest number of events may be used. This will be especially important in the search for the radiation amplitude zero, where statistics will be vital in showing the dip in the rapidity spectrum.

In order to maximize the sensitivity to events in which the photon is emitted either from the initial quarks or the triple gauge vertex, a kinematic constraint on

the transverse mass of the muon-photon-neutrino system is made. If the longitudinal momentum of the neutrino was known, then an invariant mass cut on the mass of the three final state particles could be made to ensure that the mass of the system was greater than that of the W boson (meaning that the photon did not originate from the lepton itself). Since the longitudinal momentum of the neutrino is not known, a three body transverse mass may be constructed to suit a similar purpose:

$$M_T^2(l\gamma; \not{E}_T) = \left((M_{l\gamma}^2 + |\mathbf{p_T}(\gamma) + \mathbf{p_T}(\mathbf{l})|^{\mathbf{2}})^{\frac{\mathbf{1}}{\mathbf{2}}} + \not{E}_T\right)^2 - |\mathbf{p_T}(\gamma) + \mathbf{p_T}(\mathbf{l}) + \not{E}_T|^{\mathbf{2}}. \quad (2.12)$$

In Equation 2.12, $\mathbf{p_T}(\gamma)$ and $\mathbf{p_T}(\mathbf{l})$ are the vector transverse momenta of the photon and lepton respectively, $M_{l\gamma}$ is the invariant mass of the lepton-photon system, and $\not{E}_T$ is the missing transverse energy.

The three body transverse mass (as shown in Equation 2.12) is the equivalent of the invariant mass of a three body system in which the longitudinal momentum of one of the particles is unknown. For events in which the photon is radiated from the lepton, the three body transverse mass should be at, or lower than the mass of the initial W (modulo finite width and resolution effects). For events in which the photon was radiated off the initial state quarks, or from the W itself, the three body transverse mass should be reconstructed as higher than the W mass.

2.3 Limits on Anomalous Couplings

Anomalous coupling between the W boson and the photon can be searched for in a number of ways. The lowest level manner in which this can be measured is in the measurement of the cross section for Wγ production. However, additional information is contained in the kinematics of the final state particles, such as the photon transverse energy distribution.

Using the parametrized Lagrangian in Equation 2.1, sets of Monte Carlo events may be generated with different anomalous coupling parameters. Given a simulation of the detector response, these may be compared to the data. For each set of coupling parameters, the likelihood that the data represents the behavior in the Monte Carlo may be calculated.

Utilizing a Bayesian method to determine the likelihood is fairly straightforward. One would expect in a given experiment:

$$\mu = b + \epsilon L \sigma(\Delta\kappa, \lambda). \tag{2.13}$$

Thus, if we expect the number of events in an experiment to be Poisson distributed:

$$P = \frac{e^{-\mu}\mu^n}{n!} \tag{2.14}$$

then,

$$P = \frac{e^{-(b+\epsilon L\sigma(\Delta\kappa,\lambda))}(b + \epsilon L\sigma(\Delta\kappa, \lambda))^n}{n!}. \tag{2.15}$$

Here, $\sigma(\Delta\kappa, \lambda)$ is the cross section for the process as a function of the coupling parameters. In this equation for the Poisson distributed probability, there are parameters that are known as nuisance parameters. A nuisance parameter is commonly defined as any parameter whose true value is unknown but which must be excised from the problem in order for an inference to be made on the parameter of interest. b (the number of background events), L (the integrated luminosity) and ϵ (the efficiency times acceptance) are examples of these parameters. The assumption is made that these nuisance parameters are Gaussian distributed, with their properties given by the measured values (properties being σ and $\overline{x}$, etc). Thus one may numerically integrate over the nuisance parameters in order to obtain the true probability P as a function of the anomalous coupling parameters:

$$P = \int G_L dL \int G_b db \int G_\epsilon d\epsilon \frac{e^{-(b+\epsilon L\sigma(\Delta\kappa,\lambda))}(b + \epsilon L\sigma(\Delta\kappa, \lambda))^n}{n!}. \tag{2.16}$$

G_x is a Gaussian distribution for nuisance parameter x, which has a nominal mean of μ=1, and an RMS distribution of σ_x:

$$G_x = \frac{1}{\sigma_x\sqrt{2\pi}} e^{\frac{-(x-\mu)^2}{2\sigma_x^2}}. \tag{2.17}$$

For later reference, the likelihood (L=log P) will be used for convenience.

From the Lagrangian (Equation 2.1), one would expect that the cross section for

Wγ production as a function of $\Delta\kappa$ and λ would be of the form:

$$\sigma(\Delta\kappa, \lambda) = \sigma_{SM} + a_0\Delta\kappa + a_1\Delta\kappa^2 + b_0\lambda + b_1\lambda^2 + c_0\Delta\kappa\lambda. \quad (2.18)$$

This would give rise to a cross section that increases with the anomalous couplings. Therefore one may attempt to use this bilinear form to fit the likelihood distribution (even though the functional form of the likelihood itself may not be this function). From the final fit of the likelihood, limits on the coupling parameters may be obtained.

In order to use the information in the entire $E_{T\gamma}$ spectrum, the probability may be obtained in bins, and then multiplied together. In some cases, such as ours, the final bin is constructed such that there are no signal candidates so that more strict limits may be set.

As previously mentioned, limits on anomalous couplings have been set in the past, both at LEP and in Run I at the Tevatron. These limits, at 95% confidence level are summarized in Table 2.1*.

Experiment	$\Delta\kappa$	λ
DELPHI	[-0.13, 0.68]	[-0.11, 0.23]
ALEPH	[-0.200, 0.258]	[-0.062, 0.147]
L3	[-0.08, 0.38]	[-0.14, 0.14]
OPAL	[-0.27, 0.07]	[[-0.13, 0.01]
CDF	[-2.3, 2.3]	[-0.7, 0.7]
DØ	[-0.93, 0.94]	[-0.31, 0.29]

Table 2.1 Summary of Previous Limits on Anomalous Couplings at 95% CL.

*These values are obtained from [6], [7], [8], [9], [10], and [2].

Chapter 3
Experimental Apparatus

3.1 Tevatron

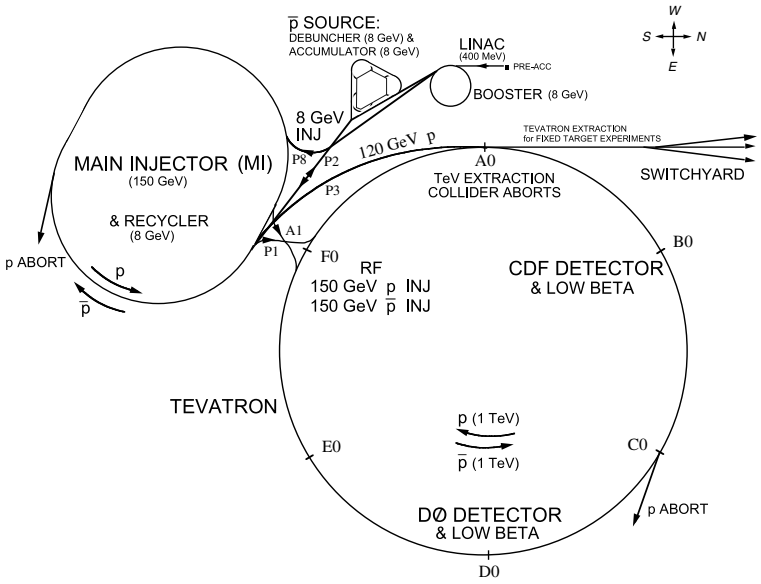

Figure 3.1 Diagram of Tevatron Complex.

The Fermilab Tevatron complex is currently the highest energy collider facility in the world, capable of accelerating protons and anti-protons to 980 GeV, for a collision energy of $\sqrt{s} = 1.96$ TeV at the two experiments. As with most high energy colliders, the Tevatron is the final step in a long chain of accelerators.

Negatively charged hydrogen ions begin at the Cockcroft-Walton (CW) generator. The CW functions to accelerate the ions to 750 keV. The ions are then bunched (spatially) and led into a 150m long linear accelerator (LINAC). The LINAC accel-

erates the ions to 400 MeV, after which the particles are sent through thin sheets of carbon foil, which strip off the electrons leaving only the positively charged protons. The protons are then directed into the booster where they are accelerated to 8 GeV, the injection energy for the Main Injector (MI). The MI serves to accelerate protons for injection into the Tevatron (injection energy 150 GeV), and also to provide high energy protons to the anti-proton source where the beam of protons is directed onto a fixed target producing (among many other secondaries) anti-protons. The anti-protons are then sent to the Accumulator where they are bunched and inserted into the Main Injector. After the Main Injector accelerates the protons and anti-protons to 150 GeV, both are transferred to the Tevatron for their final acceleration to 980 GeV. The beams are then brought together at the collision regions at D0, and B0 (the home of the CDF experiment). At all other interaction points, the beams are kept separate so that collisions only take place at the two points at which there are experiments.

A measure of the number of collisions that are taking place is known as the instantaneous luminosity. Instantaneous luminosity is given in units of $\mathrm{cm}^{-2}\mathrm{s}^{-1}$ (or per cross section (in cm^{-2}) per second). The instantaneous luminosity is defined as the number of inelastic $p\overline{p}$ collisions that occur per second at an experiment. Each experiment at the Tevatron has a dedicated detector for measuring the number of these events. A typical instantaneous luminosity for the data collected for this

thesis is $3.5 \times 10^{31}\text{cm}^{-2}\text{s}^{-1}$. The integrated luminosity is a measure of how many collisions have taken place over the course of the entire period of beam delivery to each experiment. Effectively, using the measured integrated luminosity corresponds to normalizing the data in question to the inelastic QCD $p\overline{p}$ cross section.

A single 'store' of protons and anti-protons in the Tevatron can last days, while the number of collisions in each crossing decreases. A typical store will collide for about a day. When the instantaneous luminosity is too low, the particles are removed from the Tevatron, and the process of injecting a new set of protons and anti-protons begins. Since the Tevatron is the last step in a long chain of accelerators, the process of building up the necessary numbers of protons and anti-protons is done while the previous set is colliding, thus limiting the amount of time where the experiments are waiting for collisions to occur.

3.2 The DØ Detector

An overview of the upgraded DØ detector is presented here. Interested readers are referred to [11] for a detailed description of the Run I detector, and [12], [13], for the enhancements added for Run II. The major components are described with an emphasis on the instrumentation that will be used in the measurement of quantities required for the Wγ analysis.

Note that two different coordinate systems are used in the description of the detector. The first is a conventional cylindrical-polar description in which the z-axis

is identified with the beam line through the center of the detector (protons circulate in the positive z direction). The radial direction and the azimuthal (ϕ-)angle are then used for identifying the position in the detector as a whole. There is another system used however, which is a modified spherical-polar description, coordinates in η and ϕ are quoted where ϕ is simply the azimuthal coordinate and η is called the pseudorapidity and is defined as:

$$\eta = -ln(tan(\frac{\theta}{2})), \tag{3.1}$$

where θ is the polar angle made with respect to the beam axis. In the high energy limit (p$\gg$m, which is often the case at Tevatron energies), η is a good approximation of the true rapidity (y) which is given by Equation 2.8. The advantage of using the rapidity (or in our case the pseudorapidity) is that distribution of particles is approximately flat in η (to approximately $|\eta| < 2.5$ [14]).

Sometimes for detector quantities it is convenient to define coordinates with respect to $\eta_{detector}$, which is simply the pseudorapidity defined with respect to the center of the detector, instead of the position of the interaction. For a particle from an interaction that is not in the center of the detector, $\eta_{detector}$ of one component need not be the same as $\eta_{detector}$ of another.

Another important quantity is ΔR which is defined as:

$$\Delta R = \sqrt{(\phi_1 - \phi_2)^2 + (\eta_1 - \eta_2)^2}. \tag{3.2}$$

ΔR is generally used to describe the separation between two physics objects with coordinates (η_1,ϕ_1) and (η_2,ϕ_2) in the detector. One can also define a cone in ΔR of a constant value, which is commonly done to isolate objects in the detector.

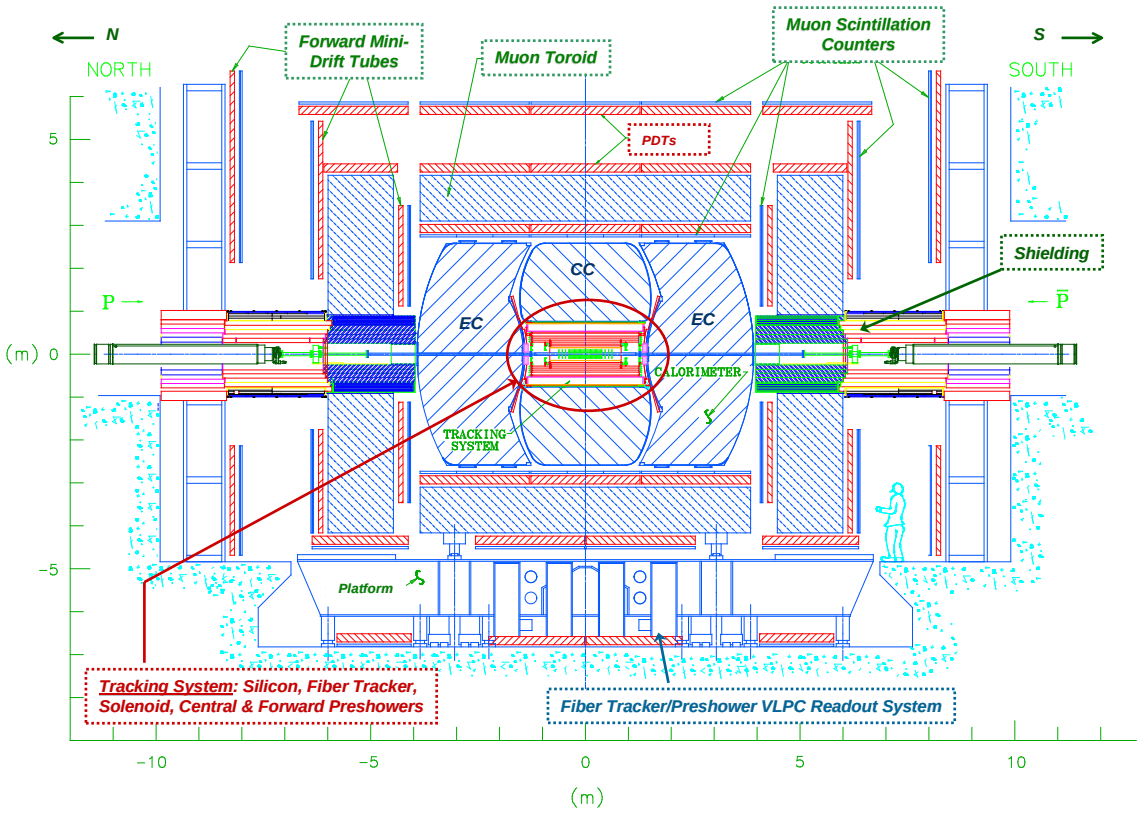

Figure 3.2 DØ Detector Overview.

3.2.1 Tracking

In Run I, the tracking system of the DØ detector consisted of a central transition radiation detector and drift chambers in the central and forward. There was no magnetic field in the interaction region to provide charge determination or a momentum

measurement. For Run II the transition radiation detector and drift chambers were removed. These detectors were replaced by a silicon microstrip tracker, a central fiber tracker, a superconducting solenoid, and preshower detectors directly before the calorimeters. The silicon microstrip tracker provides good spatial resolution in the area very close to the beam line. The central fiber tracker provides a fast trigger for tracks in the detector as well as (in conjunction with the SMT) a measurement of momentum (curvature) of the tracks in the magnetic field. The preshower detectors (which are described in 3.2.2) are meant to compensate for the energy loss in the solenoid, as well as provide additional separation for electrons and photons from QCD jets. The central tracking volume is shown in Figure 3.3.

Silicon Microstrip Tracker

The silicon microstrip tracker (SMT) is the closest subsystem to the beam pipe. It is made up of two different structures, barrels and disks. Both structures have thin silicon strips with fine cathode lines etched onto their surfaces.

These silicon microstrips are solid state detector devices which give a signal when charged particles pass through them. The charged particles deposit a small amount of energy in the material through ionization. Electron-hole pairs are produced from this ionization energy, and are collected at the nearest cathode. This produces a signal which will in turn determine the position at which the particle passed through the silicon. Reconstruction of the path of the particle leaving the interaction region

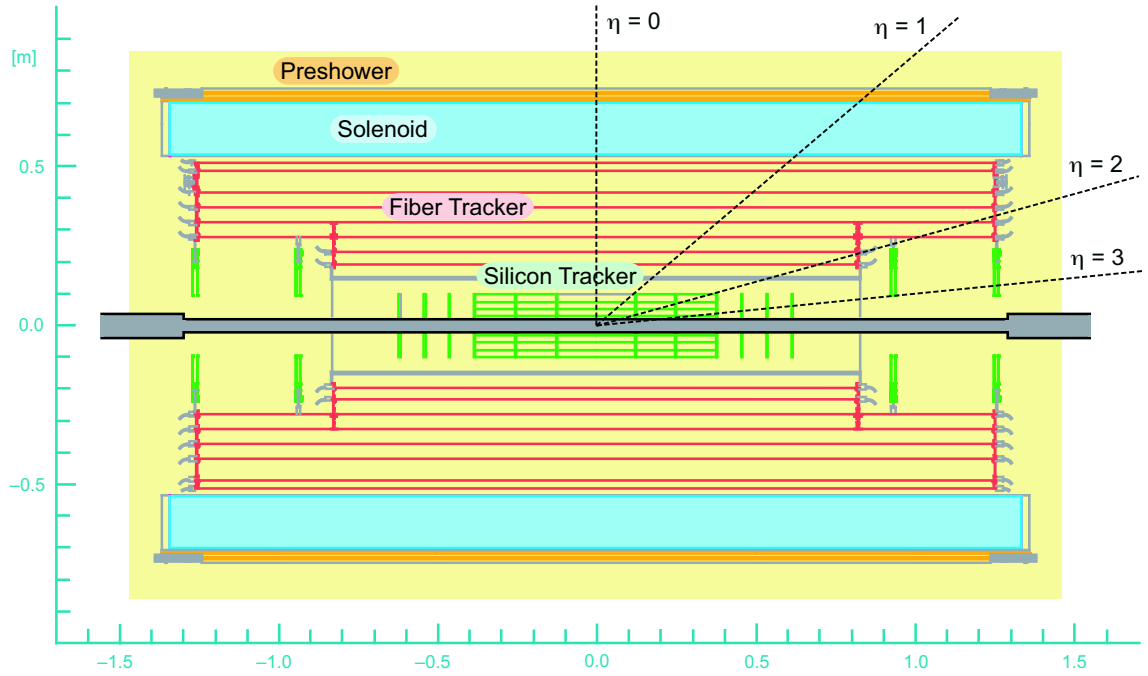

Figure 3.3 DØ Tracking Overview.

is made based on these signals. Since there are many cathode lines, with very small spacing, this gives a very accurate measurement of the position at which the particle crossed the material.

The position and design of the silicon detector allows for reconstruction of tracks within a detector $|\eta| < 3$. The barrels of the SMT are located in the center of the DØ interaction region so that the event vertex is likely to be within its acceptance. Secondary vertices, due to long lived particles, may also be reconstructed within the central assembly of the silicon. The disks of the SMT are placed at increasing spacing along the beam line so that the maximum coverage may be obtained.

Figure 3.4 shows the general arrangement of the SMT barrels and disks. In the most central regions small diameter barrels, and slightly larger diameter "F" disks cover the largest part of the interaction region. The four barrels closest to the center of the detector have four layers of double sided silicon microstrips in the axial direction and at ninety degrees to the axial direction (this direction indicates the direction of the cathodes). The contrasting pitch of the cathode directions allow for three dimensional hit positions to be reconstructed.

The outermost two barrels have single sided silicon strips with strips in the axial direction and two degrees to the axial. The "F" disks, made up of double sided silicon strips at thirty degrees stereo pitch, are interspersed with the outermost barrels. Beyond, these are the "H" disks. The "H" disks are large diameter and are made up of single sided silicon strips at fifteen degrees stereo pitch. These are the outermost detectors in the silicon system, and allow for detection of tracks at small angles to the beam direction. In the larger scheme of tracking for high p_T objects the SMT adds good spatial resolution hits for tracks for better momentum measurement.

The amount of charge collected is digitized via the SVX-II chip, which is included with the module, and read out. The full 8-bit digitization is made available through the hits in the reconstruction offline. Since the full SMT detector contains approximately 800,000 channels of readout, the SVX also handles setting an online threshold for each chip.

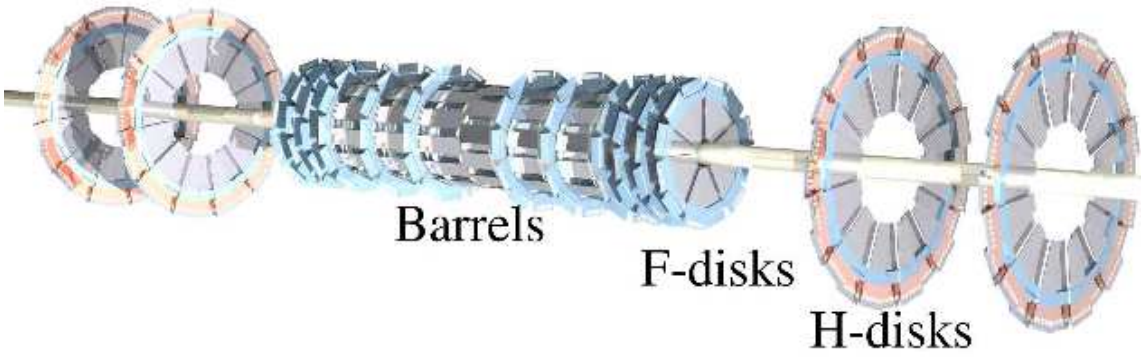

Figure 3.4 Diagram of Silicon Detector.

Signals above threshold for each channel are transferred via cables from the inner portion of the detector to a device known as a sequencer, located on the platform beneath the detector. The sequencer reads the electrical signals and outputs a digital light pulse signal which is then carried via fiber optic cables to the readout crates in the movable counting house.

Central Fiber Tracker

The Central Fiber Tracker (CFT) surrounds the silicon detector. The CFT consists of ribbons of scintillating fiber mounted on concentric cylinders for mechanical support. There are eight cylinders (of increasing radius), each of which contains a doublet layer of axial fibers (parallel to the beam direction), and a doublet layer at three degrees stereo pitch to the axial direction. The CFT is positioned to complete the coverage of the central tracking volume. The CFT also provides track information for fast triggering.

Charged particles passing through a layer of the fibers deposit a small amount of energy via ionization. The organic molecules of the scintillating fiber are excited via this energy, and then radiatively decay to their ground states producing photons inside the fibers. The fibers then act as waveguides for the produced photons, and carry the light to the end of the cables. At one end of the tracker, the fibers are mated to clear fiber optic waveguides, which in turn lead to photodetectors. At the opposite end, the fibers are mirrored, so that the light may be reflected back to the detection end.

The central fiber tracker provides full sixteen layer coverage of detector $|\eta| < 1.6$. Tracks at larger detector η may still pass through some of the layers as well, up to $|\eta| < 1.8$.

VLPC Cassettes The light from the scintillating fibers is collected at a specially prepared photon detection "cassette". Each of these cassettes contain the waveguides to transmit the light from 1024 channels of the tracker to arrays of visible light photon counters (VLPCs). Visible light photon counters (VLPCs) convert the photons to electrical signals much like a photomultiplier tube (with gains on order 20,000-50,000 and high quantum efficiency). However, the optimum operating temperature of these devices is approximately 9 K (depending on the different properties of each VLPC hybrid, see [15]).

The VLPC hybrids were characterized to determine their gain and temperature parameters before cassettes were assembled. The VLPCs were grouped by operating temperature* and gain. The chips with the highest gain were used for the CFT axial layers, since those channels would be used in the trigger. Among those highest gain chips, the best were selected to be used with the longest waveguides (to compensate somewhat for the greater attenuation in the fiber).

The cassettes were constructed to take the optical signal from the waveguides at room temperature, and transfer it onto the designated VLPC chips, which are held at the bottom of the cassettes within a cryostat held at 6 K (using liquid helium). Individual chips are kept at different temperatures by resistive heaters mounted near the VLPC chips at the bottom of the cassette. The electrical signal from the VLPC is transferred via a flexible cable (essentially gold traces deposited on Kapton), which then returns the signal to the readout electronics mounted on the upper portion of the cassette bodies at room temperature. The design of the cassettes is quite complex, due to the necessity of keeping the portion of the device with the VLPCs at low temperature, while carrying the signals from the chips to the readout electronics at room temperature (see Figure 3.5 for a general arrangement). The interested reader is referred to [16] for further details.

*The resistive heaters on the cassettes at the cold end were attached at the end of a 16 (128 channel) chip module. Thus the performance could be optimized by selecting chips that all had similar operating temperatures, and setting the heater accordingly.

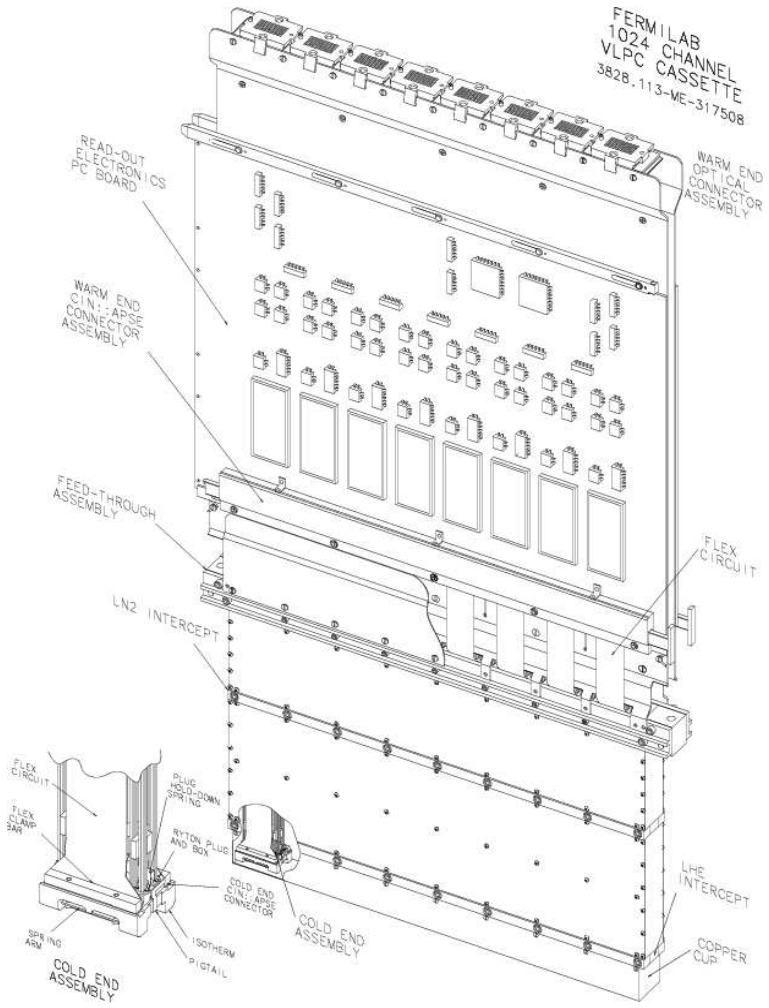

Figure 3.5 Diagram of VLPC Cassette.

The electronics for the digitization of the charge from the VLPC cassettes are mounted on the sides of the cassette body. The signals from the cassettes are sent first to the SIFT discriminator chips, which provide hits to the different trigger systems. The hits in the axial layers of the CFT are then sent to the Level 1 trigger via a separate low voltage differential signal path. The analog signal is then digitized by

SVX-II chips (the same as used for the SMT readout), and transferred from the AFE backplane to sequencers which serve the same purpose for the CFT as the SMT. The discriminator output is packed and sent out with the readout of the SVX chips.

Central Track Trigger The signals from the discriminators are sent to the Central Track Trigger (CTT) system. Each of the front end electronics boards mounted on the cassettes has encoded in its firmware a 'personality' which allows the trigger electronics to map the signals into the different trigger sectors. Once the mapping is done, the axial layers are organized into four degree trigger sectors (in ϕ). The pattern of hits in each trigger sector is compared to track equations that are pre-loaded into the trigger firmware. Hits are required in all of the eight axial layers to construct a track. This limits the efficiency of the trigger, but also reduces the rate of fake track triggers, and limits the number of track equations required.

By comparing the hits in the axial layer to the predefined track equations, the Level 1 Track trigger reports the number of tracks in each of its four p_T bins to the trigger manager. This information is also forwarded to the Level 1 Muon trigger so that tracks in ϕ may be associated with octants of the muon system for triggering.

Solenoid

A 2 Tesla solenoid surrounds the inner tracking systems. The inclusion of a magnetic field increases the number of processes that may be explored by providing

charge discrimination. The solenoid is located just interior to the central preshower detector and calorimeter.

The solenoid magnet keeps a constant field (to approximately 0.5%) of 2 Tesla in the region of the tracking subsystems, parallel to the beam line. It is a superconducting solenoid, which requires a supply of liquid helium to keep the temperature low enough for the coil to conduct without resistance. Since there is no return path for the field lines, the field is kept constant in the end regions by using different grades of conductor, allowing for a greater charge density at the ends of the solenoid than in the center. The liquid helium supply that is provided to the magnet also supplies the cryostats for the fiber tracker/preshower detector cassettes (described in 3.2.1). The energy stored in the energized solenoid is approximately 5 MJ. The bulk of the coil and cryostat that make up the solenoid assembly is approximately 0.87 radiation lengths thick.

3.2.2 Energy Measurement

The sampling calorimeter from Run I is unchanged, except for the complete replacement of the readout electronics which allows the calorimeter to operate in the new higher luminosity and faster crossing time of Run II*. Central and forward preshower detectors have been added to provide additional energy sampling and shower profiles prior to the calorimeter.

*The Run I crossing time for the Tevatron was 3.5 μsec. The crossing time for Run II is 396 nsec.

Preshower Detectors

The preshower detectors are the last instrumentation prior to the calorimeters. The addition of the preshowers is important for the following reasons:

- The position measurement in the preshowers allows for good matching of tracks from the inner tracking detectors to objects in the calorimeter.
- The energy deposited in the preshowers essentially creates an additional layer of calorimeter with fine segmentation.
- The shape of clusters in the preshower detectors helps to discern whether a cluster in the calorimeter is from a single object (an electron for instance) as opposed to being from two clusters close together (a π^0 for example).

The preshower detectors are made up of triangular strips of scintillating material that are wrapped about wavelength shifting fiber optic cable. These detectors function much like the CFT. Ionization energy from charged particles is emitted from the scintillating material as photons. Photons from the scintillating material enter the fiber optic cable, where by absorption and re-emission at smaller wavelengths, the photons are shifted into the optimum range to be read out by VLPCs in cassettes like those described in Section 3.2.1. There is expected to be a considerably larger light yield than in the CFT system (due to the larger path length through the scintillator, and the number of particles in the shower), and thus the VLPCs do not require as high

a gain. The amount of light collected from the preshower detectors is proportional to the amount of energy deposited by the shower, which is in turn proportional to the energy of the shower. By using the light yield and gain from the preshower detectors, the deposited energy may be measured.

A layer of lead has been added to the material outside the solenoid, which increases the probability that an electron or photon will begin to shower before the preshower detectors. An electron or photon will pass through approximately two radiation lengths, at the shortest path length, before reaching the central preshower detector.

The division of the calorimeter sections necessitates the division of the preshower detector into forward and central detectors. The central preshower (CPS) uses the solenoid and lead layer as its radiating material. The CPS consists of three layers of scintillating strips, one layer along the axial direction, and two angled at approximately 22 degree stereo pitch.

The forward preshower detectors (FPS) are different in geometry. Each FPS consists of four layers of scintillating material, two before a layer of lead, and two after. These layers are aligned at different pitches so that the three dimensional position of the particle may be found both before and after showering. The innermost layers of the FPS are known as the MIP* layers, since there is little material between these layers and the interaction region. The outer layers are known as the shower

*Minimum Ionizing Particle.

layers, since electromagnetic showers that develop in the lead absorber would first be detected here. Since the FPS covers a range of detector η outside the full CFT coverage, it can serve as both a part of the tracker and as part of the calorimeter.

In addition to the two preshower systems there is a layer of scintillating pixels in the remaining space between the central cryostat and the endcap cryostats so that there would be no inactive medium for the particles to pass through. This gives additional position and energy measurement for particles that 'fall in the cracks'. Thus even for electromagnetic or hadronic showers in the boundary between the central and endcap calorimeters, some measurement may be obtained. This helps in the proper measurement of the missing transverse energy, which is the important use for the analysis described here. These systems are known as the Intercryostat Detector (ICD) and Massless Gaps (MG) respectively.

Calorimeter

The DØ calorimeter is a liquid argon-uranium sampling compensating calorimeter. Its function is to provide energy measurement for particles exiting the tracking volume, as well as to provide the shapes of the energy deposition for particle identification.

Particles passing through the calorimeter (with the exception of muons and neutrinos) will interact with the material and shower, producing more charged particles. The charged particles leaving the material (the absorber) then ionize the liquid argon

(the active medium). Charge from the ionized liquid argon is then collected at high voltage pads in each cell, giving a measure of how much energy was deposited in the material. It is important to note that there are gaps between modules in the different sections of segmentation in the calorimeter (some of this space is taken up by the material in the boundary). Showers reconstructed near the edges of the modules will be more poorly measured due to the amount of charge which is not collected at the readout pad. Therefore, if an electromagnetic cluster's centroid is determined to be within these gaps it is discarded. This is treated as a loss in acceptance for the Wγ analysis.

The principle of a compensating calorimeter (such as the DØ Calorimeter) is to equalize the response of the calorimeter signals from hadrons and electrons. This is achieved by the tuning the thickness and the material chosen for the absorber. The depleted uranium absorber provides backgrounds at low energies due to its own radioactive breakdown, but low energy neutrons from nuclear breakup (due to the hadronic showers) cause fission in the uranium producing charged particles which compensate for the lower visible energy in hadronic showers. The ionization energy from these fission effects can be measured in the same way as the ionization energy from leptons.

The calorimeter is composed the central calorimeter, which covers the range $|\eta| < 1.1$ and the two endcap calorimeters which cover from $|\eta| > 1.3$ to $|\eta| \approx 4$ (see

Figure 3.6). Liquid argon is the active medium, particles passing through the absorber material (the uranium, and in some areas copper and steel) will shower.

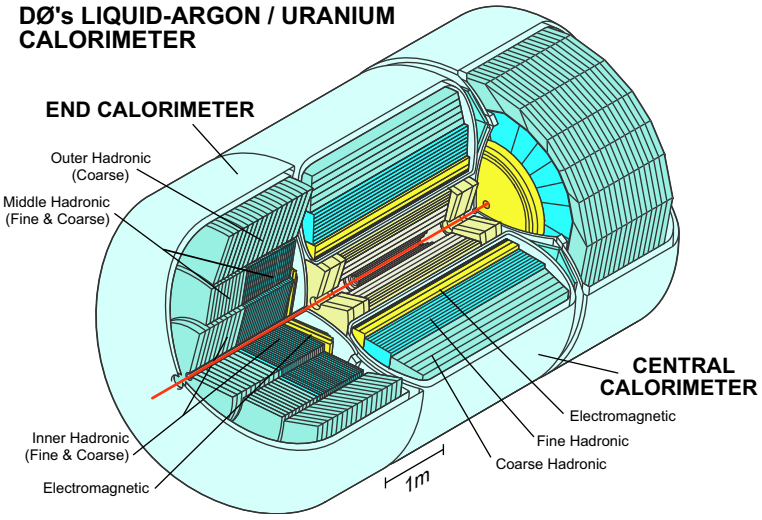

Figure 3.6 Cross section of the DØ Calorimeter.

The calorimeter is divided into three different sections of segmentation. There are the four the innermost layers, which make up the electromagnetic calorimeter. These layers are finely segmented, and the absorber is almost pure uranium. Next, there are three layers of larger segmentation and thicker uranium-niobium alloy plates which make up the fine hadronic portion of the calorimeter. Beyond the fine hadronic section there is a single layer of coarsely segmented absorber made up of thick copper (and stainless steel in the case of the endcaps) plates which serve as the coarse hadronic layer. The parameters of the calorimeter are summarized in Tables 3.1 and 3.2.

The electromagnetic calorimeter layers are designed so that showers from electrons

Module Type	EM	Fine Had.	Coarse Had.
Central			
$\eta_{detector}$	$\pm$1.1	$\pm$1.0	$\pm$0.7
Absorber Material	Uranium	Uranium (1.7% Nb)	Copper
Readout Layers	4	3	1
Segmentation ($\Delta\eta \times \Delta\phi$)	0.1×0.1 (Layer 1, 2, 4) 0.05×0.05 (Layer 3)	0.1×0.1	0.1×0.1
Radiation Lengths	2, 2, 7, 10 X_0 (0.76 λ_a)	1.3, 1.0, 0.9 λ_a	3.2 λ_a
Total X_0	21	96	33
Total λ_a	0.76	3.2	3.2

Table 3.1 DØ Central Calorimeter Parameters. X_0 is the radiation length for electromagnetic particles, while λ_a is the nuclear interaction length for hadronic particles.

Module Type	EM	Fine Had.	Coarse Had.
Endcap			
$\eta_{detector}$	$\pm$(1.3-4.1)	$\pm$(1.6-4.5)	$\pm$(2.0-4.5)
Absorber Material	Uranium	Uranium (1.7% Niobium)	Steel
Readout Layers	4	4	1
Total Depth	20 X_0 (0.95 λ_a)	4.4 λ_a	4.1 λ_a

Table 3.2 DØ Endcap Calorimeter Parameters.

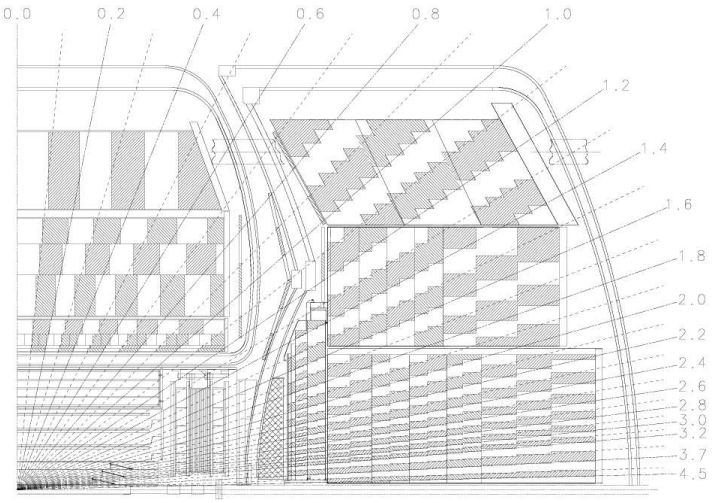

Figure 3.7 Side View of the DØ Calorimeter.

and photons stop within the finely segmented layers of uranium. The maximum of electromagnetic showers is calculated to take place in the third electromagnetic layer, so this region is further segmented for a more precise measurement. This calculation was made for the Run I calorimeter, which did not have the additional material of the solenoid and preshower absorber. Even so, the shower maximum is still calculated to be within the third electromagnetic layer. The η and ϕ parameters for an electromagnetic cluster (before track or preshower association) are calculated using the z vertex position from the tracking and the position at the third floor of the electromagnetic calorimeter.

The calorimeter is organized into towers for readout. Each 'tower' in the calorimeter is approximately 0.1×0.1 in $\eta \times \phi$. For the trigger system, these towers are summed

into 0.2×0.2 in $\eta \times \phi$ and can be used to measure the shower or jet profile while online. Various energy thresholds on the 0.2×0.2 towers can be set for use in the trigger.

The main change from the calorimeter from Run I is a full replacement of the readout and trigger electronics which allows for faster readout, required due to the higher crossing frequency of Run II. This complicates the readout of the calorimeter, due to the fact that charge is still being collected from the previous events as additional events occur. This change in the amount of time available to collect the charge from ionized liquid argon is handled by what is known as baseline subtraction. The calorimeter dynamically assigns a value to the amount of energy at the start of a collision, then takes another point after the collision, the difference being the amount of charge from the interaction that took place.

3.2.3 Muon System

A separate detector system is exclusively devoted to the detection of muons. Since muons will not shower in the calorimeter, and all other particles should be contained within the calorimeter, the muon system is positioned furthest from the interaction region. The system is composed of scintillators (for time measurement) and proportional drift tubes for finer position measurement. A magnetic iron toroid adds additional interaction lengths from the material, and makes an additional measurement of the momentum of muons available.

Muons pass through the calorimeter, and deposit a small amount of their energy via ionization. Then, upon reaching the A-layer of the muon system, the muon interacts with the scintillator paddles first, giving a hit that records the time (relative to the beam crossing time) at which the hit occurred. The muon continues and leaves hits in the A-layer proportional drift tubes (or mini-drift tubes in the forward). This track allows the extrapolation of the original direction of the muon prior to the toroid. Past the A-layer, the muon enters the iron of the toroidal magnet, which is run at a magnetic field strength of 1.8 T. The muon is multiple scattered through the iron, as well as bent by the magnetic field, and emerges at the B-layer, where again a measurement of the position may be made. By use of the positions before and after the toroid, a track may be fit to the muon and the amount of bend due to the magnetic field of the toroid estimated. If a muon does not have the necessary momentum to penetrate the toroid, then only the measurement of momentum from the central tracker is available.

The muon system is divided into two sections, the central (or wide angle) section ($|\eta| < 1$) and the forward section ($1 < |\eta| < 2$). Each of these systems is divided into three layers, A, B, and C. The A-layer is the closest to the cryostat of the calorimeter. An iron toroid magnet is between the A-layer and B-layer, and then the outermost C-layer completes the system. The central muon system consists of three layers of proportional drift tubes, with scintillators to provide the necessary time stamp for the

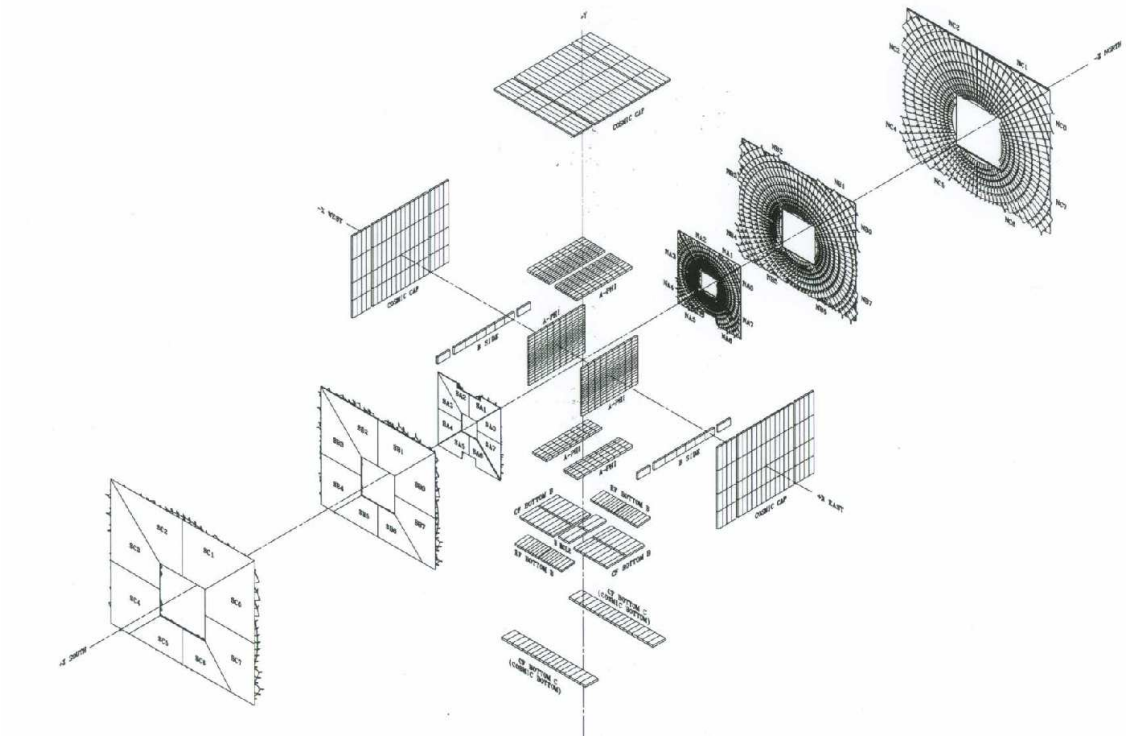

Figure 3.8 Exploded View of DØ Muon Scintillators.

chambers. This allows for momentum measurement and tracking independent of the central systems. The forward muon system is composed of mini-drift tubes instead of proportional drift tubes due to the higher radiation environment in the forward direction. Additional shielding was also added around the beam line, to cut down on beam related backgrounds in the forward system. Also, the forward muon system consists of three full layers of mini-drift tubes and scintillator, as opposed the central where there are two layers of scintillator and three layers of wires.

From Run I, it was discovered that the proportional drift chambers had to be

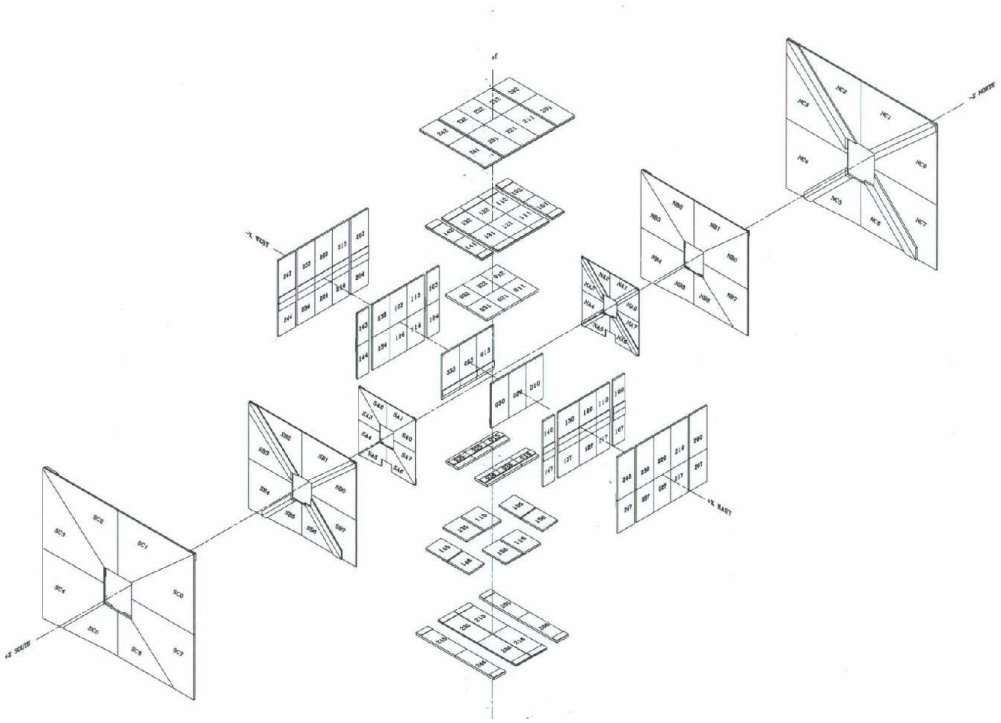

Figure 3.9 Exploded View of the DØ Muon Wire Chambers.

'cleaned' by the application of a high voltage to return to the cathodes to their proper operating conditions. Due to the high occupancy in the forward direction it was necessary to 'clean' these chambers with an unacceptable frequency (allowing too much dead time) and thus these chambers were replaced with mini-drift tubes. The only difference between these tubes and the larger proportional drift chambers is the lower occupancy due to the much smaller cross-sectional area of the small tubes, as well as an improvement in the response time. For both of the muon systems the resolution is on order 1mm due to multiple scattering.

Muon Trigger Coverage

It is important to note that the muon trigger used in the Wγ analysis always required at least coincidence of scintillators (before and after the toroid) to accept an event. Figure 3.8 shows the exploded view of the scintillator coverage. In the bottom of the detector, one can see that there is less scintillator coverage than in all of the other regions. Triggers requiring a scintillator coincidence therefore will not fire when a muon in this area passes through the muon system. This area is known as the 'hole', and is necessitated by the physical support for the calorimeter. In the analysis, an area of $\eta_{detector} - \phi$ is defined so that this may be removed from the acceptance. This area is defined as being within $|\eta_{detector}| < 1.0$ and in $4.25 < \phi < 5.15$. Muons could still be reconstructed offline within this region, but could not fire the trigger.

3.2.4 Trigger and Data Acquisition

Beam crossings from the Tevatron occur approximately every 396ns. Not all of these crossings are occupied, but even so, it is impossible for the detector to read out every single beam crossing during a store. Thus the experiment readout is triggered only if the event possesses qualities that are signatures of interesting physics produced in the collision.

The DØ detector has three levels of triggering logic for the implementation of physics triggers. The first layer (Level 1) is made up of hardware quantities from

individual detectors, implemented in firmware. Level 1 must reduce the rate from the beam crossing clock (1.8 MHz), to approximately 1 kHz. If a trigger is determined to have a Level 1 rate which takes up too much of the bandwidth, it may be prescaled. A prescale reduces the rate at which a trigger at Level 1 may fire by only allowing triggers in some pre-determined number of crossing. For example, a prescale of three will randomly select (on average) one out of three triggers from the Tevatron bunch crossings. This is done randomly to avoid selecting a single bunch crossing preferentially. The data is then buffered pending an accept signal from the second level of triggering which has the time to make rough measurements on event quantities and objects with information that spans different detectors. If an event passes Level 2, it is sent on to the third layer of triggering. The event will undergo a fast reconstruction (like the algorithms described in Chapter 4, only optimized for speed), and then the final decision will be made about whether or not to write out the event.

During the first two stages of the trigger, rough quantities that could be calculated quickly in the different hardware systems are used to reduce the rate into Level 3. However, since Level 3 does a fast reconstruction using all of the different detector readouts, the information from each readout VME crate must be assembled before the data may be processed. Complicating this further is that Level 3 is made up of a farm of approximately 100 individual Linux nodes. Therefore the data acquisition system must coordinate the information from each crate for each event and ensure

that the proper farm node receives data from all of the crates before reconstruction (and possibly the final writing of the event) may be done.

A scalable system based on single board computers (SBCs) and a Cisco 6509 switch was implemented for this purpose [17]. A single process known as the routing master (RM), which runs on its own single board computer, interfaces with the hardware Trigger Framework which coordinates all of the trigger bits and runs in the system. The RM controls coordinating the information from the crates, and the routing of the information from each crate to available farm nodes. Each readout crate in the system contains an SBC, which has dual 100 Mb/s ethernet interfaces, as well as a VME-to-PCI interface. The crate will signal that it is ready for readout via the VME backplane, and the SBC collects the data from the readout buffers (a single crate's data is sometimes referred to as an event fragment). The information from a given event is then sent through the switch to a farm node assigned by the routing master. The farm node receives a list of crates from the routing master, and checks to make certain all crates arrive before beginning the reconstruction.

Level 1 At Level 1, there are only a few quantities available within the DØ detector. These can roughly be separated out into the following list:

- Calorimeter quantities: Energy deposited in projective trigger towers in the calorimeter is available at Level 1. This energy is divided into two basic types,

Electromagnetic (the amount of energy in just the electromagnetic portion of the trigger tower) and Total (the full amount of energy in the tower). Level 1 triggers can require one or more towers above four pre-programmed thresholds (called reference sets). An example of a typical Level 1 calorimeter trigger is CEM(2,10), which requires two towers in the calorimeter to have at least 10 GeV of energy (in Level 1 units) in the electromagnetic portion of the trigger towers. The Level 1 calorimeter readout is separate from the full cell-by-cell (precision) readout that is available at Level 3. Level 1 trigger towers are sums of the projective towers in segmentation of 0.2×0.2 in $\eta \times \phi$.

- Muon System quantities: At Level 1, the muon system has trigger terms consisting of scintillator and wire hits in each region and octant. The scintillator trigger can consist of an in-time hit in only one scintillator paddle, or a coincidence of scintillator hits in a road. Wire hits in the A-layer are likewise made up of roads based on the probable trajectories (from Monte Carlo) that a muon might travel leaving the interaction region. The muon trigger can also receive tracks from the fiber tracker in time to make a decision at Level 1. Otherwise, the only momentum measurement possible for Level 1 muon is if a coincidence of scintillators inside and outside the toroid is required, which implicitly requires that the muon have been of at least 3 GeV/c in transverse momentum.

- Central Tracks: As previously mentioned (in Section 3.2.1), the central track trigger functions to provide information at Level 1 about the number and momentum of tracks in each event. Tracks are made available within the eight layer coverage of the CFT axial instrumentation, in 4.5 degree sectors of ϕ. In each sector, a number of tracks above each of the four thresholds (1.5, 3, 5, 10 GeV/c) is found based on the FPGA pre-programmed roads. This information is made available directly at Level 1, and also forwarded to the Level 1 Muon system, which represents the only cross-detector information available at Level 1.

With these quantities, a gross determination of whether or not an event is interesting for physics study may be made. Other events can also be selected at Level 1 for studies. Simply reading out the detector on the crossing clock (at a low rate) gives an unbiased look at the state of the the instrumentation. These are known as zero bias events. Hits may be required in the luminosity system as well, which requires there to have been at least some activity in the interaction region, without biasing the event by requiring other detector quantities*. These are known as minimum bias events. These events have been shown to be useful for examining data quality in the

*The luminosity system is an array of scintillating tiles located on the inside of the endcap calorimeters. The scintillators function to record hits of particles from the Tevatron beam crossings, from which the integrated luminosity may be calculated. Coincidences between the scintillators at the north and south detectors can roughly determine the position of the interaction, known as a 'fast z' requirement.

calorimeter.

Level 2

At Level 2, a more sophisticated (though still rough) treatment of the detector quantities within the event may be made. Only slightly more information is available at Level 2 than at Level 1. The advantage at Level 2 is that rough trigger level information for detectors may be combined to give more discrimination power.

- Information about the Level 1 calorimeter tower energies may be grouped into clusters (of towers). Quantities such as electromagnetic fraction and width (in towers) may be calculated. The sum of the E_T of these clustered towers can be calculated and thresholds assigned.

- Axial tracks from the Central Track Trigger are made available for matching with calorimeter objects. Three dimensional preshower objects are also available.

- In the muon system, pre-processed information from the readout is assembled into stubs in each of the different layers. Look-up tables provide a p_T measurement for those muon tracks that have hits inside and outside of the toroid.

- Roads from the axial only central track trigger are sent to special sextant cards that search through the indicated roads for hits representative of tracks in the silicon detector.

Level 3

At Level 3 the events from the detector undergo a fast reconstruction, akin to the full reconstruction that is carried out offline. The full detector information is available, including hits from the trackers, the full calorimeter precision readout, and muon system information. Generally, a Level 3 trigger fires if an object of the required type is reconstructed, such as a track above 10 GeV/c (using the entire tracker, silicon detector and fiber tracker), or a calorimeter cluster greater than 5 GeV (using the cell level readout information). Level 3 algorithms are required to run as fast as possible, with the greatest efficiency possible.

Chapter 4
Reconstruction

An overview of the software used in the reconstruction of detector quantities at DØ is presented. Each topic could easily occupy an entire volume in its own right, so only those quantities most germane to the analysis are studied in detail. Where possible, other sources of documentation on the individual packages have been referenced. All of this information pertains to production version 14 of the DØRECO (reconstruction) program.

4.1 Muon Reconstruction

Muons are reconstructed from hits in the muon chambers. The hybrid system of proportional drift tubes and scintillators serves a dual purpose. First, to ensure the proper measurement of the position of the particle before and after the toroid. Second, that the particle is in time with the beam crossing (and not from noise related or cosmic backgrounds).

There are both physics and instrumental backgrounds to reconstructing muons from collisions. Scattering of protons from the beam pipe or magnets further down the Tevatron tunnel can provide real muons that are not from the collision at the interaction region. Also, the ceiling of the collision hall has been exposed to beam losses from the Tevatron, and is radioactive, giving a background in the outer cham-

bers (low energy photons from the ceiling activity). The calorimeter is made of depleted uranium, which is decaying and giving off secondary particles that give rise to a background in the innermost chambers. The timing information for muons (from the scintillators) reduces both of these backgrounds by a large fraction.

Given these backgrounds, hits in the muon system that occur within the crossing time of the beam, are first associated into what are called 'segments' at each layer (see [18] for a full discussion on how segments are formed). Basically, muon segments are constructed by considering hits in each plane of the wire chambers first. Each hit in a proportional drift tube is effectively a circle (see Figure 4.1), since the actual particle track may have passed anywhere in the plane about the hit with the proper time. The hits are transformed into a local Cartesian coordinate system in which the wire direction lies along the z axis, with the plane in which the wires are located is parallel to the y-axis. This is done so that regardless of the orientation in the global coordinate system, the same segment algorithm can be used. The hits are grouped by wire chamber at this point (see Figure 3.9 for the locations and number of chambers). Next, all possible two hit connections (local segments) are created according to the following criteria:

- The two hits must not be on the same drift circle (must be two separate hits).
- The separation between both hits in the y-direction may not be more than 20cm.

- Both hits are not on the same plane unless they come from two neighboring hits, and one is at the top of a drift circle and the other is at the bottom.

After all two hit combinations have been made, the local segments are looped over and combined with other local segments to create new segments, with three or more hits. After all possible segments are matched (where the matching proceeds from left to right to cut down on combinatorics) each set of hits is fit to a line in two dimensions (x-y). The χ^2 of this fit along with the number of hits is used to filter down to the four best segments, where a better segment has more hits, or if two segments have the same number of hits, the one with the smaller χ^2 is chosen.

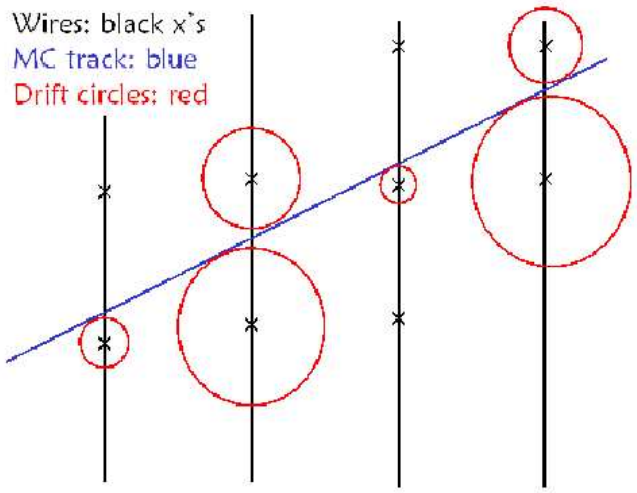

Figure 4.1 An Example of Segment Construction from Drift Hits.

Segments are then associated with scintillator hits in the vicinity and re-fit. These

segments are then looped over in a list, and the best matches between segments at the A-layer, and segments in the B- or C- layers are re-fit into tracks (see [19] for a technical description). These tracks give a measurement of the p_T of the muon, though this measurement is limited in resolution at low energy (under approximately 6 GeV) due to multiple scattering in the iron of the toroid, and at high energy(above 10 GeV) due to the finite position resolution of the chambers themselves.

4.1.1 Track Association

Once the reconstruction has been completed in the muon system itself, tracks from the central tracking volume are associated (if possible) with the muon tracks. Segments can also be associated with central tracks. This allows muons that do not penetrate the toroid to be identified, and used for analysis, with the momentum measured by the tracker. Such 'A-Stub' muons are valuable in analyses that require muons below 3 GeV to be reconstructed. Depending on the quality of the muon in the muon system, tracks may be associated in one of two ways.

Muon to Central Matching

If two or more segments have successfully been fit into a muon track (meaning the fit to segments inside and outside the toroid has converged), then the Muon-to-Central "Saclay" match will be attempted. Using the position, momentum, and associated

errors on each, the error matrix for the measured muon track may be calculated:

$$E_{6x6} = \begin{pmatrix} E_{3x3}^{PP} & E_{3x3}^{PX} \\ E_{3x3}^{XP} & E_{3x3}^{XX} \end{pmatrix}.$$

Here, E^{PP} is the error matrix for the momentum defined as $E^{PP} =< \delta p^T(\delta p) >$, where δ stands for the difference with respect to the mean value $\delta p = p - < p >$. Using the errors from the muon system track, and the like errors from the central tracker parameters, it has been shown that the final combined muon-central tracker parameters and errors may be found [21].

Central to Muon Matching

If the muon system reconstruction did not produce a converged fit then tracks from the central tracking volume are propagated to the A-layer of the muon system. Only tracks of greater than 2 GeV in momentum are used in this propagation. All tracks within $\Delta\phi < 1$ and $\Delta\theta < 1$ are associated with the muon, but only the best (meaning the closest) is selected as the proper track to associate with the muon. Using the same method as previously cited, only beginning with the central track instead of the muon, the parameters are propagated to the A-layer of the muon system. In this case no attempt is made to merge the local track fit and the fit from the central track, and thus the central tracker momentum is used.

4.1.2 Muon Identification Definitions

The Muon Algorithm group at DØ certifies common definitions of the different qualities of reconstructed muons in the detector. A brief summary of the quality definition for muons used in this analysis is included here (see [20] for full details).

'Medium' quality muons (which are the quality selected for the analysis) are in general reconstructed muon tracks with hits both inside and outside of the toroid. These muon tracks are required to satisfy the following conditions:

- Scintillator Hit at the A-layer.
- At least two A-layer wire hits.
- Scintillator Hit at the B- or C- layer.
- At least two B- or C- layer wire hits.

An exception to these requirements is made in the bottom of the central muon system if a central track is matched. The physical support for the calorimeter requires that the muon instrumentation be sparse in these octants (octants 6 and 7), and thus these requirements are relaxed to allow for a more uniform reconstruction efficiency over the detector ϕ of the muon system. Muons satisfying only the A-layer or only the BC-layer requirements in the bottom of the detector, and matched to central tracks are also defined to be medium.

The invariant mass of Z$\rightarrow \mu\mu$ events from data, using the central track information is shown in Figure 4.2. The resolution, using the width and position of the peak of the invariant mass has been parametrized. The form of the parametrization is based on the expected resolution given multiple scattering (through Coulomb repulsion) and tracker position resolution. The parametrization, as well as the effect that the resolution has on the Wγ analysis is given in Section 6.1.4.

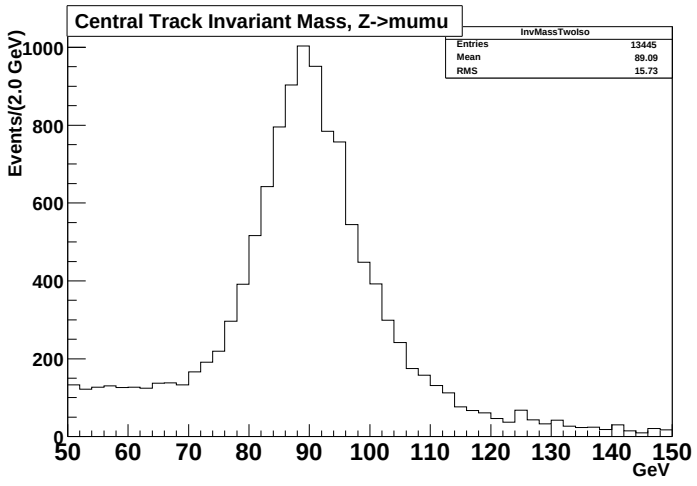

Figure 4.2 Invariant mass for Z$\rightarrow \mu\mu$ from central tracks.

The resolution for the muon system estimate of the transverse momentum has also been parametrized, using dimuon events. The invariant mass for Z$\rightarrow \mu\mu$ events within the peak (between 70-120 GeV) in Figure 4.2 is shown in Figure 4.3. The parametrization, as well as the effect that the resolution has on the Wγ analysis is given in Section 6.1.4. The resolution of the momentum for these high p_T muons

is dominated by the position resolution of the muon system chambers (though contributions from multiple scattering and energy loss prior to the muon system are included). However, as the invariant mass shows for muons that are high p_T (such as from Z$\rightarrow \mu\mu$), the muon system seldom reconstructs a low value. Thus the muon system may be used for confirmation that the central tracker has correctly identified the muon as high p_T*.

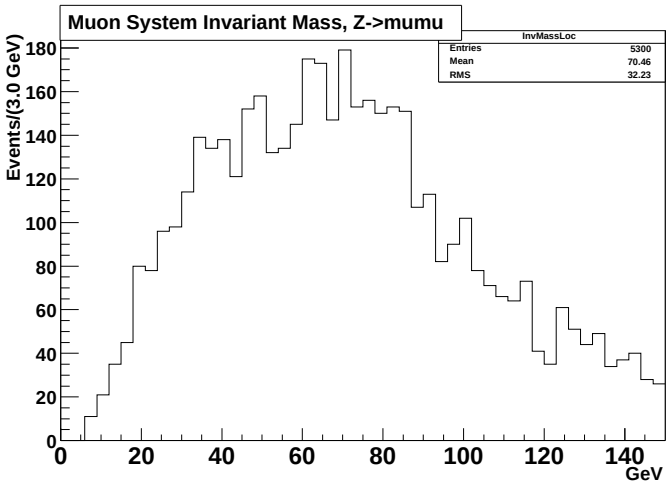

Figure 4.3 Invariant mass for Z$\rightarrow \mu\mu$ from Muon System Only.

*In the case of in flight decays (such as π or K to μ) the central track of the initial particle with decay may be misreconstructed. The 'kink' in the track may cause the central track to be reconstructed as high p_T, which is then mis-associated with the muon. The muon system however, will only see the low momentum muon from the decay. Thus by using both the central tracker and muon system information (though not combining them) a more effective selection may be made.

4.2 Electromagnetic Object Reconstruction

Electromagnetic showers should be tightly clustered in the electromagnetic portion of the calorimeter. The dominant showering mechanism for photons is e^+e^- pair production. For electrons (or positrons) the mechanism is bremsstrahlung (braking radiation). Thus a photon or an electron entering the calorimeter results in a shower of electromagnetic particles which terminates when the final produced particles lack the energy to continue the process of showering. The depth of the electromagnetic calorimeter (in radiation lengths as described in 3.2.2) implies that almost all electromagnetic showers will be completely contained within the electromagnetic calorimeter. In contrast, hadronic showers will in general deposit energy in both the electromagnetic portion of the calorimeter and the hadronic portion (since the scale is set by the nuclear interaction length (λ_b), unless the shower develops early on into multiple $\pi^0 \rightarrow \gamma\gamma$ which would give rise to an electromagnetic signature, though wider in width (due to multiple photons).

4.2.1 Simple Cone Algorithm

For the analysis detailed in this thesis, electromagnetic objects are identified by first considering quantities within the electromagnetic layers of the calorimeter. Another algorithm, which begins with tracks and preshower information is also available,

but not used for this analysis*.

The algorithm receives a list all towers of non-zero energy, which are ordered in decreasing energy. The list is looped over, searching for a tower above the threshold of 500 MeV. If a tower contains a cell in the Coarse Hadronic layer of the calorimeter, this cell's energy is discarded and the tower energy is recomputed.

When a tower above threshold is found:

- A cone of dR=0.4 is drawn about the seed tower $\eta - \phi$ position.
- Towers other than the seed within this cone are then looped over.
- If another tower is found within this cone, the tower is added to the cluster and the $\eta - \phi$ position is recalculated. The dR=0.4 circle is drawn again, around the new position, and the remaining towers are looped over. This process continues until all possible towers have been added. Finished clusters must contain at least two towers and have an E_T of greater than 1 GeV. The list of 'simple cone' clusters is then sent for processing to the electromagnetic reconstruction program.

Each cluster in the list must then pass more stringent requirements. The energy must be at least 1.5 GeV, and the ratio of energy deposited in the electromagnetic calorimeter to the total cluster energy must be at least 0.9. Then a large window, of

*Much of the information in this section comes from [22]. Some however was found by delving into the code itself and the reconstruction parameters.

radius 4 calorimeter towers (an example of a window of towers is shown in Figure 4.5), about the highest energy tower in the cluster is taken, and a list of those towers made. The isolation, as shown in Figure 4.4 is then calculated. The total energy in the towers in the large window is first computed. Then the sum of just the electromagnetic energy deposited in a cone of ΔR=0.2 is computed, and the isolation formed:

$$isolation = \frac{E_{TOT}(0.4) - E_{EM}(0.2)}{E_{EM}(0.2)} \tag{4.1}$$

The closer the isolation is to zero, the more tightly the width of the cluster is constrained. This helps discriminate between clusters which are formed by hadronic showers and clusters which originate from single photons. For the candidate cluster to be selected as an electromagnetic object by the reconstruction, the isolation must be smaller than 0.2.

4.2.2 Electromagnetic Energy Scale

The energy scale of the electromagnetic portion of the calorimeter is set using data from reconstructed Z→ee events. Using DØGEANT Monte Carlo events, individual layer weights (corresponding to the amount of charge collected) for the electromagnetic calorimeter are developed, by minimizing the following equation:

$$\chi^2 = \sum_{events} (E_{true} - \sum_{i=1}^{4} a_i L_i)^2. \tag{4.2}$$

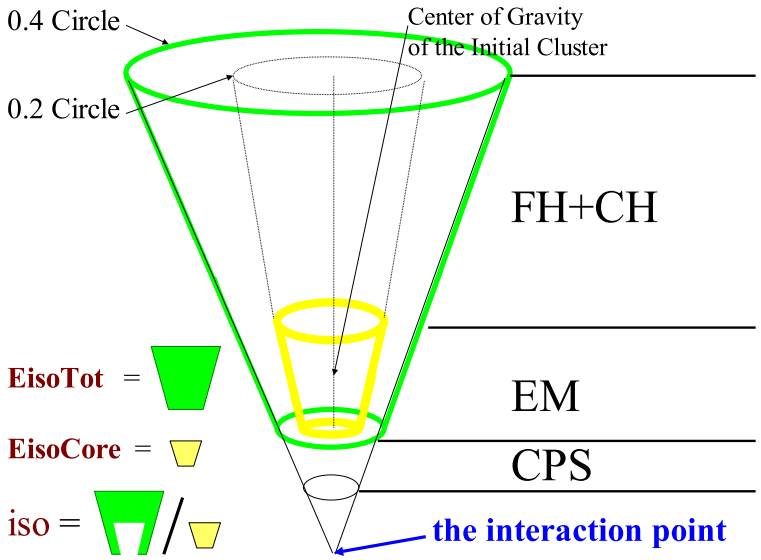

Figure 4.4 Schematic of Isolation for the Simple Cone Algorithm.

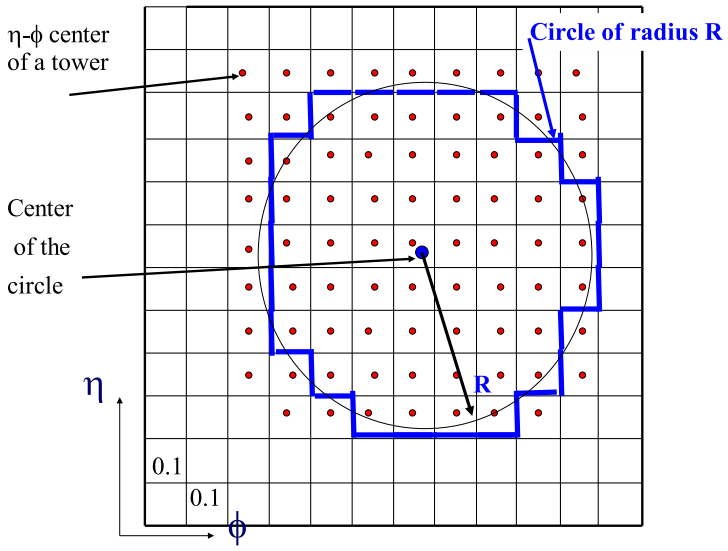

Figure 4.5 A Circle of Towers in η-ϕ space.

L_i is the energy deposited in the liquid argon in layer i, and a_i is the sampling weight. These layer weights are tuned such that the best resolution (or width of the peak) may be obtained by weighting the layers of the calorimeter more that sampled more of the energy of the shower. The absolute scale for the calorimeter is set using the Z→ee peak in data.

The invariant mass for Z→ ee events in data is shown in Figure 4.6. From the width and position of the peak, the resolution for the electromagnetic calorimeter has been parametrized. The parametrization, as well as the effect of the resolution on the Wγ analysis is described in Section 6.1.4.

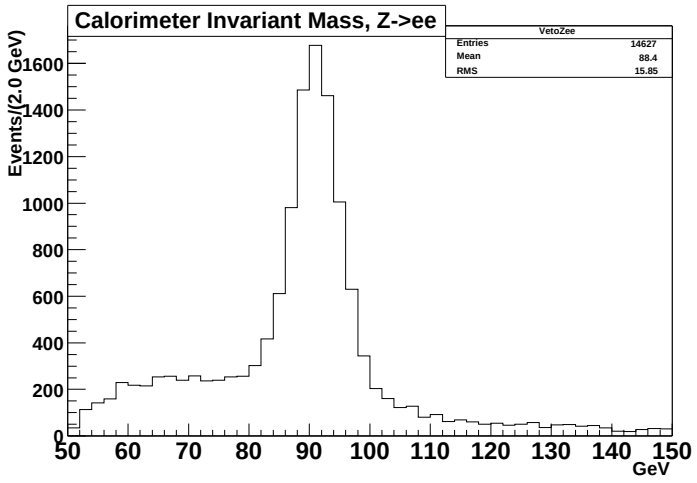

Figure 4.6 Invariant mass for Z→ *ee* from calorimeter.

The central and forward preshower detectors are not integrated into this energy measurement as of the writing of this thesis. This results in a larger weight for the

first layer of the electromagnetic calorimeter. This weighting is due to the fact that electromagnetic showers will begin earlier with respect to the first calorimeter layer, because of the additional material of tracker, solenoid, and lead.

4.2.3 Electromagnetic Identification Quantities

Several quantities are used to discriminate between electromagnetic objects (such as electrons and photons), and backgrounds (such as multiple π^0, $\pi^{\pm}$ that undergo charge exchange, *etc*). The isolation, as calculated in Section 4.2.1, is used. The electromagnetic fraction as calculated from the cells (as opposed to towers) is also used. Additional variables such as shower widths and derived quantities may also provide discrimination.

The width of an electromagnetic shower in ϕ is defined as:

$$\sigma_{r\phi} = \sum_{i=0}^{N} \frac{E_i \times R^2 \times sin^2(\phi_C - \phi_i)}{E_C} \tag{4.3}$$

The sum in Equation 4.3 is over the number of cells in the electromagnetic cluster. E_C and ϕ_C are the cluster energy and energy weighted ϕ of the cluster ($\phi_C = \frac{\sum_{i=0}^{N} E_i \phi_i}{\sum_{i=0}^{N} E_i}$, where again this is a sum over the cells in the cluster.). E_i and ϕ_i are the individual cell quantities. A similar quantity for the width in z is also available. In Monte Carlo comparisons to data for electrons, the $\phi-$width is shown to be modeled well, while the z-width is not.

An additional variable, known as the HMatrix is also used. The HMatrix is a

discriminant variable based on the shower profile of electrons in Monte Carlo. Eight variables are used to construct a covariance matrix in a large energy range, in the following way:

$$M_{ij} = \frac{1}{N}\sum_{n=1}^{N}(x_i^n - \overline{x}_i)(x_j^n - \overline{x}_j), \tag{4.4}$$

where N is the sum over the reference Monte Carlo electrons, x_i is the value of variable x, and $\overline{x_i}$ is the mean of variable x_i. variables. The HMatrix χ^2 is then constructed:

$$\chi^2_{HM} = \sum_{i,j=1}^{8}(x_i^{'} - \overline{x}_i)H_{ij}(x_j^{'} - \overline{x}_j) \tag{4.5}$$

In Equation 4.5, $x_i^{'}$ is the data value of variable x_i, $\overline{x}_i$ is the mean of the variable x_i from Monte Carlo, and the matrix H is the inverse of the covariance matrix M_{ij}. A shower that closely resembles one of the electromagnetic showers from Monte Carlo will have a low χ^2. The eight correlated observables are used for shower shape analysis are:

- The fraction of energy deposited in each of the layers of the electromagnetic calorimeter.
- The total electromagnetic energy.
- The energy weighted transverse shower width in z and ϕ.
- The z vertex distribution.

The HMatrix is constructed using Monte Carlo electron events, and thus is not used for photon selection. Instead the variable that showed both the best agreement with Monte Carlo in data, and the most discrimination, was used: the $\phi-$width of the cluster at the third floor of the calorimeter, as defined in Equation 4.3* .

Track match quantities are useful for identifying electrons and photons. In the case of electrons, the better the match of a single track to the electromagnetic cluster, the less likely the cluster is to originate from a QCD jet (since jets commonly have many tracks). For photons, isolation from surrounding tracks decreases the probability that the object originates from either QCD or electrons.

For track matching to electrons, there are two different χ^2 match probabilities. The first takes into account the position of a track with respect the the cluster in the calorimeter. Since no comparison is made between the momentum of the track and the energy in the calorimeter, this method suffers from a substantial mis-association rate, but has a high efficiency. The second combines the (non-gaussian) $\frac{E}{p}$ with the spatial match of the track-cluster pair for the the match χ^2. This yields a substantially lower fake rate, but is also substantially lower in efficiency both due to bremsstrahlung photons†, and tracker resolution. For photons, a track isolation is constructed, by requiring the sum of the momentum of tracks in a 'hollow cone' of dR(0.05-0.4) to

*For typical selection cuts to identify electrons, see Section 6.2.5. For the photon selection cuts for the Wγ analysis, see Section 5.2.

†In the case of bremsstrahlung, the energy of the cluster would be correctly measured as the photon would likely be included by the cone algorithm. The momentum of the electron track however, would be different.

be smaller than a certain threshold cut. This allows discrimination between jets and photons, but allows for the possibility that photon conversion might provide tracks in the center of the cone.

4.3 Jet Reconstruction

4.3.1 Run II Cone Algorithm

The jet reconstruction algorithm used at DØ is similar to the algorithm described in Section 4.2.1. There are several important differences. Electromagnetic showers all share some similar characteristics. For example the transverse development of an electromagnetic shower (from an electron or photon) scales with the Moliere radius:

$$R_M = X_0 \times \frac{E_S}{E_C}, \tag{4.6}$$

where X_0 is the radiation length of the material, E_S is the scale energy (≈ 21 MeV) and E_C is the critical energy, which depends on the atomic number of the material. Roughly 99% of the energy in an electromagnetic shower is contained within 3.5 R_M [23]. However, there is no such restriction on jets, as the width will depend strongly on how the quarks hadronize. In order to deal with these differences, and still find stable jets, additional support in the algorithm is needed [24].

The goal of a cone algorithm is to find jets from detector quantities in such a way that the resultant detector objects may be compared with what is predicted from theoretical models (reconstructed jets, though consisting of many constituent

particles, should possess the same energy as the initially produced quark). The Run II Cone Jet algorithm begins with a cone of radius 0.5, as opposed to that of the photon reconstruction. A list of seed towers in the calorimeter is used to limit the amount of processing time spent on the reconstruction (minimum E_T 500 MeV). For each seed tower in the list, a 'proto-jet' is created, using an iterative algorithm about the tower (as in Section 4.2.1). If the final stable cone from this iteration is not already reconstructed, then this cluster is sent on to determine if it is part of another, larger jet, or is already too large and must be split into two jets.

The so-called 'split-merge' algorithm is used in the case where 'proto-jets' share towers. An E_T ordered list is made of the cone jets found in the clustering, and the algorithm works down the list. If a 'proto-jet' shares no towers with any other cluster, then it becomes a jet (no ambiguity). If the candidate does share towers with other jets, then each is considered separately. If the energy shared with the lower E_T jet is greater than half the energy of the other jet, then the two jets are merged (the algorithm assumes that the two 'proto-jets' are made of energy originating from a single real jet). If the energy is less than half, then the jets are split apart, with the shared cells being assigned to the nearest jet (algorithm assumes that there were initially two real jets nearby). The energies of the two jets are recalculated, and the list of jets is remade (since the E_T ordering may have changed). This continues until no further towers are shared.

4.3.2 Jet Energy Scale

The energy scale for the hadronic portion of the calorimeter is set using jet events in which a photon is reconstructed back to back with a jet. Since the electromagnetic energy scale is set using the Z boson mass, the energy scale for the hadronic may be set by requiring the electromagnetic energy in these events to balance that of the energy reconstructed in the jet. This method has the advantage of using the well known energy scale of the electromagnetic calorimeter to get an energy scale from the data. The disadvantage however, is that the jet energy scale will be limited by the number of these photon+jet events found in data. Also, if a 'photon plus jet' is in reality an electron plus jet, the energy should not balance (a single electron implies the presence of a neutrino, and thus missing transverse energy). Fundamentally, this also limits the understanding of the hadronic energy scale to the understanding of the electromagnetic calorimeter.

Corrections to the jet energy scale are made at the level of reconstructed jets. These corrections at low transverse energy are large, and also uncertain. When jets are used in the analysis for the estimation of the background, this uncertainty will be addressed.

4.3.3 Jet Identification Quantities

The quantities used to reconstruct jets in data (*i.e.* to separate real quark and gluon jets from noise) are listed here.

- JetCHF: The fraction of energy within the jet which is deposited in the coarse hadronic layer of the calorimeter.
- JetEMF: The fraction of energy within the jet which is deposited in the electromagnetic layers of the calorimeter.
- Jetn90: The number of towers which contain 90% of the jet's energy.
- JetHOTF: The ratio of the highest E_T cell in the jet to the second highest E_T cell in the jet.
- Jetf90: The ratio of the number of towers containing 90% of the energy in the jet to the total number of towers in the jet.

Cuts made on these quantities are mainly made so that the jet reconstruction will not re-find objects that were selected by the electromagnetic reconstruction, and to limit the number of false jets (caused by cells with large pedestal variations, drift of pedestals, miscalibration). For the purposes of the Wγ analysis, reconstructed jets are also limited to the η coverage of the calorimeter, the boundary between the

central and endcap cryostats is not used. For the cuts used to identify jets in the Wγ analysis, see Section 7.1.1.

4.4 Track Reconstruction

The offline track reconstruction used for the Wγ analysis is an algorithm that was initially developed for detector alignment [25]. The track finding attempts to find tracks beginning in the Silicon Microstrip Tracker, creating a pool of track hypotheses as it works outward in increasing radius. These hypotheses are then filtered down by quality criteria.

Initial tracks are made up of at least three hit tracks in the silicon. The first measurement can be in any of the layers of the barrels, or F-disks. The second measurement is selected in any successive layer, provided that the angle between the first and second point is smaller than $\Delta\phi$=0.08. The third measurement is selected in any layer following the second, provided that the radius of curvature of a circle through the selected hits is greater than 30 cm (in p_T, 180 MeV). The axial impact parameter (the distance of closest approach to the origin of coordinates) of these three hits must be smaller than 2.5 cm, which is equivalent to requiring the track to have come from somewhere within the beam spot. A fit to the initial track hypothesis* is required to have $\chi^2 < 16$. These track hypotheses are extrapolated to the rest of the silicon and the fiber tracker. Hits may then be associated if the match to the fit track

*The initial track hypothesis is a circle in the axial plane, which passes through the initial three points. See Figure 4.7.

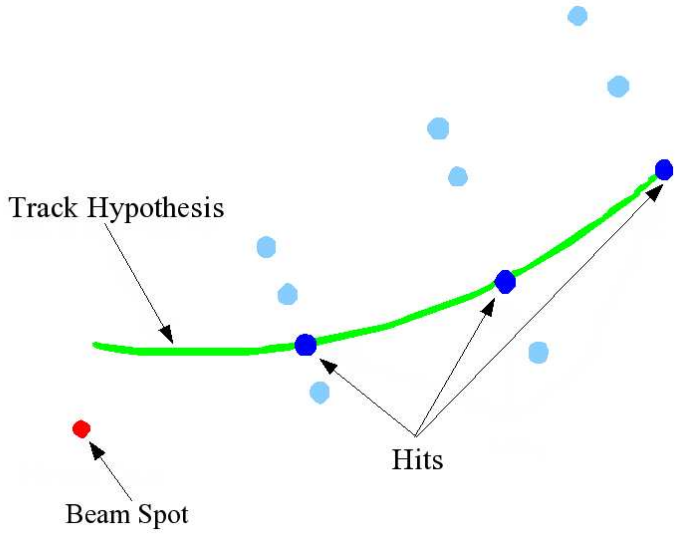

Figure 4.7 Initial Track Hypothesis.

is smaller than the previously mentioned $\chi^2 < 16$. If there are multiple hits within the window in a layer, the hypothesis is split, and each investigated as a unique track. Hits can be missed at any layer†.

These track hypotheses are then filtered down, using requirements on the track hypotheses:

- At least four detectors (where a detector is a single side of a silicon strip, or a single ribbon of the CFT), must be hit, and there must be both axial and stereo hits (no two dimensional tracks).

†Whether or not a layer (meaning a single side of an SMT strip, or single ribbon of CFT), is 'on' (readout enabled) is determined by the presence or absence of other hits outside the window in the detector. Thus if a CFT ribbon does not have a hit where the track hypothesis expects, it is not counted as a miss, unless there are other hits in that ribbon that indicate that it is enabled.

- There may be no more than three misses inside a track. An example of a valid track could then be that there were four hits within the silicon, then two misses, and then a miss at the first layer of the CFT, and then all other layers are hit. If the second layer of the CFT was also missed (which would be four hits) the track is discarded. A track may not have more than six total misses.

- No more than two inside misses in the SMT. For instance, a single hit, then two misses, and two more successive hits is fine, but three misses is not.

- $\frac{N_{hits}}{5} <= N_{miss}$

- Hits may be shared in the axial plane for different stereo projections, but:

  † $N_{shared} < \frac{2}{3} \times N_{tot}$

  † $N_{shared} < \frac{1}{5} \times N_{tot}$ OR $N_{tot} - N_{shared} > 3$

The position of vertices is then determined by the reconstructed tracks. This is done by first attempting to associate tracks with the beam spot position (within 0.1 cm in z position and 0.2 in DCA). Then other tracks are grouped together, and fit together (in much the same way as in Section 4.5). The χ^2 in this case is reduced by filtering out the tracks included in the vertex itself. In order to be identified as a vertex by the tracking software, there must be at least five tracks, which have a $\chi^2 < 36$. Then, a second pass is made over unused hits, and tracks that do not have silicon

may be reconstructed within the fiber tracker, but only if they are consistent with a vertex position (this significantly reduces the combinatorics of the problem). For the purposes of analysis, tracks which do not have any silicon tracker hits are constrained to pass through the primary vertex (at the distance of closest approach). This gives an improvement in the p_T resolution as compared to the resolution of the fiber tracker alone. All remaining track hypotheses then have a final refitting performed to all of the associated hits that determines the track parameters such as η, ϕ, and curvature $(\frac{q}{p_T})$.

4.5 Vertex Reconstruction

The reconstruction of the event vertex is very important. In order to properly calculate transverse energies in the calorimeter (and missing transverse energy) the proper position along the z-axis must be reconstructed. In the Tevatron, the distribution of the interaction point in z is spread out in a Gaussian distribution, typically with a width of at least 20 cm.

The vertex position is determined in a two pass method [26]. The first pass basically loops over all tracks in an event of $p_T > 0.5$ GeV and clusters them in candidate vertex positions in z. The x-, y-, and z-position of the track parameters for each of the associated tracks (at the distance of closest approach) are then used in a fit to better ascertain the position the vertex. The goal is to determine the vertex position $\mathbf{x}$=(x, y, z) by using the information from the clustered tracks, and better

determine their momentum by constraining them to this vertex.

Vertex fitting is done using a modified Kalman Filter algorithm, which relies on a fast least squares fit rather than a recursive fitting approach. If one defines:

$\mathbf{d}^m = \begin{pmatrix} \mathbf{m}_1 \\ \\ \mathbf{m}_2 \end{pmatrix}$ where $\mathbf{m}_k$ is the vector of track parameters* ,

$V = \begin{pmatrix} V_1 & 0 \\ \\ 0 & V_2 \end{pmatrix}$ the covariance matrix,

$W = \begin{pmatrix} W_1 & 0 \\ \\ 0 & W_2 \end{pmatrix}$ the weight matrix ($\mathrm{W}_i = \mathrm{V}_i^{-1}$), and

$\mathbf{q} = \begin{pmatrix} \mathbf{x} \\ \\ \mathbf{q}_1 \\ \\ \mathbf{q}_2 \end{pmatrix}$, which is the vector of vertex parameters, and momentum of tracks associated with the vertex, then the goal of the least squares fit is to minimize:

$$\chi^2 = (\mathbf{d}^m - \mathbf{d}(\mathbf{q}))^T W (\mathbf{d}^m - \mathbf{d}(\mathbf{q})), \tag{4.7}$$

For more information on the minimization, see [26].

In the first pass, candidate tracks to be associated with the vertices must pass a loose selection cut of $\frac{dca}{\sigma} < 100$ with respect to the center of the detector in (x,y) (here σ is the error on the position, $\frac{dca}{\sigma}$ is sometimes called the DCA significance). In

*Tracks are given as a function of five parameters: z, ϕ, tan(λ), distance of closest approach to the origin, and the curvature ($\frac{q}{p_T}$).

the second pass, the cuts on tracks selected to be attached to the vertices is tightened to $\frac{dca}{\sigma} < 3$, where instead of the center of the detector, the beam spot position that is found using the first pass list of vertices is used instead.

This two-pass method gives a clean list of candidate vertices for each event. However, not all vertices may be from the collision that gave rise to the trigger for the event (additional interactions in the crossing may also be reconstructed. These are sometimes called 'minimum bias' events.). In order to select the primary vertex, the 'hard scatter' in the event, each vertex candidate in the event is characterized by the logarithm of the p_T of tracks that make up the vertex. For each track attached to the vertex with $p_T > 0.5$ GeV a probability for the track to have come from a minimum bias event is assigned based on $log_{10}p_T$:

$$P(p_T) = \frac{\int_{log_{10}(p_T)}^{\infty} F(p_T)dp_T}{\int_{log_{10}(0.5)}^{\infty} F(p_T)dp_T}. \tag{4.8}$$

In this equation, $F(p_T)$ is the minimum bias track $log_{10}p_T$ spectrum distribution obtained from Monte Carlo [27]. For each vertex, the product of the probabilities is formed and weighted by the number of tracks to make it independent of the number of tracks at the vertex, thus forming the probability for the candidate vertex to originate from a minimum bias event. Then the vertex with the lowest probability to be from a minimum bias event is selected as the primary vertex.

4.6 $\not\!\!E_T$ Reconstruction

At hadron colliders the energy of the colliding partons is not known precisely. This is due to the composite nature of the proton and the momentum distribution of the quarks within it. The transverse momentum at the interaction point is approximately zero, which implies that the transverse momentum of the particles produced in an interaction must sum to zero. The magnitude of the vector sum of the x- and y-components of the measured energy in an event may be calculated, and is balanced (by definition) by the missing transverse energy. The missing energy is rarely zero, due to resolution effects from the various detector components. However, in most events that do not have a neutrino this quantity should be small..

The missing transverse energy is reconstructed by first considering the energy depositions in the calorimeter on a cell by cell basis, with respect to the primary vertex.

$$E_{Tx} = \sum_{i=0}^{Ncells} E_i \times cos\theta_i \tag{4.9}$$

$$E_{Ty} = \sum_{i=0}^{Ncells} E_i \times sin\theta_i \tag{4.10}$$

$$\not\!\!E_{Tx} = -E_{Tx} \tag{4.11}$$

$$\not\!\!E_{Ty} = -E_{Ty} \tag{4.12}$$

$$\not\!\!E_T = \sqrt{\not\!\!E_{Tx}^{\ 2} + \not\!\!E_{Ty}^{\ 2}} \tag{4.13}$$

The sums in Equations 4.9 and 4.10 include all of the calorimeter cells above threshold,

excluding the coarse hadronic section. The coarse hadronic layer is not used due to a distortion effect caused by noise from this region (detailed in [28]). The removal of this layer leads to improvements of the $< \not\!\!E_T >$ component in x and y by approximately 500 MeV in each. The polar angle θ_i is calculated with respect to the primary vertex for each cell individually.

The net transverse energy in the x and y directions is calculated, and from these quantities the missing transverse energy (see Equations 4.11, 4.12 and 4.13). The momentum of any muons that are matched to central tracks is subtracted from this missing E_T, yielding the final quantity used in the analysis.

The missing transverse energy distribution in minimum bias events (defined in Section 3.2.4) is used as a check on the functionality of the calorimeter. If the distribution in a given run shows an excess of high missing E_T events, this may be an indication that either the calorimeter is not correctly reading out, or some problem in the electronics is present (such as a 'hot' cell, or a 'warm region' that would indicate pedestal drift). These problems are assessed on a 'luminosity block'* basis. If the distribution is shifted, or widened by an increase of high $\not\!\!E_T$ events, then the block will be marked bad, and the integrated luminosity from that data is excluded from analysis. The cuts used for marking a luminosity block bad are summarized in

*A luminosity block is a unit of time used by the luminosity system to measure the number of interactions that have occurred. It corresponds to approximately one minute of data taking. Since luminosity blocks are used to calculate the integrated luminosity, they correspond to the smallest amount of data one may exclude and still have a sample that may be properly normalized.

Table 4.1. These cuts eliminate approximately 5% of recorded luminosity.

Cut	Value
$<\not\!\!E_T>$	<4 GeV
RMS$_{\not\!\!E_T}$	<22 GeV
Scalar E_T	>80 GeV
Events	>500

Table 4.1 Luminosity Block Selection Cuts.

The final $\not\!\!E_T$ used in the Wγ analysis is corrected for electromagnetic objects that are good by the prescription listed in [29]. This is due to the fact that energy corrections are applied as a function of detector η for isolated electromagnetic objects, and thus need to be included in the final $\not\!\!E_T$.

Chapter 5
Selection

5.1 Muon Selection

5.1.1 Trigger

The first step to selection of W$\gamma \rightarrow \mu\nu\gamma$ events was the selection of high transverse momentum muons indicative of W decay. At the trigger level of the detector, only the muon was considered, removing the bias from quantities such as missing transverse energy and photon E_T.

Level 1 Trigger

Three separate triggers were used to select these events. The differences between the triggers constitute the continuing upgrades to the performance of the muon trigger systems, and the changes in instantaneous luminosity as the Tevatron performance continued to improve. One issue which was more or less constant was the amount of the total Level 1 trigger rate which was allocated to the single muon trigger. This sometimes necessitated prescaling of the trigger to reduce the rate (see Section 3.2.4).

The trigger in the earliest data simply required a coincidence between the A and C layer scintillators in the central, or A and B layers in the forward. This trigger was most often prescaled due to limited data acquisition bandwidth. Both the data acquisition system and accelerator performance varied throughout the data set, and thus many different prescale factors were used. These prescale factors have been

accounted for in the calculation of the integrated luminosity for the analysis.

Since the muons of interest are high transverse momentum, the implicit momentum cut (approximately 3 GeV/c) of requiring the muon to pass through the toroid is not an issue. The coincidence was required within the 'Wide' scintillator region, which covers approximately $|\eta_{detector}| < 1.5$. This region was designed to approximate the coverage of the full sixteen layers of the central fiber tracker. In this early data the luminosity system was required to reconstruct a z-vertex position within the detector. This was observed to slightly lower the Level 1 rate.

In later data (constituting approximately two-thirds of the dataset), a wire requirement was added to the Level 1 trigger. This required that wire hits in the decks of the A-layer of drift tubes were present along with the scintillator confirmation. This had the advantage of providing additional rejection to lower the Level 1 rate (effectively removing the prescale issue), even though this made the L1 trigger efficiency more dependent on the efficiency of each particular deck of proportional (or mini-) drift tubes at the A-layer. When the instantaneous luminosity was low enough ($2.5\times10^{31}\mathrm{cm}^{-2}\mathrm{s}^{-1}$), the trigger coverage was expanded to the full $|\eta| < 2.0$ coverage of the muon system. It is important to note that in no period of data taking could a muon in the 'hole' area of the muon system be triggered on, due to the lack of A-layer scintillator coverage with which to construct a tight scintillator trigger (see Section 3.2.3). In the future, with the addition of the requirement of a central track

at Level 1 in that region, a loose scintillator trigger could be constructed, though that is beyond this scope of this analysis.

Level 2

At Level 2, requirements also changed with time. In the first period of data taking, a 'Medium' quality muon was required to be present with a transverse momentum measured by the toroid (as acquired from the look-up tables, see Section 3.2.4) of greater than 5 GeV/c. The look-up tables at that time were not optimized (using data), and thus incurred some inefficiency. In later periods of data taking, coinciding with the application of the wire hits at Level 1, the look-up tables were updated, and the threshold lowered to 3 GeV/c.

A 'Medium' muon reconstructed at Level 2 required at least loose stubs in the A- and BC-layer wire chambers to be reconstructed. These stubs were defined to be:

- Forward A Layer: At least two decks of mini-drift tubes hit, and an associated scintillator hit (note that tighter criteria could have three decks hit without the scintillator requirement).
- Forward BC Layer: At least two wire hits in either B or C layer decks.
- Central A Layer: At least three hits (not decks) with valid look-up table pattern.
- Central BC Layer: At least three hits in any combination of B or C layer.

These cuts constitute the loosest quality muon at Level 2 that would have an estimate of the transverse momentum from the toroid.

For the first period of data taking, a medium muon at Level 2 was effectively wire confirmation at the A-layer and at the B- or C-layers, as well as an explicit p_T cut. In later periods of data taking, the wire hits at the A-layer were already required, and thus most of the rejection came from the p_T cut.

Level 3

At Level 3, for the different periods of data taking the same filter was required. Unlike Level 1 and Level 2, there were no muon specific cuts applied. Instead, a track with greater than 10 GeV/c transverse momentum was required to be reconstructed. This track was not required to be associated with the muon, as the rejection was found to be sufficient without any further cuts that could decrease the efficiency.

The Level 3 track tool starts from the outer axial layers of the central fiber tracker. The tool has a minimum p_T of 1.0 GeV/c, and thus tracks will not show a great deal of curvature. The difference in ϕ between two layers then is approximated by:

$$\phi(r) = \phi_0 + ar, \tag{5.1}$$

where ϕ_0 is the track ϕ at the distance of closest approach, a is proportional to the inverse transverse momentum and r is the radius. Inside the outer two layers, hits are assigned based on the extrapolation from only the previous layers via a linear

extrapolation:

$$\phi_i = \phi_{i-1} + (\phi_{i-1} - \phi_{i-2})\frac{r_i - r_{i-1}}{r_{i-1} - r_{i-2}}, \tag{5.2}$$

where ϕ_i is the predicted position at the next layer radius r_i and (r_{i-1},ϕ_{i-1}), (r_{i-2},ϕ_{i-2}) are the previous two positions found. At least seven out of the eight axial layers are required to have had hits found. The algorithm then attempts to associate silicon hits, and hits from the stereo layers of the tracker [30]. A track that is made up solely of axial fiber tracker hits is still high enough quality to satisfy the filter. From the curvature of the track, the p_T is measured, and if greater than 10 GeV/c the event is written out.

It is important to note that only tracks within the full fiducial coverage of the fiber tracker ($\eta_{detector} < 1.6$) are reconstructed at Level 3. Thus there are still some events in which the muon is triggered on at Level 1 and Level 2, yet the track does not cross enough of the tracker to get reconstructed and thus is not written out. The inclusion of the coverage of the full muon system does help however, since muons originating from the far ends of the interaction region may cross the entire fiber tracker and be found in the muon system at $|\eta_{detector}| > 1.6$.

5.1.2 Muon Quality

After all trigger requirements have been fulfilled, a series of additional cuts are applied on the offline quality of the muon and associated central track.

- The offline reconstruction must have found a 'Medium' quality muon (as defined in Section 4.1.2) matched to a central track.

- The central track must be measured to be greater than 20 GeV/c in transverse momentum.

- The muon system must reconstruct the transverse momentum of the muon to be above 8 GeV/c.

- The muon and central track must be within the volume of the detector defined by the Level 3 track trigger ($\eta_{detectorCFT}$ <1.6), and not in the 'hole' area as described in Section 3.2.3.

- The reconstructed distance of closest approach to the beam line (DCA) for the central track must be smaller than 0.20 cm.

- The muon must be isolated in both the calorimeter and the tracker, as per the following cuts:

  † The sum of the E_T in the calorimeter, between a cone of 0.1 and 0.4 about the muon direction must be smaller than 2.5 GeV.

  † The transverse momentum sum of tracks in a 0.5 cone about the muon must be smaller than 3.5 GeV/c.

- No additional 'Medium' quality muons are allowed to be present, nor is any additional track of $p_T > 15$ GeV/c, within the coverage of the CFT ($\eta_{detectorCFT}$ <1.8).

The cut on the DCA of the track matched to the muon is to ensure that the muon originated from the beam line (not a cosmic, or background muon from the Tevatron tunnel). The isolation and transverse momentum requirements are made to select muon candidates that are likely from W decays (and not muons from other sources such as heavy flavor, or decay in flight). The veto on high p_T tracks and additional muons is made to reduce backgrounds from Zγ production.

5.2 Photon Selection

The reconstruction for isolated electromagnetic objects is detailed in Section 4.2. For this analysis, photon candidates were required to pass the following selection criteria:

- At least one EM object as selected by the simple cone algorithm.
- EM object is reconstructed in the central calorimeter, $|\eta| < 1.1$.
- Transverse energy greater than 8 GeV.
- Fraction of energy in the electromagnetic calorimeter greater than 90%.
- Object is not reconstructed as being within the module boundaries of the central calorimeter as defined in Section 3.2.2.

- Isolation about the central cone of the object is smaller than 0.15.
- Azimuthal width of the cluster in the third layer of the electromagnetic calorimeter must be smaller than 14 cm^2 (as defined in Section 4.2.3).
- Sum of the p_T of tracks in a hollow cone of dR(0.4-0.05) must be smaller than 2 GeV/c.
- The spatial track match χ^2 as described in Section 4.2.3 must be smaller than 0.001.

These cuts are made mainly to limit the number of jets from QCD that are misidentified as photons. The track isolation requirement is made to not only to limit the amount of jet contamination, but also possible contamination from electrons.

5.3 Kinematic Selection

Besides the selection cuts on the muon and the photon, missing transverse energy consistent with the escape of the neutrino is required. The $\not\!\!E_T$must be greater than 20 GeV. The requirement on missing transverse energy reduces the amount of possible contamination from QCD events.

Figure 5.1 shows the distribution of the missing transverse energy in events in which the muons have been required to fail the isolation requirements*. Included in

*Requiring the muon to fail the isolation requirements effectively requires the muon to have been associated with jet activity in the event. This ensures that while the muon will have the same kinematic properties and trigger biases, it is not associated with a W production event.

the figure is the event normalized Monte Carlo missing transverse energy spectrum. A cut on missing E_T of 20 GeV effectively saves the majority of the signal, while cutting away the background.

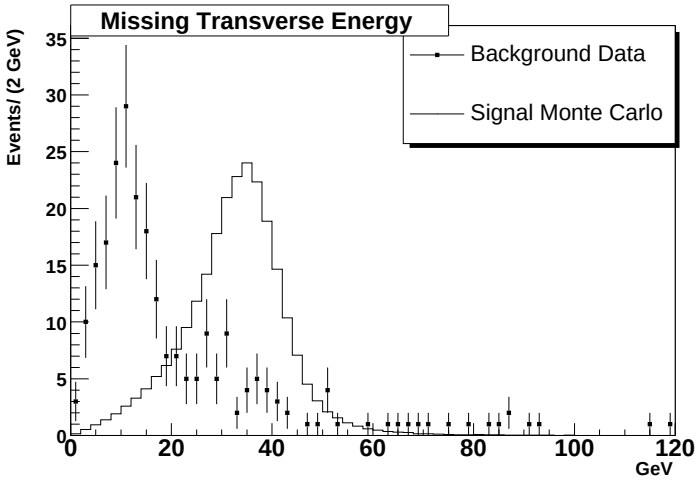

Figure 5.1 Missing E_T for Background data and Signal Monte Carlo.

The muon and photon candidates are required to be well separated. This is necessary for two reasons. The first is that if a separation requirement is not imposed, the full cross-section (including photons radiated directly from the muon) will diverge. The second is that events in which the photon is radiated from the lepton line do not probe the coupling of the W to the photon. Therefore, the separation cut helps to minimize the contribution from these radiative decays. This cut is partially redundant because of the track isolation requirement on the photon, and the isolation of the muon. If the central track associated with the muon is within 0.4 in ΔR of the photon,

then the photon will fail its track isolation requirement. Likewise, unless the muon is at least 0.6 in ΔR from the photon, the outer annulus of the muon's calorimeter isolation cone will intersect the 0.2 cone that contains most of the photon energy, and cause the muon to fail it's isolation requirement. The separation cut of 0.7 is chosen both because of the above reasons, and because the additional separation removes a great deal of radiative decays. Figure 5.2 shows the distribution of $\Delta R(\mu - \gamma)$, for unsmeared Monte Carlo events that at the generator level were required to be separated by 0.4. At the generator level, if the three body transverse mass is required to be greater than 90 GeV, the radiative part of the cross section is effectively turned off. Thus by plotting the separation for events that were below 90 GeV and for those above 90 GeV, the number of events from radiative decays may be estimated, as can the effect of the separation cut on production decays. Setting ΔR >0.7 leaves 66% of the radiative Wγ events, while saving 98% of the production decays.

For the anomalous coupling limits and the radiation amplitude zero (but not the cross section), a cut on the three body mass of the system is made, to further minimize the contribution from final state radiation. The three body mass of the muon-photon-$\not\!\!E_T$system is defined in Equation 2.12. This is the equivalent of requiring the minimum invariant mass of the system be greater than 90 GeV, well in excess of the W mass. Radiative decays should peak strongly at 80 GeV, since they originate from a W decay with photon radiated off of the final state lepton.

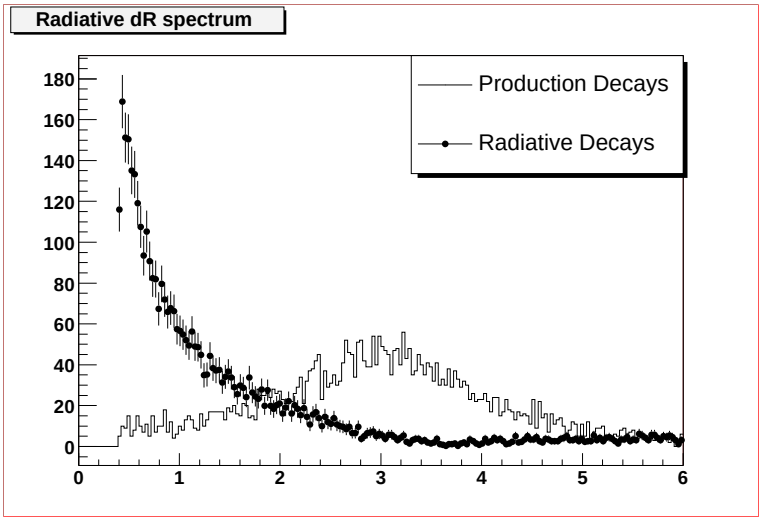

Figure 5.2 ΔR for Production and Radiative Decays.

5.4 Selected Candidates

The total number of selected candidates in each trigger range is given in Table 5.1. The combined candidate plots for muon p_T, $\not\!\!E_T$, photon E_T, transverse mass and three body transverse mass are shown in Figures 5.3, 5.4, 5.5, 5.6, and 5.7 respectively. The selected candidate plots with the three body mass cut of 90 GeV are shown in Figures 5.8, 5.9, 5.10, 5.11, and 5.12 respectively.

Trigger	Events	Events ($M_{T3} > 90$ GeV)	Luminosity (pb^{-1})
MU_W_L2M5_TRK10	23	11	30.4
MUW_W_L2M3_TRK10	73	33	59.3
MUW_A_L2M3_TRK10	65	28	44.8

Table 5.1 Number of Candidates in each trigger range, with integrated luminosity. M_{T3} is the three body transverse mass as defined in Equation 2.12.

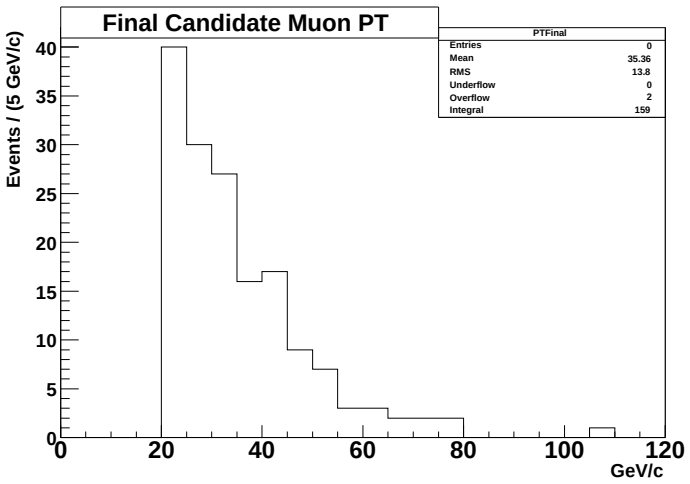

Figure 5.3 Muon p_T as measured by the central tracker for selected candidates.

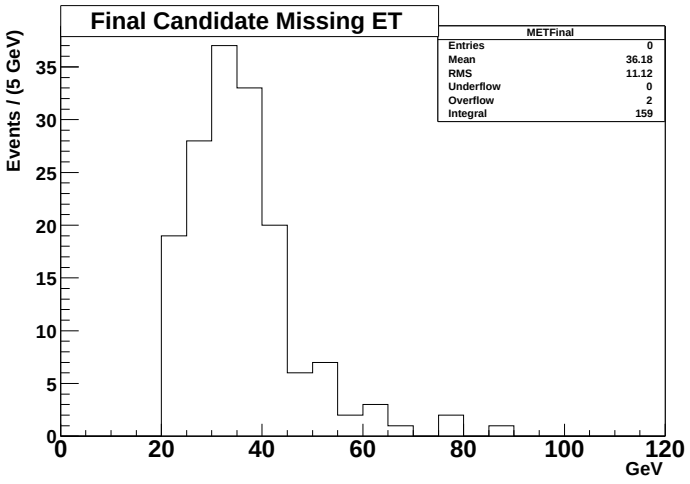

Figure 5.4 Missing E_T for selected candidates.

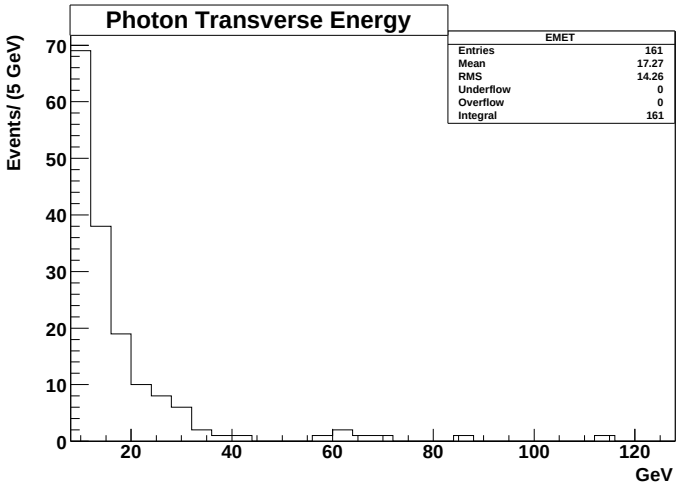

Figure 5.5 Photon E_T for selected candidates.

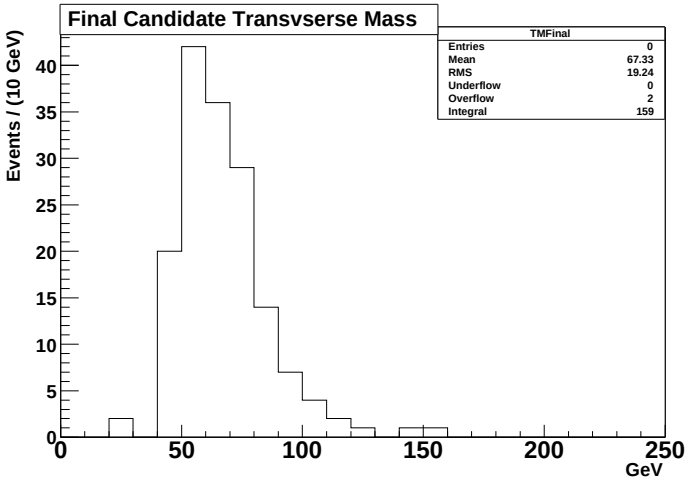

Figure 5.6 Transverse Mass (muon-$\not\!\!E_T$) for selected candidates.

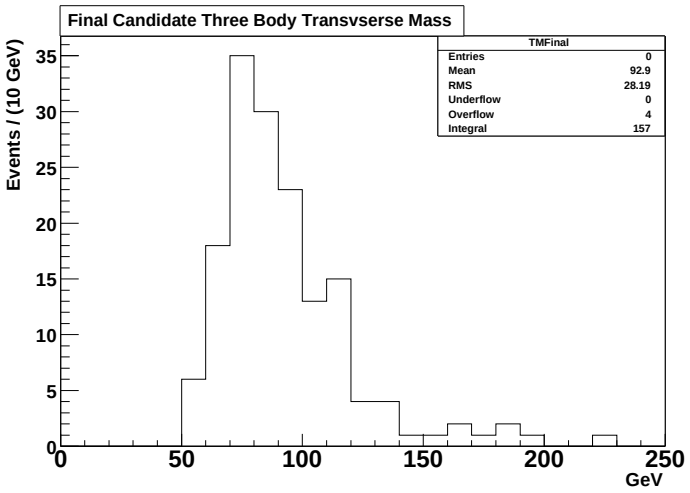

Figure 5.7 Three Body Transverse Mass for selected candidates.

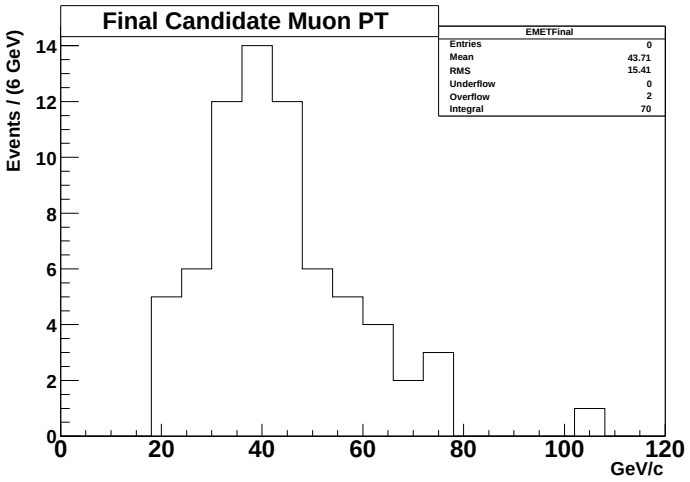

Figure 5.8 Muon p_T as measured by the central tracker for selected candidates, with three body mass cut.

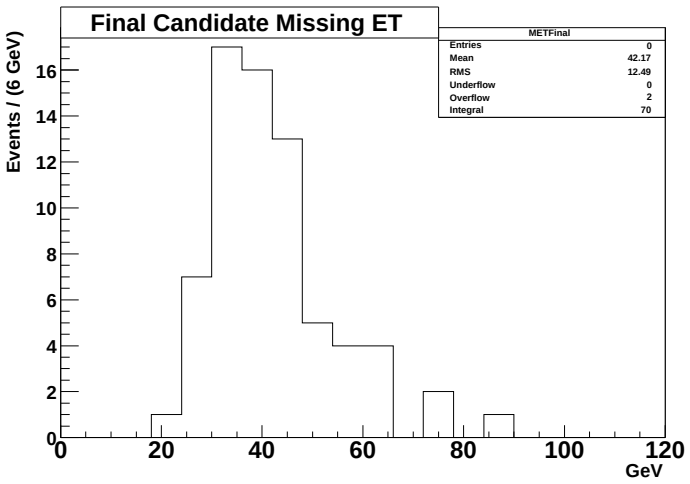

Figure 5.9 Missing E_T for selected candidates, with three body mass cut.

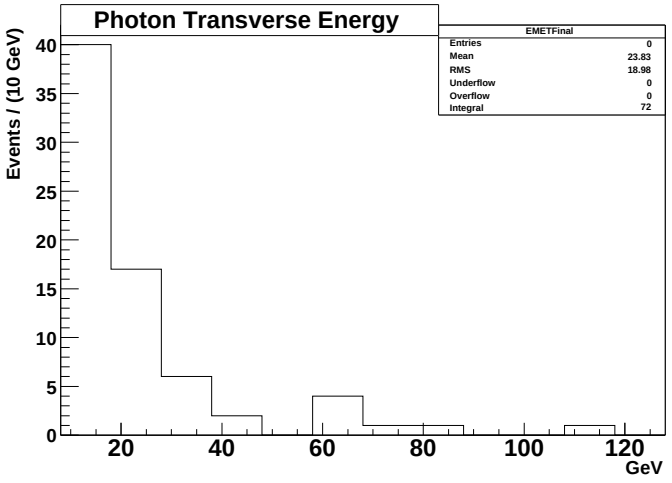

Figure 5.10 Photon E_T for selected candidates, with three body mass cut.

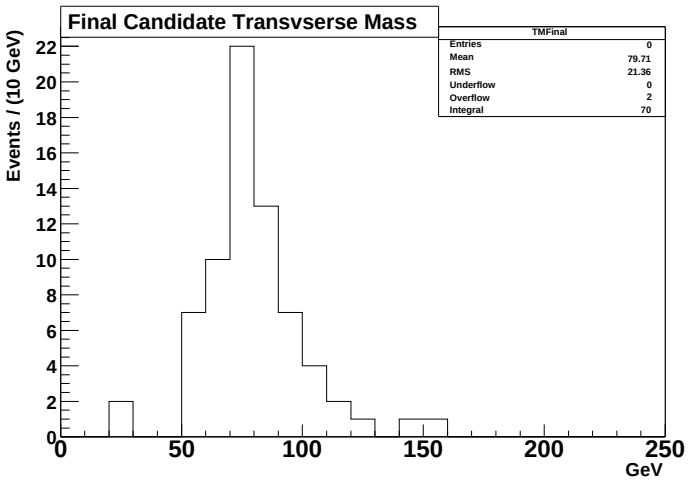

Figure 5.11 Transverse Mass (muon-$\not\!\!E_T$) for selected candidates, with three body mass cut.

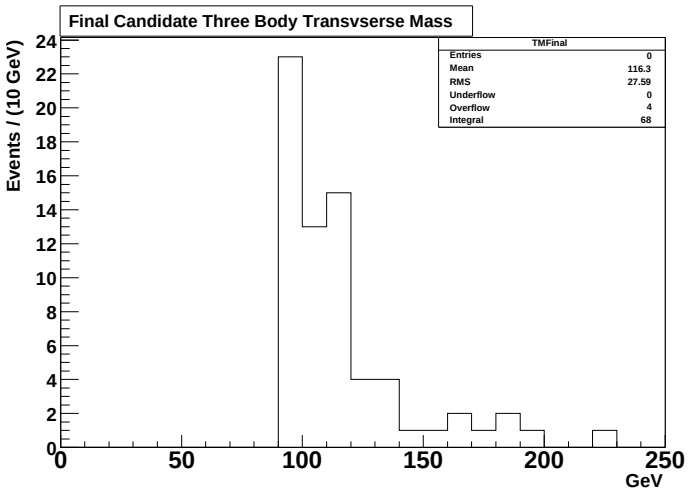

Figure 5.12 Three Body Transverse Mass for selected candidates, with three body mass cut.

Chapter 6
Efficiencies

In order to calculate the cross section for $W\gamma \rightarrow \mu\nu\gamma$, the efficiency of each of the selection cuts must be obtained. Many of the efficiencies are determined from independent sets of data. Others depend on the kinematics of $W\gamma$ production, thus it is necessary to appeal to the Monte Carlo. For both the cross section and the limits on anomalous couplings it is important to assess the effect of all selection cuts as a function of the transverse momentum of both muon and photon, and their $\eta - \phi$ locations.

For the total efficiency, for the cross section calculation, the efficiencies will be calculated by first assessing the efficiency for $W\gamma$ events to be produced in the DØ detector. The acceptance of the DØ detector for this analysis is the central calorimeter for the photon, and the entire volume of the muon system for the muon. The resolution and smearing effects for both the muon and the photon are taken into account in these efficiencies.

Then the reconstruction and efficiencies for the muon and the photon are applied. The trigger efficiency for the muon is then calculated with respect to the kinematics of the muon from the W decay only, and combined with the other efficiencies. Since the muon trigger depends only on the kinematics of the muon from the W decay, this

treatment should be sufficient. The efficiencies for reconstruction of the photon are estimated using Monte Carlo, and checked using the data.

6.1 Acceptance

The acceptance of the DØ detector for W$\gamma \rightarrow \mu\nu\gamma$ events may be roughly divided into two separate parts, geometric and kinematic. Geometric acceptance is defined to be the efficiency with which Wγ production events will fall within the detector (as defined below). Kinematic acceptance is the efficiency with which events from Wγ will be reconstructed with the proper kinematic properties, such as photon E_T and muon p_T. Kinematic acceptance also takes into account photons which were produced with lower E_T, but due to finite resolution effects were reconstructed with high enough E_T to pass the selection criteria. Since these efficiencies are correlated through the transverse momentum of the system, the acceptance for geometric and kinematic cuts are calculated together.

The geometric acceptance for Wγ events is defined as events in which both the muon and the photon are separated by ΔR > 0.7, and both lay within the acceptance of the detector in η. The acceptance for the muon is defined by the full coverage of the central fiber tracker (CFT detector $|\eta| < 1.62$). This is necessitated by the Level 3 track requirement in all versions of the trigger. In addition to this requirement, the muon is required to be in the muon system (muon system detector $|\eta| < 2.0$), and required not be in the area in the bottom of the central muon system where

instrumentation is sparse. If one calculates $|\eta_{detector}|$ for muons that pass through all sixteen layers of the CFT, the muon $|\eta_{detector}|$ is always within 2.0.

The acceptance for the photon is defined as the central calorimeter only (detector $|\eta| < 1.1$). This is the area of the best tracking efficiency, and thus the best photon reconstruction. The photon is required to not have been reconstructed inside the calorimeter module boundaries, so that the energy of the photon may be reconstructed with the best resolution.

The kinematic acceptance is the efficiency for which the muon (in the geometric acceptance) is reconstructed with a transverse momentum of greater than 20 GeV/c (using the momentum value from the central tracker), 20 GeV of missing transverse energy is reconstructed, and the photon is required to be reconstructed with a transverse energy of greater than 8 GeV.

$$A = \frac{N(\eta_{\mu_{CFT}} < 1.6; \eta_{\gamma_{CAL}} < 1.1; p_{T_{\mu S}} > 20GeV; E_{T_{\gamma S}} > 8GeV; \Delta R_{\mu\gamma S} > 0.7)}{N(E_{T_{\gamma G}} > 8GeV; \Delta R_{\mu\gamma G} > 0.7)} \quad (6.1)$$

The equation for the total acceptance (kinematic and geometric) is given in Equation 6.1. Here, $E_{T_{\gamma S}}$ is the smeared E_T of the photon, $\Delta R_{\mu\gamma S}$ is the smeared separation between the muon and photon, and $E_{T_{\gamma G}}$ and $\Delta R_{\mu\gamma G}$ are the generated quantities respectively. The term in the numerator is the number of events, within the detector acceptance, reconstructed with the proper kinematic values for muon transverse momentum, missing transverse energy, and photon transverse energy. The denominator is the total number of events generated with photon transverse energy greater than

8 GeV, and lepton-photon separation of 0.7 in ΔR.

2.6 million simulated Wγ events were generated using the Baur Monte Carlo [31]*, with the photon E_T threshold at 3 GeV (to properly account for energy smearing effects at 8 GeV), and with a separation in $\Delta R > 0.4$. The acceptance may be calculated by counting those events which pass the kinematic and geometric acceptance cuts, and dividing by the total events generated. However, several effects in the generation and smearing of this Monte Carlo must be accounted for. Since this is a leading order Monte Carlo, the Wγ system is produced with no initial state gluon radiation that would provide a boost, possibly changing the acceptance for events. A boost was added to the system to simulate this effect (see Section 6.1.2). Differences in the parton distribution functions used in the generation may yield a difference in the distributions as well. This is assessed using several different PDF sets to determine if the choice of a single one introduces a bias. The distribution of the z vertex in the three different trigger ranges is slightly different, and thus systematic effects in the distribution in z must be taken into account. This may be taken into account by examining the distributions from the data. The parametrized Monte Carlo simulation is used to simulate the resolution of the detector for the kinematic efficiencies for the muon and photon resolutions. The uncertainty in the parameters used in the

*At the present time, the full interference structure of $W\gamma$ is not handled properly in the version of Pythia used at DØ. Therefore the same generator that was used in Run I to properly generate these events is used for this analysis.

simulation must be assessed as well.

6.1.1 Z Vertex Distribution

The z vertex distribution for each of the single muon triggers is slightly different due to different trigger requirements. This difference is especially visible in the earliest trigger, MU_W_L2M5_TRK10, where the luminosity counters were required to reconstruct a fast z position in the detector, which more tightly constrains the distribution.

Using a sample of inclusive high p_T single muon events from the same dataset as the signal and background, the three different vertex distributions may be plotted. Each was fit with a Gaussian, and then the fit parameters were used in the Monte Carlo (fits are shown in Figures 6.1, 6.2 and 6.3). The acceptance for each of these distributions is given in Table 6.1. Since the difference in acceptance is very small as a function of the change in the vertex distribution, the parameters for the highest integrated luminosity trigger, MUW_W_L2M3_TRK10 will be used for the remainder of the acceptance studies. The largest difference between these acceptances will be taken as a systematic error.

Vertex Dist.	Acceptance	MC Stat. Err
MU_W_L2M5_TRK10	0.102895	0.000316
MUW_W_L2M3_TRK10	0.102526	0.000315
MUW_A_L2M3_TRK10	0.102579	0.000316

Table 6.1 Summary of Acceptance, with Variation of Z Vertex Distribution. Each set represents 2.6M Monte Carlo events produced with the Baur Monte Carlo (using CTEQ5L), and then boosted using Pythia QCD ISR (using CTEQ5L).

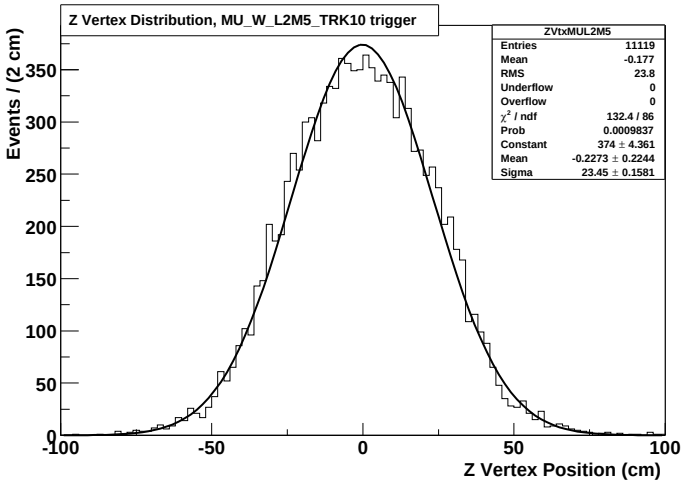

Figure 6.1 Vertex Distribution and Fit for MU_W_L2M5_TRK10 from data.

6.1.2 Next to Leading Order Effects

The Baur Monte Carlo program calculates the cross section for Wγ production using a k-factor to take into account next-to-leading order effects *. The k-factor is a constant which is used to scale the cross section up to account for the increase

*The next-to-leading order effects mentioned here are from QCD. Initial state gluon radiation off of the incoming quarks can provide the final Wγ system with an non-negligible p_T boost, which can change the final observed kinematics.

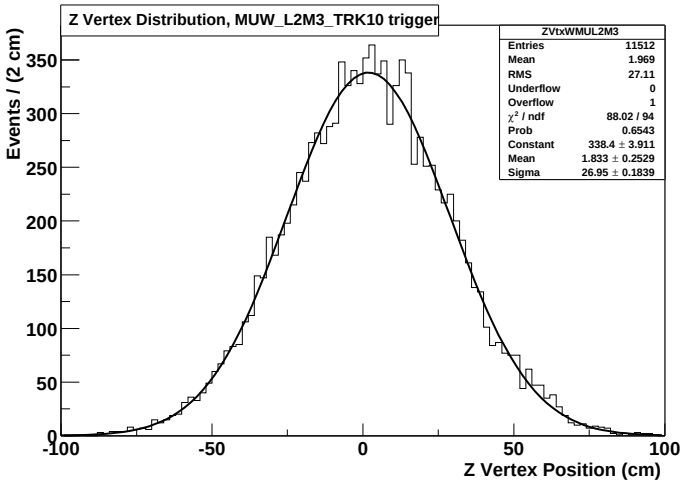

Figure 6.2 Vertex Distribution and Fit for MUW_W_L2M3_TRK10 from data.

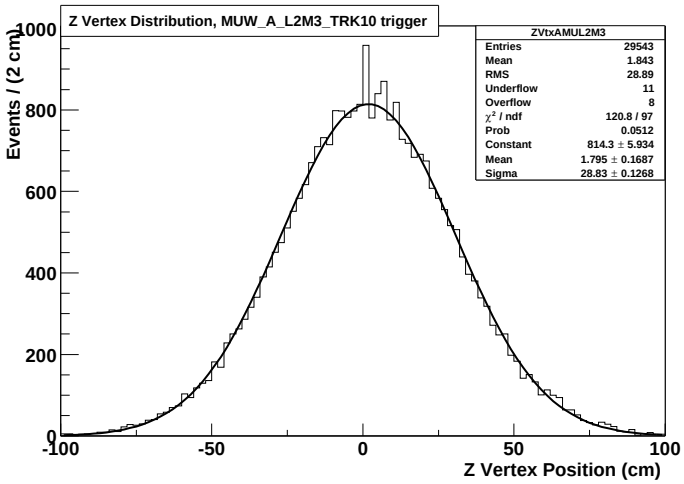

Figure 6.3 Vertex Distribution and Fit for MUW_A_L2M3_TRK10 from data.

due to QCD effects. This allows the proper calculation of the cross section, but does not replicate the boost given to the system p_T due to this radiation. Therefore the

four vectors produced by the generator are produced with no initial system p_T. In order to simulate these next to leading order effects, Wγ events from Pythia were produced with initial state radiation enabled. The actual cross section and lepton-photon kinematic properties of these events is incorrect, but the important part taken from Pythia was the initial p_T boost of the system.

The p_T spectrum (shown in Figure 6.4 for CTEQ5L) is then applied to the four vectors produced by the Baur generator. Each of the final state four vectors is Lorentz boosted in an arbitrary direction in ϕ with the magnitude from the initial state radiation. The difference in acceptance between applying this initial state radiation from Pythia, and simply using the Baur generated four vectors is summarized in Table 6.2. The system transverse momentum was generated using CTEQ5L PDF, and cross checked against a different set (CTEQ3M).

Boost	Acceptance	MC Stat Error
None	0.102649	0.000318
CTEQ5L	0.102526	0.000315
CTEQ3M	0.102631	0.000315

Table 6.2 Summary of Difference Between Leading Order Acceptance and Acceptance with Pythia Boost. Each set was generated using the Baur Monte Carlo (using CTEQ5L PDF), and then the specified boost was applied.

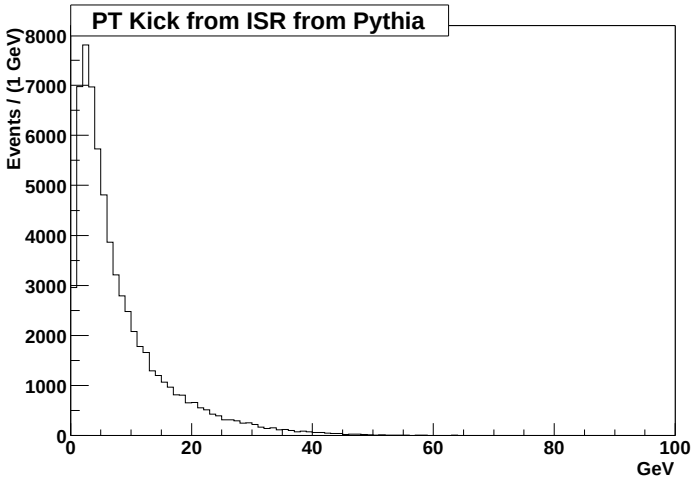

Figure 6.4 Initial System p_T from Initial State Radiation (CTEQ5L).

6.1.3 Parton Distribution Functions

In order to assess the dependence of the acceptance on the parton distribution functions that were used in the generation of the Monte Carlo, several sets of events were generated using different PDF sets. Three different sets were used, CTEQ5L, GRV98, and MRSR2. The average will be the used in the final calculation, and the difference assigned as a systematic. The system was boosted according to the distribution acquired in Section 6.1.2, using the CTEQ5L boost. The results from this variation are summarized in Table 6.3.

6.1.4 Resolution Effects

The resolution of the detector is parametrized from the data. The calorimeter and tracker both have resolution functions which are functions of the E_T and p_T of the

PDF	Acceptance	MC Stat Error
CTEQ5L	0.102526	0.000314
GRVLO98	0.101436	0.000313
MRSR2	0.106020	0.000319

Table 6.3 Summary of Acceptance Calculation Using Different Parton Distribution Functions. Each set of Monte Carlo consists of 2.6M events generated using the Baur Monte Carlo and uses the CTEQ5L boost to simulate NLO QCD effects.

measurement respectively. Since these parameters are determined from data each has an associated uncertainty which contributes to the uncertainty in the acceptance. To gauge the effect of these uncertainties, each parameter in the simulation is varied by one sigma from its central value and the acceptance recalculated. The uncertainty on the acceptance due to the parameters in the simulation is taken to be the maximum difference between this variation and the central value.

Calorimeter Smearing

The energy from the parametrization for the calorimeter is given by:

$$E_{smeared} = E^{'} + x * \sigma_E, \tag{6.2}$$

where

$$E^{'} = A + B \times E_{generated}, \tag{6.3}$$

and

$$(\frac{\sigma_E}{E})^2 = C^2 + \frac{S^2}{E} + \frac{N^2}{E^2}. \tag{6.4}$$

The first term in Equation 6.2 (E') is due to the uncertainty in the energy scale. This is taken to be an offset (A), plus a scale factor (B), as shown in Equation 6.3. The second term is due to the energy resolution (σ_E), which is shown in Equation 6.4, multiplied by a Gaussian distributed random number (x).

In Equation 6.4, C represents calibration errors (the amount to which any given energy measurement is wrong due to pedestals, gains, non-linearity etc.). S represents the sampling fluctuations, the error due to the amount of shower sampled. N represents the 'noise', mainly due to the natural radioactivity of the uranium which contributes energy to the calorimeter. From Z→ee events the constant term (C) in the central is determined to be (4.20 ± 0.30)%. This ends up being the dominant term in the resolution. The sampling term (S) is taken to be the same as from Run I which was determined to be 0.15 $\text{GeV}^{\frac{1}{2}}$. Compared to both of the previous terms, the noise term (N) is small. Since this (like the sampling term) is expected to be the same as from Run I (since the physical construction of the calorimeter has not changed), this term is set to its Run I value of 0.29 GeV. The scale factor (B, in Equation 6.3 was determined to be 1.0054 ± 0.0020. The offset (A) was determined to be 0.038 ± 0.048 [32].

The position resolution of the calorimeter and muon combine to form the resolution of the separation cut. However, the position resolution of the calorimeter will dominate the measurement of ΔR (due to the coarseness of the segmentation as

compared to the tracker), thus the error on the acceptance due to this uncertainty appears mainly in the variation of the calorimeter resolution for η and ϕ. The position resolution in η is measured to be 0.015 ± 0.004, and is Gaussian distributed.

The calorimeter ϕ position however is found to be more complex in the areas near where the module boundaries are removed. Since some energy is lost within the boundary, the cluster position in ϕ is 'pulled' away from the boundary. Instead of parametrizing this behavior, the distribution of the difference in ϕ from the measured track position in Z→ee events was put into the parametrized Monte Carlo so that the effect on the acceptance could be properly gauged. The error on this smearing is assessed by varying the module boundary cut by the RMS (root-mean-square) of the $\Delta\phi$(Calorimeter-Track), measured to be (0.0072 in ϕ or 0.036 in ϕ module space). This uncertainty dominates the error on the acceptance.

Parameter	$+1\sigma$ (%)	-1σ (%)
Offset	+0.724	-0.715
Scale	+0.334	-0.276
Constant	-0.0146	+0.00975
σ_η	+0.104	+0.0283
σ_ϕ	-4.93	+5.96

Table 6.4 Change in Acceptance Due to variation of Calorimeter Parameters

Tracker Smearing

The measurement of the transverse momentum from the central tracker for high p_T tracks has been found from Z$\rightarrow \mu\mu$ events and parametrized in the simulation [33]. The resolution of the central tracker is parametrized as:

$$\frac{1}{p_T^{smeared}} = A \times (\frac{1}{p_T^{generated}} + x * \sigma_{p_T}), \tag{6.5}$$

where A is the momentum scale, and σ_p is given by:

$$\sigma(\frac{1}{p_T}) = \frac{\sqrt{(S^2 cosh(\eta) + (Cp_T)^2)}}{p_T}. \tag{6.6}$$

In Equation 6.6 the S term represents the multiple scattering through the material of the detector, which increases with the path length through the material, and C represents the finite position resolution of the detector . These parameters were found to be S=0.002670±0.00020 and C=0.02580±0.0008 respectively.

Parameter	$+1\sigma$ (%)	-1σ (%)
Scattering (S)	-0.0624	+0.106
Resolution (C)	+0.0166	-0.0283
Scale	+0.335	-0.292

Table 6.5 Change in Acceptance Due to variation of Tracker Parameters

The missing transverse energy cut is dominated by the momentum resolution of the muon (and simulation of underlying event), and is thus assessed with the kinematic requirements on the muon.

Local Muon Smearing

The momentum resolution for the muon system has been parametrized using dimuon events over a large range of p_T, and entered into the simulation [35]. The resolution is parametrized as:

$$\frac{\sigma(p)}{p} = \frac{\alpha \times (p - \beta)}{p} \oplus \gamma p. \tag{6.7}$$

In this expression, α represents the contribution from multiple scattering, β is represents the energy loss in the material prior to the muon system, and γ is the contribution due to the finite position resolution of the muon chambers. Since the tracking systems for forward and central muon are different, they are parametrized separately. Table 6.6 summarizes the different parameters for forward and central local muon resolution. The change in acceptance from the variation of these parameters is summarized in Table 6.7.

Parameter	Value	Fit Error
α_C	0.3621	0.0376
β_C	3.089 (GeV)	0.2048
γ_C	0.0314	0.00297
α_F	0.2108	0.0101
β_F	1.785 (GeV)	0.1557
γ_F	0.00575	0.00048

Table 6.6 Summary of Local Muon Smearing Parameters

Parameter	$+1\sigma$ (%)	-1σ (%)
α_C	-0.0390	+0.0497
β_C	+0.00682	-0.000975
γ_C	-0.432	+0.381
α_F	-0.00195	≈ 0
β_F	≈ 0	-0.00195
γ_F	≈ 0	+0.00195

Table 6.7 Change in Acceptance Due to variation of Muon System Smearing Parameters.

6.1.5 Acceptance Values

The final value of the acceptance is found to be 0.1033 ± 0.0068 (sys). The final values for the systematic uncertainties are summarized in Table 6.8. From the distribution given by these Monte Carlo events, the efficiencies measured from data will be applied to get efficiencies corresponding to the physics distribution of $W\gamma \rightarrow \mu\nu\gamma$ events.

Parameter	Error (%)
Z Vertex	0.360
NLO Boost	0.120
PDF Variation	2.61
Calorimeter Smearing	6.02
Tracker Smearing	0.352
Local Muon Smearing	0.435

Table 6.8 Summary of Acceptance Uncertainty.

6.2 Muon Efficiencies

Many of the appropriate muon efficiencies may be obtained by using Z$\rightarrow \mu\mu$ events from data. The single muon trigger that is required for the selection of the candidate events may be used to select these events. Then one of the muons matched up to the trigger information. The other muon from the Z decay should then be unbiased by the trigger requirements and can yield the efficiencies of interest.

In each case, once the appropriate efficiency from the data has been measured, the Monte Carlo muon distribution may be used to fold in the actual distribution of muons so that the efficiency for muons from Wγ may be determined.

6.2.1 Reconstruction Efficiency

The reconstruction efficiency is composed of two different factors, which are handled together for the purposes of this measurement. First there is a contribution from the efficiency with which the offline software will reconstruct a muon of the appropriate quality in the detector. Second, there is the efficiency for which a muon of a given $\eta_{detector}$ will meet the offline requirements for the number of hits in the different layers.

The reconstruction efficiency can be directly obtained from the data, by using Z events in which one muon is matched up to the appropriate trigger information, and the other is found in the tracking volume. From the tracking quantities alone, the invariant mass of the Z may be reconstructed, and the background subtracted [34].

Note that the background subtraction in most cases consists of Drell-Yan muons that also should have had tracks associated with them. The subtraction is only necessary at all because of a small percentage of contamination from $b\overline{b}$ production.

It is necessary to find the efficiency for reconstructing not only the required muon quality for the selection, but also for the veto. The efficiency of the veto in the selection cuts for rejecting Zγ background is dependent on both the tracking efficiency and the reconstruction efficiency.

The efficiency as a function of muon detector η is shown in Figure 6.5 *. For the efficiency of reconstruction for the cross section, the distribution of the muons from Wγ events in the Monte Carlo is folded with the efficiency distribution from data to give an efficiency for a muon from a Wγ event to be reconstructed. Also, the efficiency for matching a track to a muon found in the muon system is implicitly included here. This efficiency (though close to one) will be eliminated from the study of the tracking efficiency so that it is only counted once. The average efficiency for reconstructing a medium muon from a Wγ event is estimated to be 0.847 ± 0.010.

6.2.2 Tracking Efficiency

Z$\rightarrow \mu\mu$ events can be used to measure of the tracking efficiency. As before, one muon is required to be reconstructed both in the muon system and in the tracker, and be associated with the trigger information. Unlike in the reconstruction efficiency,

*Since the reconstruction efficiency is largely a function of the geometry of the muon system, the dependency is plotted as a function of detector η.

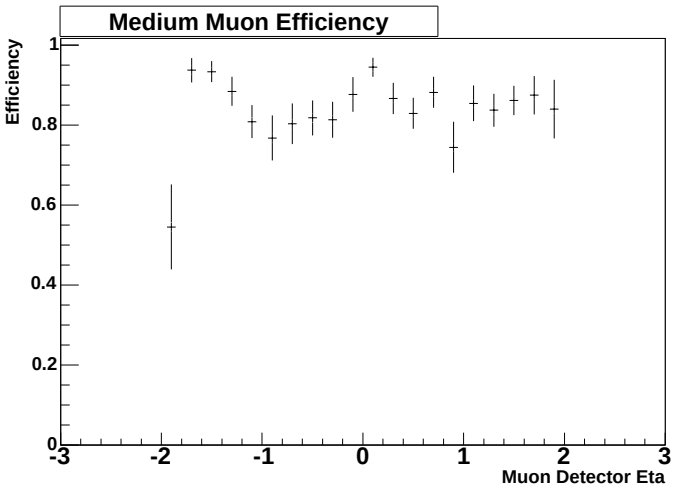

Figure 6.5 Medium Muon Reconstruction Efficiency as a function of muon detector η.

the second muon is required to be reconstructed in the muon system, with a high transverse momentum as given by the toroid. The invariant mass (though poor in resolution), can be reconstructed from the track and toroid momenta. Then the number of true Z$\rightarrow \mu\mu$ events may be reconstructed and the efficiency calculated.

Like the reconstruction efficiency, the tracking efficiency is also used to find the rejection of Zγ events. If an additional stiff track is reconstructed, it could be a sign of this background. Thus the efficiency for reconstructing the track from a Z is needed, not the efficiency multiplied by the matching efficiency (which for the purposes of the cross section is already included in the reconstruction efficiency). This effect was checked for by allowing for a 'matched' track greater than 15 GeV in a cone of dR$<$ 0.5 about the test muon. This effect is observed to be small (less than 1%).

The tracking efficiency is found to be not a function of $\eta_{detector}$, but rather of the physics η of the track*. This can be understood by visualizing the path length of the charged particle through the central fiber tracker. At small η, meaning a track almost perpendicular to the beam direction, the path length through the scintillating fiber will be the smallest, and thus the light yield will also be small. Conversely, the light yield is the highest when the path length of the particle is the highest, meaning at high physics η. Thus the tracking efficiency is parametrized in physics η and five bins of z vertex position (z< -30cm, -30cm < z < -10cm, -10cm < z < 10cm, 10cm < z < 30cm, and z > 30cm). The center bin (-10cm < z < 10cm) is shown in Figure 6.6. Binning in physics η and z position, and then folding the distribution with the Wγ Monte Carlo sample, the average efficiency is found to be 0.983 $\pm$ 0.010 (sys). The systematic error here originates from the statistical errors in the Z$\rightarrow \mu\mu$ sample.

6.2.3 Trigger Efficiency

The trigger efficiency is calculated by two different methods. First, by selecting events in which an independent calorimeter trigger fired, and a single 20 GeV/c muon (as measured by the central tracker) was reconstructed, the trigger bits may be examined to see if the appropriate trigger fired. These events are effectively muon plus jet events, and thus to maintain a large enough sample of events, the isolation criteria is not applied to the reconstructed muon.

*Each track that has z-information (meaning not axial only tracks from CFT), has its own physics η from the angle the track makes with respect to the z-axis.

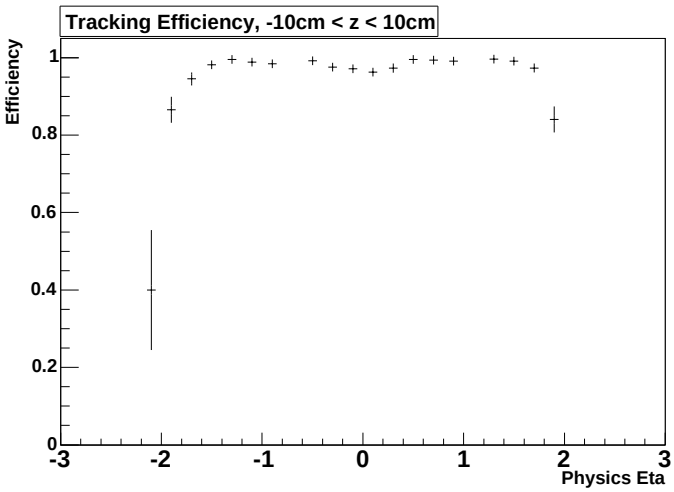

Figure 6.6 Tracking efficiency as a function of physics η with z vertex, -10cm < z < 10cm.

Second, Z→ $\mu\mu$ events may be used. In events selected on a single muon trigger where one muon is matched up to the Level 1 information, the readout may be matched to the second as well. This has lower statistics, and is limited to the period of data in which the Level 1 Muon readout is available*. This limits the statistical power of the sample, and thus the data from Z→ $\mu\mu$ events is used in trigger studies as a cross check, where available.

The trigger efficiency may be divided up into its component parts. First, the efficiency for the Level 1 trigger to fire is measured, with respect to an offline medium muon matched to a central track of 20 GeV/c of momentum. Then the efficiency of the Level 2 requirement is measured with respect to the same kind of muon, which

*The amount of data without Level 1 Muon readout corresponds to approximately half of the MU_W_L2M5_TRK10 luminosity, or 15 pb^{-1}.

fired the Level 1 muon trigger. Finally the efficiency for Level 3 to reconstruct a central track of greater than 10 GeV/c is measured with respect to all of the preceding conditions (offline muon, Level 1 and Level 2).

The Level 1 and Level 2 trigger efficiencies are broken down into the three separate ranges of data individually, since the Level 1 requirements were different for each. Due to changes in the look-up tables at Level 2, the efficiencies for each of the separate periods of data taking are expected to be different, and are also measured separately. The Level 3 track efficiency was measured separately in the three different periods of data taking, but found not to be significantly different, and thus the Level 3 trigger efficiency is averaged over the entire range of data taking [36]. The different triggers (as described in Section 5.1.1) and the total amount of integrated luminosity for each are summarized in Table 6.9.

Trigger	Luminosity (pb^{-1})
MU_W_L2M5_TRK10	30.4
MUW_W_L2M3_TRK10	59.3
MUW_A_L2M3_TRK10	44.8

Table 6.9 Integrated Luminosity by Trigger. Each luminosity measurement has a 6.5% error associated with it.

Level 1

At Level 1, the three separate triggers differ the most. The earliest data required only a scintillator coincidence for the trigger to fire (and a fast-z signal from the

luminosity counters). In the later two periods of data, the requirement of the fast-z was removed, but wire confirmation was required. Also, when available, the all region trigger was used ($|\eta_\mu| < 2.0$, as opposed to $|\eta_\mu| < 1.6$, since muons at the far ends of the vertex distribution could pass through all layers of the fiber tracker as required, but hit the muon system at higher detector η than the wide region muon trigger. Also, the wide region trigger logic was found not to completely cover the full acceptance of the CFT, and thus some efficiency could be regained by using the all region trigger.

The efficiencies for the Level 1 trigger requirements are shown in Figures 6.7, 6.8, and 6.9 respectively. These were obtained using unbiased triggers, but agree

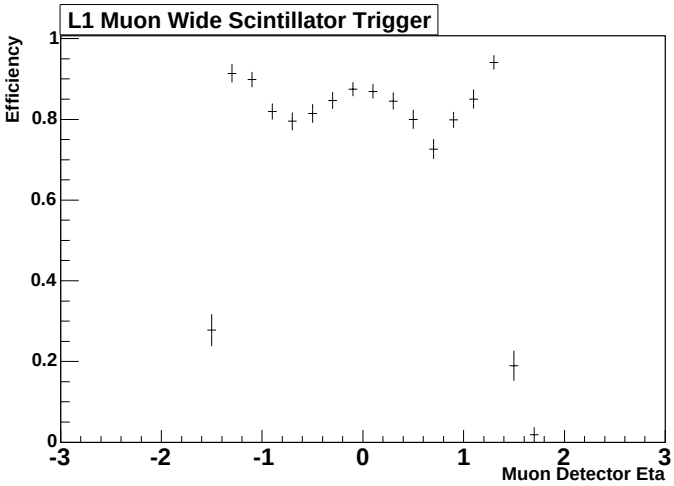

Figure 6.7 Efficiency for Level 1 Wide Scintillator Trigger (MU_W_L2M5_TRK10).

well with the efficiencies obtained from Z$\rightarrow \mu\mu$. Folding these distributions with the Monte Carlo gives the efficiencies listed in Table 6.10.

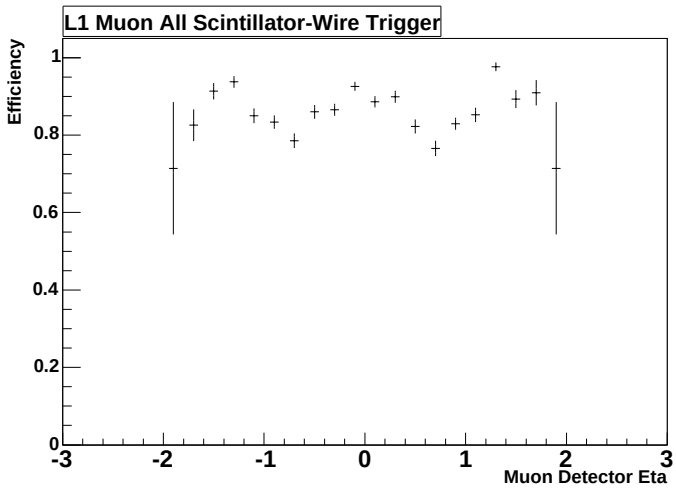

Figure 6.8 Efficiency for Level 1 All Wire and Scintillator Trigger (MUW_A_L2M3_TRK10).

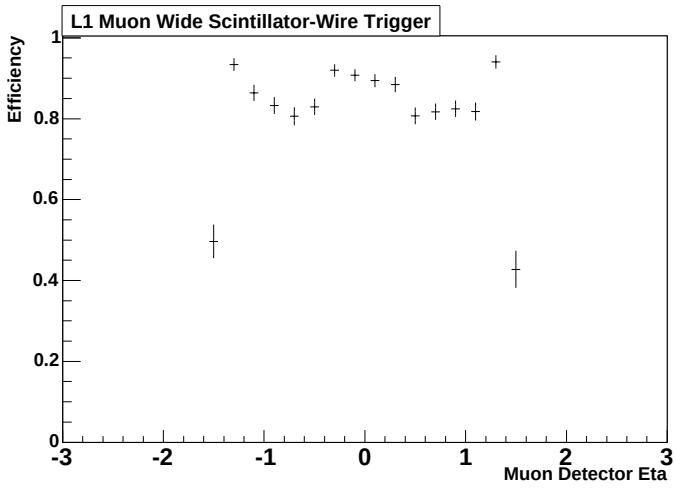

Figure 6.9 Efficiency for Level 1 Wide Wire and Scintillator Trigger (MUW_A_L2M3_TRK10).

Trigger	L1 Efficiency	MC Stat Error	Data Error
MU_W_L2M5_TRK10	0.774	0.001	0.007
MUW_W_L2M3_TRK10	0.810	0.001	0.005
MUW_A_L2M3_TRK10	0.864	0.001	0.004

Table 6.10 Level 1 Efficiencies, data measured efficiencies folded with Wγ Monte Carlo.

Level 2

The earliest data required a Level 2 medium muon with a toroid $p_T > 5$ GeV/c. This was found to have lower efficiency than expected due to inaccuracies in the muon p_T look-up tables. In later data taking, the requirement was relaxed to 3 GeV/c, and the look-up tables were updated to more accurately represent the resolution of the detector. The efficiencies for each of the Level 2 triggers are shown in Figures 6.10,

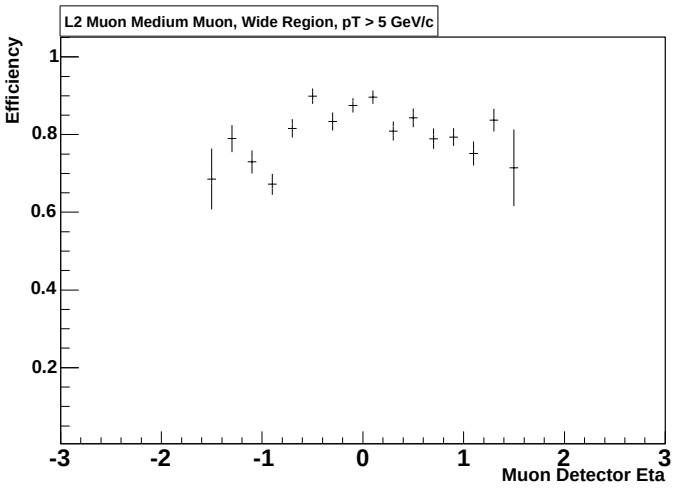

Figure 6.10 Efficiency for Level 2 Medium Muon (Wide Region), p_T >5 GeV/c (MU_W_L2M5_TRK10).

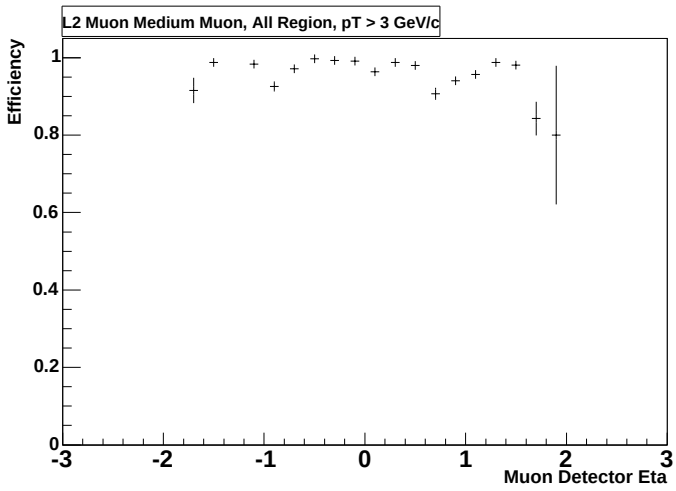

Figure 6.11 Efficiency for Level 2 Medium Muon (All region), $p_T > 3$ GeV/c (MUW_A_L2M3_TRK10).

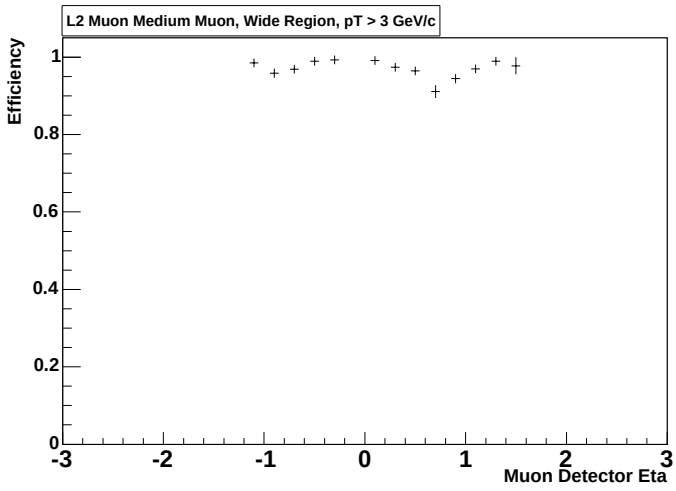

Figure 6.12 Efficiency for Level 2 Medium Muon (Wide region), $p_T > 3$ GeV/c (MUW_A_L2M3_TRK10).

6.11, and 6.12 respectively. The earliest condition is (as expected) the least efficient of the triggers, with the latter two close in their efficiencies. Folding these distributions with the Monte Carlo gives the efficiencies listed in Table 6.11.

Trigger	L2 Efficiency	MC Stat Error	Data Error
MU_W_L2M5_TRK10	0.812	0.002	0.007
MUW_W_L2M3_TRK10	0.976	0.001	0.002
MUW_A_L2M3_TRK10	0.971	0.001	0.002

Table 6.11 Level 2 Efficiencies, data measured efficiencies folded with Wγ Monte Carlo.

Level 3

The TRK10 requirement at Level 3 requires that a track of greater than 10 GeV/c be reconstructed. As discussed in Section 5.1.1, the track filter begins at the outermost layers of the CFT. Instead of being measured from the calorimeter triggered data, Z$\rightarrow \mu\mu$ data was used [33]. Since the muons in the calorimeter triggered sample are in general in association with a jet, there were more tracks as well. The Z sample was used since it more accurately represents the efficiency for an isolated track at Level 3. The efficiency for the Level 3 track filter is shown in Figure 6.13. Folding these distributions with the Monte Carlo distribution gives an efficiency of 0.966 $\pm$ 0.010 (sys).

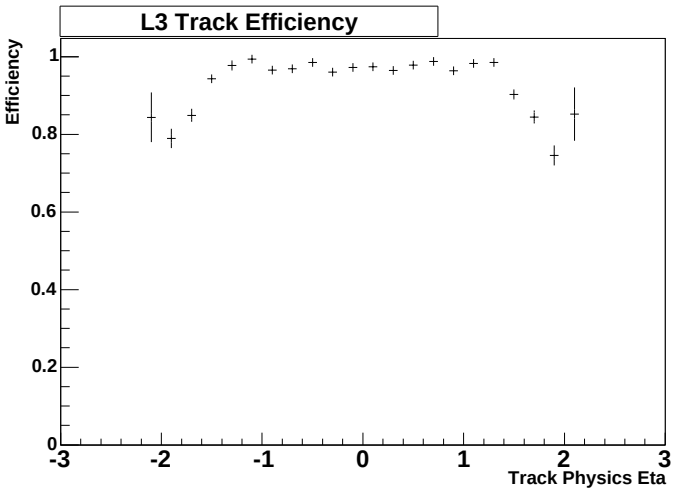

Figure 6.13 Efficiency for Level 3 Track p_T >10 GeV/c to be found with respect to an offline track with p_T >20 GeV/c.

6.2.4 Isolation Efficiency

Since the muon trigger has no isolation requirement, the full sample of Z events reconstructed offline may be used to estimate the efficiency of the offline isolation requirement, since muons from Z events should all be effectively reconstructed as isolated. Three cases can be used to calculate the efficiency for the isolation requirement:

- N_2: Both muons are isolated.
- N_1: One and only one muon is isolated.
- N_0: Neither muon is isolated.

Then the efficiency can be calculated with Equation 6.8.

$$\epsilon_{ISO} = \frac{2 \times N_2 + N_1}{2 \times (N_2 + N_1 + N_0)}. \tag{6.8}$$

By counting the exclusive number of N_2, N_1 and N_0 events, the efficiency can be calculated. Since the background in the sample of Z events is larger for those events in which one or more of the muons is non-isolated, for each case the invariant mass is formed (using the matched central tracks), and the resonance fit with a Gaussian plus an exponential (representing the background). Subtracting the exponential gives an estimate of the number of Z events in the sample for each type (see Figure 6.14). The isolation efficiency is found to be 0.905 ± 0.009 (stat). However, due to the low statistics in the case where both muons were reconstructed as non-isolated, and the uncertainty in the fit, this value was cross checked using only the events in which there were two isolated muons, and where only one was isolated. The efficiency found in this way was 0.920 ± 0.007, which is consistent within two sigma with the other value. The difference between these two efficiencies will be assessed as a systematic error.

Since the isolation requirement is made up of both the energy in the calorimeter and the sum p_T of tracks in the central tracker, there is a possibility that some η dependence is introduced from the geometry of these detectors. A separate approach, using one muon found as isolated, and matched to a central track, and the other where no isolation requirement is imposed, shows no obvious dependence has been

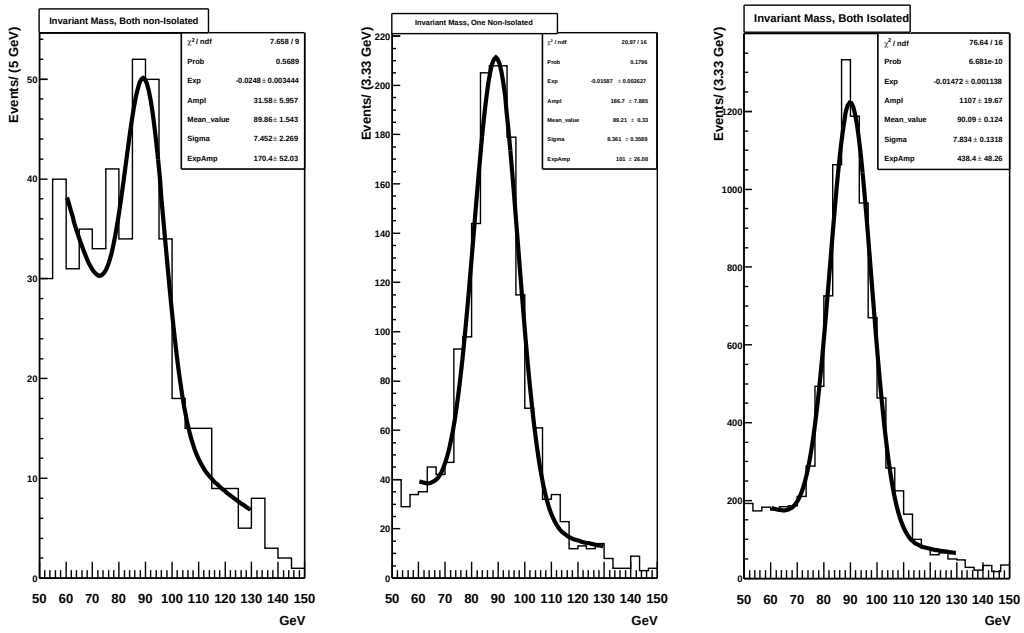

Figure 6.14 Invariant Mass in Z→ $\mu\mu$ events for isolation efficiency. The invariant mass was formed in the case where neither muon was isolated, where only one muon was isolated, and where both were isolated respectively.

introduced (see Figure 6.15).

6.2.5 Veto Efficiency

The efficiency associated with the veto on additional stiff tracks and additional muons originates from the possibility of jets in good Wγ events. These jets would arise from gluon radiation from the initial state partons, and could give rise to additional muons or high p_T tracks. To gauge this effect, a sample of Z→ee events is used. The initial state radiation in these events should be similar to that of other electroweak processes, and thus should have the same contribution from additional muons (or

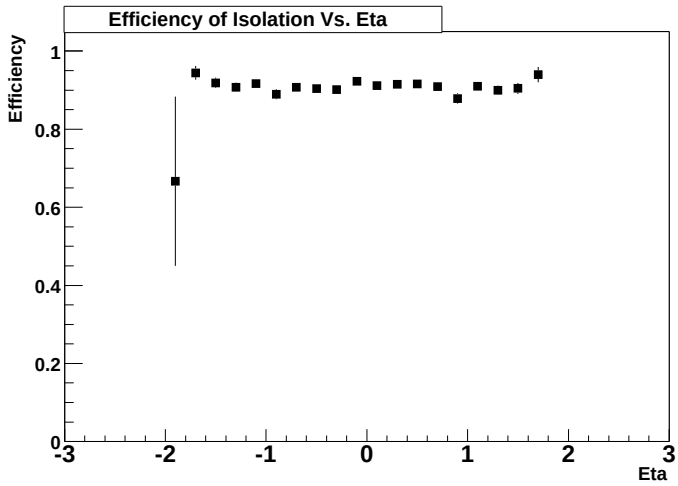

Figure 6.15 Efficiency of Isolation Requirement versus Eta. One muon was required to be isolated, and the other is used to determine the efficiency.

tracks).

The invariant mass for events in which additional muons or tracks were vetoed is formed, and the background subtracted. The same procedure was performed with events in which an additional muon or stiff track was found, so that the efficiency can be calculated (invariant mass is shown in Figure 6.16). Events were required to pass a trigger which required a single, high E_T electromagnetic object. Two electromagnetic objects must have been present, and each must have satisfied the following criteria:

- Electromagnetic Fraction > 0.9.
- Isolation < 0.15.
- HMatrix8 < 20.

- $E_T > 25$ GeV.

- Inside fiducial volume of calorimeter (within calorimeter detector $|\eta| < 1.1$ or $1.5 < |\eta| < 2.5$, and not within the module boundaries in the central region.

The veto efficiency is estimated to be 0.9438 ± 0.0032, where this statistical error is from the fit errors propagated through the calculation of the efficiency. To get an

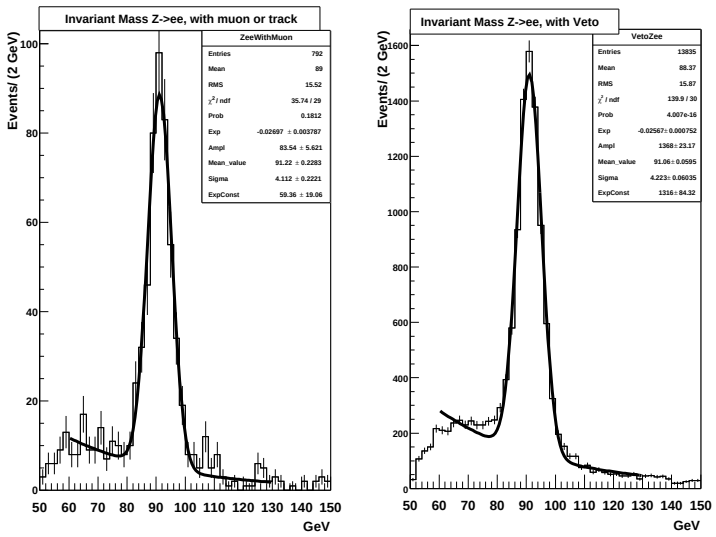

Figure 6.16 Z $\rightarrow$ *ee* Invariant Mass for the calculation of the Veto Efficiency. On the left is the invariant mass in Z events where one or more Loose muons were found. On the right is the invariant mass with the veto.

estimate of the systematic error on this efficiency, a track match was required on both EM objects, thus reducing the background. Then, without doing a fit, the number of events within the range 80-100 GeV was counted for each case (with veto satisfied and with the presence of a muon or track, see Figure 6.17) and the efficiency directly

calculated. This invariant mass range (centered about the Z mass), contains most of the reconstructed Z→ee events, as shown in Figure 6.17. The resultant efficiency was 0.9421 ± 0.0032, and thus the full difference between these two values is assessed as a systematic error on the efficiency of the veto.

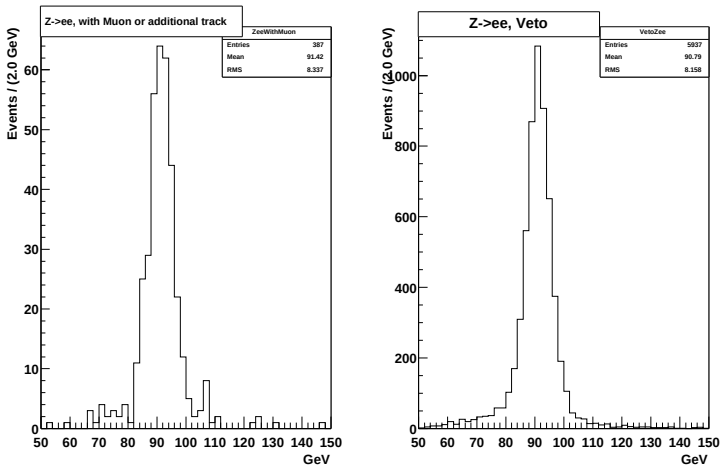

Figure 6.17 Z → *ee* Invariant Mass (with track match) for the calculation of the Veto Efficiency. On the left is the invariant mass in Z events where one or more Loose muons were found. On the right is the invariant mass with the veto.

6.3 Photon Efficiencies

The efficiency for reconstructing photons is more difficult to estimate than the efficiency for muons. Since there is no clean resonance in the data to yield a source of photons in the appropriate energy range, there are few options for gaining an understanding on photons directly from the data. Instead, by using the full GEANT Monte

Carlo simulation for the DØ detector, the photon efficiencies may be estimated*. Since it is known that the simulation does not completely describe the real detector, a scaling of the efficiencies from Monte Carlo must be performed†.

Z→ee events from data can be used to estimate the reconstruction efficiency for isolated electrons in the data. If then the simulation correctly handles the difference between electrons and photons, the efficiency for photons in the data may be estimated by scaling by the ratio of the electron efficiency in the data to the electron efficiency in the Monte Carlo. The systematic sources of error from this technique are the proper modeling of electrons in data, the difference between the electrons and photons in the Monte Carlo, and the E_T dependence of the cuts.

The cuts imposed on all electromagnetic objects by the simple cone algorithm (electromagnetic fraction, and then the tighter cut on isolation of 0.15) are found to be extremely efficient and thus the efficiency for these requirements is grouped together. A sample is identified in which one electromagnetic object is reconstructed and meets all the proper track and shower shape requirements (as in Section 6.2.5, with $E_T > 25$ GeV), and a second high p_T track is present. Thus the invariant mass for the Z may be reconstructed, without making any requirements on the calorimeter reconstruction of the second electromagnetic object. The efficiency for the reconstruc-

*This simulation of the DØ detector incorporates a full description of the material and efficiency of the real detector. No 'mixing' of parametrizations from the data is applied.

†The photon identification requirements for 'medium' energy photons, were effectively defined for the Wγ and Zγ analyses. [37] and [38] detail the studies performed to derive the efficiencies presented here.

tion of an electromagnetic cluster may then be determined (with proper background subtraction). The efficiency of the further cuts on shower shape and track isolation were likewise found, and the efficiency scaled accordingly. The Monte Carlo used for the electron efficiency was Z→ ee, and the photon Monte Carlo was based on a sample of diphoton events in the process qq→ $\gamma\gamma$, in several different momentum ranges. The efficiency found from these studies was parametrized as:

$$\epsilon_\gamma = (0.79 \pm 0.01) + (0.0032 \pm 0.0003) \times E_{T_\gamma} \tag{6.9}$$

At low E_T, there was a concern that the isolation requirement (iso < 0.15) would be less efficient, since at 8 GeV, this effectively required that there be less than 1.2 GeV between the inner cone of 0.2 in dR and the outer cone of 0.4 in dR. This efficiency was studied in J/$\psi \rightarrow ee$ events which were reconstructed with the simple cone algorithm. Since J/ψ events are in general produced in association with jets, an additional study of the noise in the calorimeter was performed by looking at the amount of energy deposited in the calorimeter in Z→ee events, in the area between the electrons where there should have been little activity. It was found ([38]) that the 'noise' energy deposition was not well modeled in the Monte Carlo. The efficiency was re-fit, taking this additional inefficiency into account:

$$\epsilon_\gamma = (A + B \times E_T) \times (1.0 - D \times e^{(E_{CLUS} \times E)}). \tag{6.10}$$

In this parametrization, the efficiency from Z→ee events in data, scaled by the differ-

ence between photons and electrons, and the Monte Carlo-Data difference is represented by the linear term $(A + B \times E_T)$. The additional inefficiency at low E_T due to calorimeter noise is given by the exponential turn on $(1.0 - D \times e^{(E_{CLUS} \times E)}$. E_{CLUS} is the energy of the cluster, since the isolation uses energy instead of E_T). The resultant parameters, their errors, and the effect on the Wγ photon efficiency are summarized in Table 6.12.

Parameter	Value	Error	% Error on Photon ID
A	0.810	0.0056	0.658
B	0.0033	0.0003	0.485
D	0.166	0.007	0.230
E	-0.073	0.002	0.170

Table 6.12 Photon Identification Efficiency Parameters, and their effect on the Wγ photon efficiency.

The final average photon identification efficiency is estimated to be 0.811 ± 0.007.

Chapter 7
Backgrounds

The main background to W$\gamma \rightarrow \mu\nu\gamma$ is Wj$\rightarrow \mu\nu$j where the jet is misidentified as a photon. This background will be measured from the data. Two smaller backgrounds, which are not as easily distinguishable from Wγ events are Zγ and W$\gamma \rightarrow \tau\nu\gamma$. Z$\gamma$ events in which one muon is lost or unreconstructed provides exactly the event geometry of a Wγ event. W$\gamma \rightarrow \tau\nu\gamma$ where the τ decays to a muon provides an additional background, though not kinematically favored. The same parametrized Monte Carlo used for the calculation of the efficiencies is used to estimate these backgrounds. There is an additional background from events which produce a muon, an electron and missing E_T. These 'leX' (lepton, electron plus X, where X is the $\not\!\!E_T$) events mimic Wγ events if the track associated with the electron is not reconstructed. This background is treated inclusively and estimated from the data.

7.1 W+jet Background

To measure the background from W+j events, the rate at which a jet fakes a real photon is estimated from the data as a function of jet E_T. Then, using a sample of W+j events selected from the same trigger as the signal, the number of W+j background events as a function of jet E_T is estimated. The angular distribution of the W+j events may be used to find the shape of the background in the charge signed

rapidity difference (for the radiation amplitude zero).

7.1.1 Rate for a Jet to Fake a Photon

To estimate the W+j background, the rate at which a jet fakes a photon is measured from the data. This is done by selecting multijet QCD events, and finding the frequency with which a good electromagnetic object is reconstructed, as opposed to a good jet. Events are selected in the following way:

- Select events that were triggered on a jet trigger. For this analysis, events from the following triggers are used:
  - Jet25_TT_NG: Two Level 1 (total energy) calorimeter towers above 5 GeV, as well as a jet reconstructed at Level 3 with minimum E_T of 25 GeV.
  - Jet45_TT: Two Level 1 calorimeter towers above 5 GeV, as well as a jet reconstructed at Level 3 with minimum E_T of 45 GeV.
- In each event, the lead (highest E_T) reconstructed jet was required to match up to all the trigger criteria.
  - Two Level 1 calorimeter towers above 5 GeV were required to be matched to the lead jet. To be matched, the towers were required to be within 0.3 in η and ϕ.
  - A Level 3 jet, with E_T above the appropriate threshold was required to be within dR < 0.5 of the lead offline reconstructed jet.

- The highest E_T jet was also required to pass the following quality criteria (as defined in Section 4.3.3):
  - $0.05 <$ Jet Electromagnetic fraction (JetEMF) < 0.7
  - Jet Coarse Hadronic Fraction (JetCHF) < 0.1
  - Jet hot fraction (JetHOTF)< 3
  - Jetn90 > 1
  - At least 6 tracks within the jet cone radius (0.5)
  - Detector $|\eta| < 1.1$ OR $1.6 <$ Detector $|\eta| < 2.5$
- With the trigger criteria met by the lead jet, the other objects in the event were effectively unbiased by the trigger requirements. The jets and EM objects found constitute the sample from which the Jet-EM fake rate was determined. Good jets for the fake rate were required to pass the following cuts:
  - $0.05 <$ Jet Electromagnetic fraction (JetEMF)< 0.9
  - Jet Coarse Hadronic Fraction (JetCHF) < 0.1
  - Jet hot fraction (JetHOTF)< 3
  - Jetn90 > 1
  - Detector $|\eta| < 1.1$

The fake rate is calculated by dividing the number of unbiased good electromagnetic objects (where good electromagnetic objects are defined in Section 5.2) in these events by the total number of unbiased objects (jets and electromagnetic objects) found:

$$f = \frac{N_{EM}}{N_{EM} + N_{JET}}. \tag{7.1}$$

Unbiased here indicates that due to the matching of the lead jet to all of the required trigger criteria, ostensibly the biases due to the E_T requirement at the the trigger level have been taken into account. This gives the frequency with which objects passing photon identification cuts will be produced in QCD events (such as the objects produced in W+jet events).

With the application of the jet energy scale corrections, the spectrum of available jet objects began only at approximately 12 GeV (the jet reconstruction threshold by default is set at 8 GeV of uncorrected E_T). To characterize the fake rate for energies down to 8 GeV (of corrected E_T), the jet reconstruction was re-run, with the threshold lowered to 3.5 GeV. This has the effect of making available objects in the appropriate energy range (see Figure 7.1).

The uncertainty of the extrapolation of the jet energy scale (JES) corrections is a known problem (JES corrections are certified only above 15 GeV). The final estimate of the number of background events is checked against a separate, lower statistics method of estimating the background which does not depend upon the energy scale

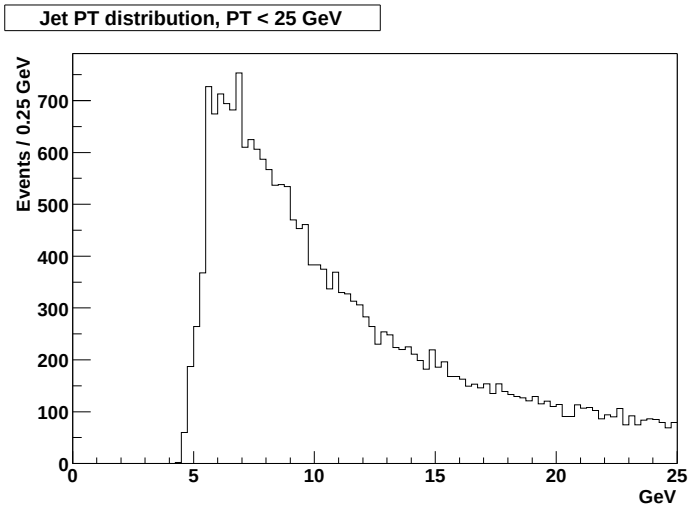

Figure 7.1 Jet E_T Spectrum for Adjusted Jet Threshold and Jet Energy Scale Correction, for Good Jets.

correction, discussed in Section 7.1.3.

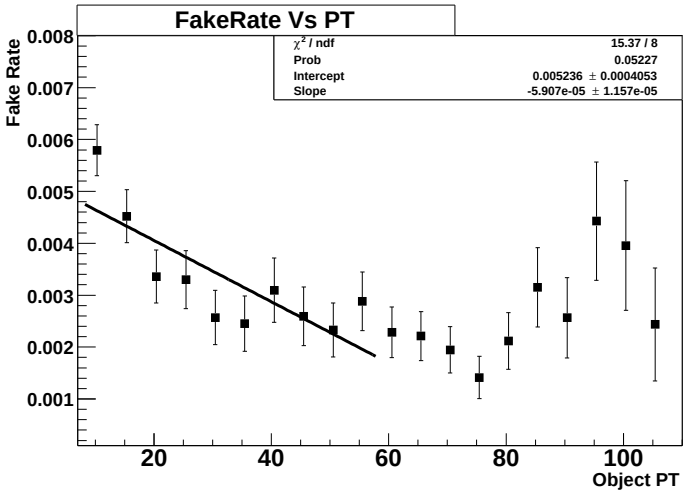

Figure 7.2 Rate for Jet to Fake Photon, with JES Correction. A line is fit to the range of 8-58 GeV which will be used in the calculation of the W+j background where no direct photon contribution is assumed.

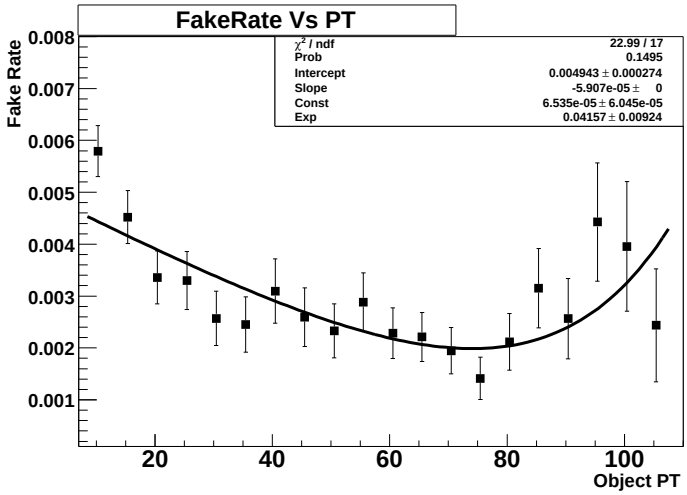

Figure 7.3 Rate for Jet to Fake Photon, with JES Correction. A line plus the Run I direct photon contribution is fit to the full range. The line will represent the actual fake rate after subtraction of direct photon contribution.

Further complicating this calculation is the increasing contribution of real photons from direct QCD photon production, which provides good photons in our sample of QCD jets, with a fraction that increases with E_T. From Run I studies [39], the purity of the direct photon sample increased from approximately 10% at 10 GeV to close to 80% at 100 GeV. One can see from Figure 7.2, that the rate in the high E_T does show a corresponding increase in the fake rate, inconsistent with the low E_T behavior. If it is assumed that the increase in the fake rate at high E_T is due to direct photon contribution, the same functional form as from Run I can be used. This background of photons can then be fit and subtracted. From Run I, the functional form of the

purity of photons was:

$$P = 1 - e^{a+b\times E_T} \tag{7.2}$$

Therefore, the fake rate is fit to a line, which represents the prior behavior of the fake rate in Run I, plus the exponent in Equation 7.2. Since at higher E_T this contribution is high, the subtraction of this exponent is assessed as an error by doing a linear fit in the range 8-58 GeV, and taking the difference (See Figures 7.2 and 7.3). For fitting the full fake rate, the slope from the linear fit at low E_T was used, to better fit the other parameters (such as the intercept). In Run I, the amount of direct photon contribution was determined by studies from the full simulation. At the present time, since the amount of material in the full simulation is believed to be insufficient to represent the actual detector configuration, these studies cannot be repeated.

7.1.2 W+j Estimation Using the Fake Rate

For the final estimate of the number of W+j events channel, a sample of W+j events was used. In these events the muon was required to pass the same cuts as in the selection of the Wγ signal. Then at least one good jet is required to be present and satisfy all the necessary event geometry (separated by dR >0.7, missing transverse energy, *etc.*). The jets that satisfy all of the cuts are binned in E_T, in the same bins as the fake rate from the previous section. Then the number of jets in each bin is multiplied by the corresponding rate to fake a photon to give an estimate of the

number of W + 'fake photon' events at each E_T.

The final estimate of the number of W+j events is shown in Table 7.1.

Data Set	N_{Wj}, exp. fit	N_{Wj}, linear fit	Stat. Err.	Sys. Err.
MU_W_L2M5_TRK10	8.8	9.49	0.23	0.69
MUW_W_L2M3_TRK10	28.7	30.9	0.76	2.20
MUW_A_L2M3_TRK10	24.3	26.2	0.63	1.90
Total	61.8	66.6	1.61	4.80
With $M_{T3} > 90$ GeV				
MU_W_L2M5_TRK10	4.86	5.27	0.12	0.41
MUW_W_L2M3_TRK10	15.9	17.2	0.39	1.31
MUW_A_L2M3_TRK10	13.3	14.4	0.32	1.10
Total	34.1	36.9	0.83	2.80

Table 7.1 Summary of Estimated W+j events from data.

7.1.3 Ratio Method

A separate estimate of the W+j background may be made using only electromagnetic objects. This avoids the complications arising from the JES corrections. This method relies on the assumption that the same fraction of electromagnetic objects reconstructed in QCD events are reconstructed as 'good' as in the signal sample. Thus if one knows the ratio of 'good' QCD electromagnetic object to 'bad' objects, then one may count the number of 'bad' electromagnetic objects in the signal sample, and use the ratio to calculate the number of background reconstructed as 'good'.

To measure this ratio, the sample of QCD events described in Section 7.1.1 is used. The number of electromagnetic objects that pass all the selection cuts is counted as

before. The number of events which have an ϕ-width $> 14\text{cm}^2$ and pass all other selection cuts is also counted, and the ratio computed.. This ratio may then be multiplied by the number of EM objects in the signal samples which satisfy ϕ-width > 14, to give an independent estimate of the number of background events in the signal region. This ratio is shown as a function of object E_T in Figure 7.4. The number of events calculated in this way is summarized in Table 7.2.

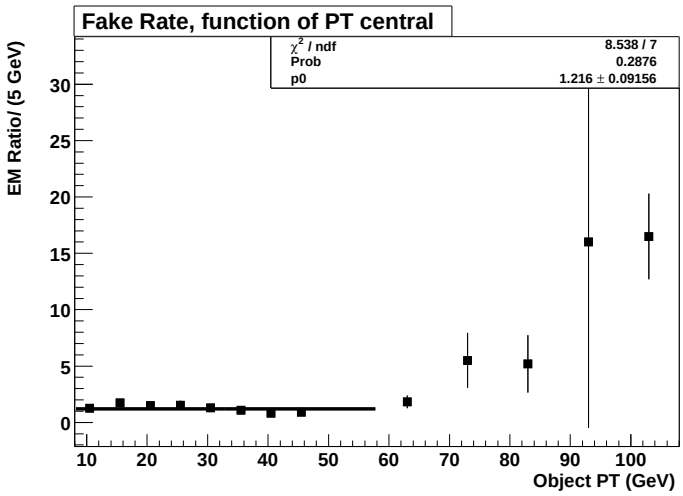

Figure 7.4 Ratio of Good EM objects to Bad (ϕ-width > 14) EM objects in QCD events. The ratio is fit to a constant.

7.2 leX Background

The leX background to Wγ is the number of events in which an electron in the calorimeter is misidentified as a photon. This is generally due to inefficiency in the reconstruction of tracks in the central tracker. A variety of processes can cause this

Data Set	N_{bkg}	Error
MU_W_L2M5_TRK10	6	2.9
MUW_W_L2M3_TRK10	30	6.5
MUW_A_L2M3_TRK10	36	7.2
Total	72	9.2
With $M_{T3} > 90$ GeV		
MU_W_L2M5_TRK10	4.8	2.4
MUW_W_L2M3_TRK10	12	3.7
MUW_A_L2M3_TRK10	18	4.6
Total	34.8	6.5

Table 7.2 Summary of Estimated QCD background using Ratio Method.

event topology ($t\bar{t}$, Z$\rightarrow \tau\tau$ etc.), and are dealt with inclusively.

Before the requirement on track isolation is made, the entire set of muon+electromagnetic object events contains some amount of Wγ, leX and the other backgrounds. If instead of requiring track isolation, a track match is required, then one has selected the events with muon, electron and missing E_T *i.e.*:

$$N_{trackmatched} = N_{leX} \times \epsilon_T. \tag{7.3}$$

The efficiency for a track to be matched to an EM object (ϵ_T) for the central region, is taken to be the applicable tracking efficiency.

To find the estimated leX background, the total number of leX events (N_{leX}) can then be multiplied by the inefficiency associated with the track isolation cut for electrons (1-ϵ_{TrkIso}). Thus the final expected number of leX events that are misidentified as signal is:

$$N_{leX} = \frac{(1. - \epsilon_{TrkIso})}{\epsilon_T} \times N_{trackmatched}. \quad (7.4)$$

The efficiency (and thus the inefficiency) of the track match, and the track isolation, can be measured from electrons in Z→ee. By reconstructing the invariant mass of the Z without using tracking quantities, the efficiency with which an electron appears as non-isolated from tracks may be computed, in the same was as the isolation efficiency in Section 6.2.4.

Using a sample of only central Z events, selected on a non-tracking trigger, the invariant mass distribution in Figure 7.5 was formed. The fit to the plot of two isolated objects (thus no tracks found) generously assumes that there was in fact some contribution from Z events, though by eye, none are obvious. Using the fits to all three plots, the efficiency of the track isolation to identify electrons as non-isolated is 0.945 ± 0.014. If one calculates the efficiency just from the one non-isolated and two non-isolated cases without the zero non-isolated case, the efficiency is calculated to be 0.946 ± 0.012. The difference will be taken as a systematic error, though much smaller than the uncertainties given from the fits.

Likewise, the efficiency for associating a track with an electron (from Equation 7.3, the actual cut is the spatial χ^2 probability greater than 0.01) may be calculated using the same di-electron sample. In Figure 7.6, the corresponding plot of the number of Z→ee events with no tracks matched, one track matched, and both tracks matched is

shown. The efficiency using this method is found to be 0.895 ± 0.026, using the fits. As before, if one calculates the efficiency without the neither matched information, the efficiency is 0.916 ± 0.011.

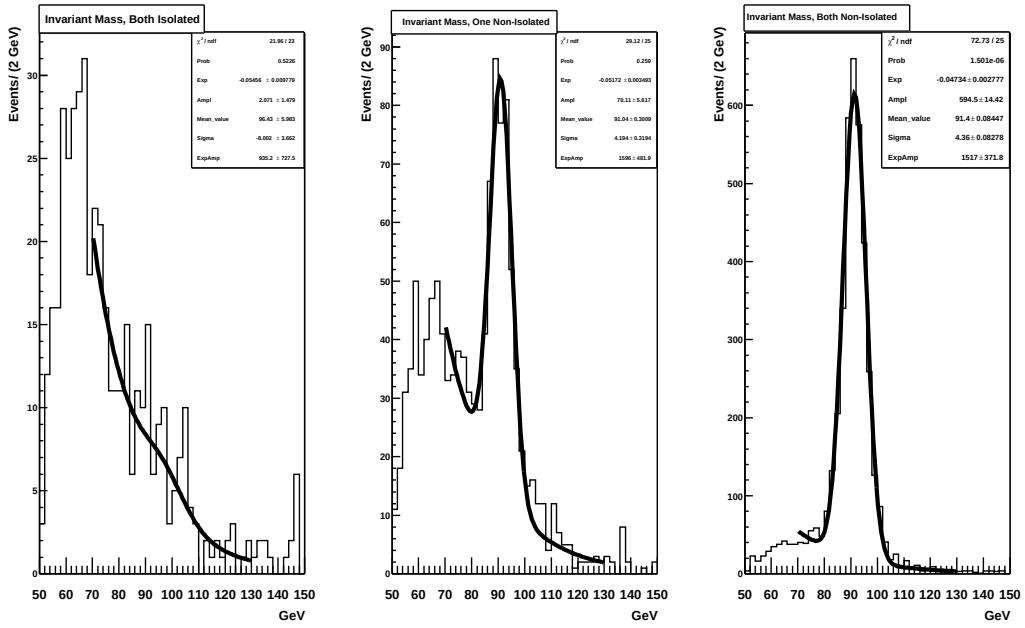

Figure 7.5 Invariant Mass in Z→ ee events. The three separate plots correspond to neither electron reconstructed as non-isolated, only one reconstructed as non-isolated, and both reconstructed as non-isolated respectively. Non-isolated corresponds to the electromagnetic object failing the isolation criteria defined for the photon identification.

This does not take into account the fake track rate (the rate at which a random track is incorrectly associated with the electromagnetic object), which can be assessed as a systematic error on the estimate of the number of track matched leX events (though in comparison to the statistical error on the number of track matched events,

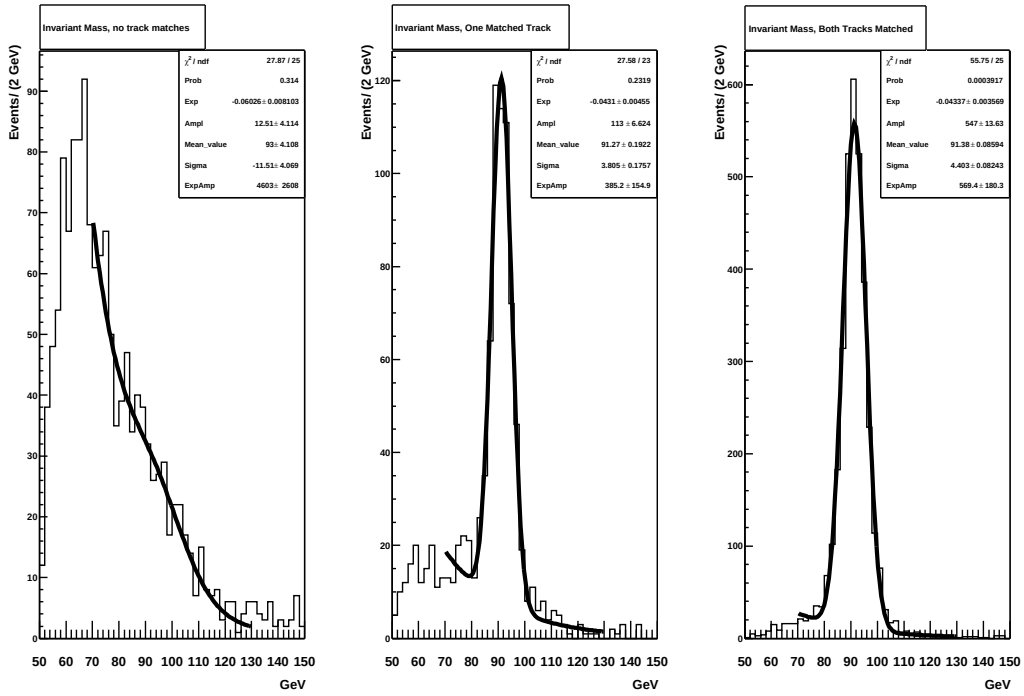

Figure 7.6 Invariant Mass in Z→ ee events. The three separate plots correspond to neither electron reconstructed as track matched, only one reconstructed as matched, and both reconstructed as matched respectively.

this error is small). With that, and the number of track matched events from the data (summarized in Table 7.3), the number of expected leX events in the data is calculated. Due to the possible presence of real Wγ events in the sample, this estimate is, if anything, conservative.

7.3 Z+γ

For the Z$\gamma \rightarrow \mu\mu\gamma$ background, the muon must have escaped detection in the muon system. This may have occurred either due to inefficiency in the reconstruction,

Data Set	$N_{trackmatched}$	N_{lex}	Statistical Error	Systematic Error
MU_W_L2M5_TRK10	0	0	0	0
MUW_W_L2M3_TRK10	6	0.36	0.17	0.007
MUW_A_L2M3_TRK10	6	0.36	0.17	0.007
Total	12	0.72	0.24	0.014
With $M_{T3} > 90$ GeV				
MU_W_L2M5_TRK10	0	0	0	0
MUW_W_L2M3_TRK10	2	0.12	0.09	0.002
MUW_A_L2M3_TRK10	2	0.12	0.09	0.002
Total	4	0.23	0.12	0.004

Table 7.3 Summary of Estimated leX events from data.

or due to missing the fiducial acceptance of the detector. The veto on additional stiff tracks helps to compensate for muons that miss the muon system. The track left by the muon must also not have been reconstructed, or have been smaller in transverse momentum than the veto of 15 GeV/c on tracks in the event. Both of these probabilities are quantified in the measurement of the muon reconstruction efficiency and the tracking efficiency. Using $Z\gamma \rightarrow \mu\mu\gamma$ Monte Carlo [40], the ratio of the $W\gamma$ acceptance to the $Z\gamma$ acceptance (given the veto and the efficiency of the requirements) may be estimated. In addition, the Monte Carlo also provides an estimate of the ratio of the $Z\gamma$ cross section to the $W\gamma$ cross section, which must also be included in the calculation. The $Z\gamma$ cross section from the Monte Carlo is summarized in Table 7.4.

$$f_{Z\gamma} = \frac{R_{\frac{Z\gamma}{W\gamma}} \times A_{Z\gamma} \times \epsilon_{vetoZ\gamma}}{A_{W\gamma} \times \epsilon_{vetoW\gamma}} \tag{7.5}$$

PDF	$\sigma_{Z\gamma}$ (pb^{-1}))	$\sigma_{W\gamma}$(pb^{-1}))	Ratio
CTEQ5L	7.477	16.58	0.451
GRVLO98	6.735	15.08	0.447
MRSR2	7.742	16.91	0.458

Table 7.4 Zγ and Wγ cross sections from the Monte Carlo, with different PDFs used.

The total fraction of events passing all selection cuts that are due to Zγ production is the ratio of the Zγ acceptance ($A_{Z\gamma}$) to the Wγ acceptance ($A_{W\gamma}$) scaled by the ratio of the Standard Model cross sections. In the ratio of the acceptances, the only efficiencies which do not cancel out are the kinematics, and the veto efficiency. Zγ has a slightly higher acceptance (since there are two muons which may fit within the acceptance), but a much lower veto efficiency ($\epsilon_{vetoZ\gamma}$). The acceptance for Zγ is estimated to be 0.133 $\pm$ 0.005, where the same error on the acceptance for Wγ (from PDF, smearing, etc.) has been assumed. The ratio of the cross sections has been taken to be 0.452 $\pm$ 0.008, based on the cross sections from Table 7.4. The final fraction of Zγ events is estimated to be 0.070 $\pm$ 0.008.

7.4 W$\gamma \rightarrow \tau\nu\gamma$

For W$\gamma \rightarrow \tau\nu\gamma$, the final event geometry for a tau decaying to a muon is the same as for the direct W$\gamma \rightarrow \mu\nu\gamma$. However, the kinematic efficiencies are quite different. The efficiency of a cut of 20 GeV/c on muon p_T and missing transverse energy is much lower for the case of the tau than for the muon. The subsequent decay of the tau into a muon gives some fraction of the lepton transverse momentum to the neutrino

as well as the muon, and thus the muon is found with a lower transverse momentum than for a W decaying directly into muon and neutrino.

$$f_{\tau\gamma} = \frac{B_{\tau\to\mu} \times A_{\tau\gamma}}{A_{W\gamma}} \tag{7.6}$$

To simulate the difference in kinematics, the same sample of Monte Carlo of Wγ was used, but the lepton changed to a tau, and then decayed to produce the proper final state quantities. Using the Monte Carlo, and the branching fraction of $\tau \to \mu$ (from [23], the branching fraction of $\tau \to \mu$ is 0.1737 ± 0.00060), the total fraction of W$\gamma \to \tau\nu\gamma$ may be estimated. The acceptance for W$\gamma \to \tau\nu\gamma \to \mu\nu\nu\gamma$ is estimated to be 0.0124 ± 0.0045. Thus the fraction was estimated to be 0.021 ± 0.002.

Chapter 8
Results and Conclusion

8.1 Cross Section

The final cross section times branching ratio is calculated in the following way:

$$\sigma_{p\overline{p}\to W\gamma+X}\times Br(\mu\nu\gamma+X) = \frac{(N - N_{Wj} - N_{leX}) \times (1 - \frac{R_{\frac{Z\gamma}{W\gamma}} \times A_{Z\gamma} \times \epsilon_{vetoZ\gamma}}{A_{W\gamma} \times \epsilon_{vetoW\gamma}} - \frac{B_{\tau\to\mu} \times A_{\tau\gamma}}{A_{W\gamma}})}{A_{W\gamma} \times \epsilon \times \epsilon_{vetoW\gamma} \times (L_1\epsilon_{L1^1}\epsilon_{L2^1} + L_2\epsilon_{L1^2}\epsilon_{L2^2} + L_3\epsilon_{L1^3}\epsilon_{L2^3})}. \tag{8.1}$$

In Equation 8.1, the total number of candidates (N) first has the number of leX (N_{leX}) and W+jet (N_{Wj}) background events subtracted. Then the fraction of the remaining candidates that are Zγ (see Equation 7.5) and Wγ decays to τ (see Equation 7.6) are subtracted. The denominator is made up of two parts: the common acceptance (A) and efficiencies (ϵ, $\epsilon_{vetoW\gamma}$) and the individual Level 1 and Level 2 efficiencies from each run range, weighted by the individual luminosities ($L\epsilon_{L1}\epsilon_{L2}$). The final efficiencies and backgrounds are summarized in Table 8.1.

It is important to note that in the full calculation of the cross section, the veto efficiency is used not only in the total acceptance times efficiency, but also in the calculation of the Zγ background fraction. Likewise, the Wγ acceptance appears in the denominator in the calculation of both the Zγ and $\tau\gamma$ fractions. The full propagation of these individual errors has been properly done (see Appendix A).

The cross section times branching fraction for W$\gamma \to \mu\nu\gamma$ is calculated to be 15.03

Quantity	Value	Combined Error (stat+sys)
Total Candidates	161	——
Acceptance	0.1033	0.0068
Medium Muon	0.8470	0.0100
Central Track	0.9830	0.0096
Veto	0.9421	0.0036
Isolation	0.9050	0.0174
L1 (MU_W_L2M5_TRK10)	0.7740	0.0070
L2 (MU_W_L2M5_TRK10)	0.8121	0.0069
L1 (MUW_W_L2M3_TRK10)	0.8100	0.0053
L2 (MUW_W_L2M3_TRK10)	0.9758	0.0021
L1 (MUW_A_L2M3_TRK10)	0.8643	0.0038
L2 (MUW_A_L2M3_TRK10)	0.9705	0.0019
L3 Track	0.9660	0.0100
Photon Identification	0.8111	0.0074
N_{W+j}	61.8	5.06
N_{leX}	0.71	0.24
$f_{Z\gamma}$	0.070	0.008
$f_{\tau\gamma}$	0.021	0.002

Table 8.1 Summary of Efficiencies and Backgrounds used in Cross Section Calculation.

$\pm$ 1.936 (stat) $\pm$ 1.400 (sys) $\pm$ 0.977 (lumi) pb. The dominant systematic error in the calculation is the error on the Wγ acceptance, which in turn is dominated by the ϕ module position resolution. This error will eventually be reduced as a better understanding of the calorimeter position resolution is gained, and larger statistics of Z$\rightarrow$ ee events obtained. This contribution to the systematic error is only slightly larger than that of the error on the W+j background estimate. In future studies, greater statistics will also aid in a better understanding of the background.

The dominant error is statistical. The statistical error dominates because of the large number of background events. If there were no background, the fractional error from the statistics of the candidates would simply be $\frac{\sqrt{N}}{N}$. Instead, the fractional error due to the statistics becomes $\frac{\sqrt{N}}{N-b}$, where b is the total number of background events. The Standard Model cross section (using the Baur Monte Carlo) for this process is calculated to be 16.19 $\pm$ 0.40 (PDF uncertainty) pb. Thus the measured value is in good agreement with the Standard Model prediction.

8.2 Coupling Limits

Limits on anomalous couplings are obtained using the method described in Section 2.3. Using the Baur Monte Carlo, events were generated with non-zero anomalous coupling parameters. Events were generated in a 7 $\times$ 7 grid in $\Delta\kappa$ and λ. The grid covered from $\Delta\kappa$=0.9 to -0.9 (in steps of 0.3), and λ=0.39 to -0.39 (in steps

of 0.13)*. In addition to these finely spaced points, eight points at large values of the anomalous coupling values were generated (The large values of the anomalous couplings were chosen to be just within the unitarity limits. See Figure 8.1.). These points were generated so that the likelihood would be well defined at the limits of the anomalous coupling space. Thus, when the limit is fit, the likelihood contours are constrained both near the minimum values, and near the unitarity limits. At each point, the Monte Carlo cross section was calculated, and sets of 4-vectors were produced (for event kinematics). These 4-vectors were smeared using the same parametrized Monte Carlo used in the calculation of the acceptance times efficiency for the cross section. At each point, the acceptance times efficiency for the given set of anomalous couplings was calculated. The uncertainty in the acceptance at each point in the grid from effects such as the parton distribution functions, z-vertex distribution, and parametrized smearing is assumed to be the same as at the Standard Model point (assessed in the cross section)†.

*The grid endpoints were chosen to approximate the DØ limits on anomalous couplings from Run I. Each point was generated with a form factor scale (as in Equation 2.3) Λ=1500 GeV. The Standard Model point of $\Delta\kappa$=0 and λ=0 is the center of the grid.

†As a cross check, all of the systematic variations of smearing, boost, vertex, and parton distribution function were repeated at one of the large values of anomalous coupling ($\Delta\kappa = 2$, $\lambda = 1.5$). The fractional systematic error was found to differ by 0.5% compared to the Standard Model point, whereas the acceptance and cross section were much larger.

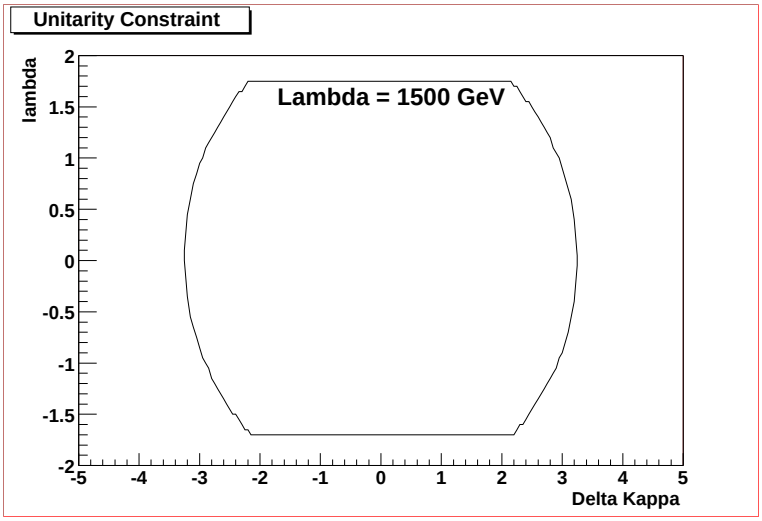

Figure 8.1 Unitarity Contour in terms of $\Delta\kappa$ and λ.

8.2.1 Likelihood in Photon E_T

The expected number of events at each anomalous coupling point was calculated using the cross section, the acceptance times efficiency, and the integrated luminosity. The photon E_T spectrum for the Monte Carlo events was also produced, and normalized to the expected number of events. Using the prescription for the likelihood in Equation 2.16, the log likelihood at each point was calculated. For the integration over the nuisance parameters, a Simpson's Rule numerical integration was performed [41]*. The likelihood was formed in bins of photon E_T. The binning chosen is shown in Table 8.2, along with the number of signal candidates and es-

*The likelihood calculation separates the nuisance parameters into three separate factors, which are uncorrelated. These factors are: the signal acceptance times efficiency, the background, and the error on the Monte Carlo prediction (dominated by the luminosity uncertainty).

timated background in each bin. The highest E_T bin is constructed to contain no signal candidates. In the case that the Monte Carlo predicts a significant contribution (from anomalous couplings) in this bin, then this adds additional information to the likelihood and can provide a more stringent limit. In the case where no events are predicted in this bin (in the Standard Model or the anomalous coupling points), this adds no additional information and does not alter the limits.

Bin (GeV)	Candidates	Background Estimate	Background Error (stat+sys)
8-13	28	13.5	1.05
13-18	12	8.06	0.68
18-23	10	5.14	0.49
23-28	7	3.42	0.37
28-33	4	2.37	0.27
33-38	2	1.37	0.18
38-43	2	1.14	0.17
43-48	0	0.700	0.109
48-68	4	1.82	0.18
68-118	3	0.765	0.062
118-up	0	0.184	0.006

Table 8.2 Likelihood Binning, along with number of candidates and background estimate.

The distribution of the likelihood as calculated at each point in the anomalous coupling grid is shown in Figure 8.2. Using the likelihood at each point in the grid, a function was fit to interpolate between each point such that the 95% confidence level contour may be generated. The form:

$$-ln(P) = c_0 + c_1\Delta\kappa + c_2\lambda + c_3\Delta\kappa^2 + c_4\lambda^2 + c_5\Delta\kappa\lambda, \tag{8.2}$$

was found to give a very good fit. Variation on this form by removing the cross term and removing terms that were linear in $\Delta\kappa$ or λ (or both) resulted in worse fits, but very similar limits. Additional terms (such as cubic terms in the coupling parameters) were found to not be favored.

The contour (found by fitting the likelihood to the form of Equation 8.2) is shown in Figure 8.3. This contour is generated by ascending 3.0 units of negative log likelihood from the minimum of the fit. From the fit to the likelihood, the limit on $\Delta\kappa$ when λ=0, and the limit on λ when $\Delta\kappa$=0 may also be obtained. These limits are: -1.05 $<\Delta\kappa <$ 1.04 for λ=0; -0.28 $< \lambda <$ 0.27 for $\Delta\kappa$=0.

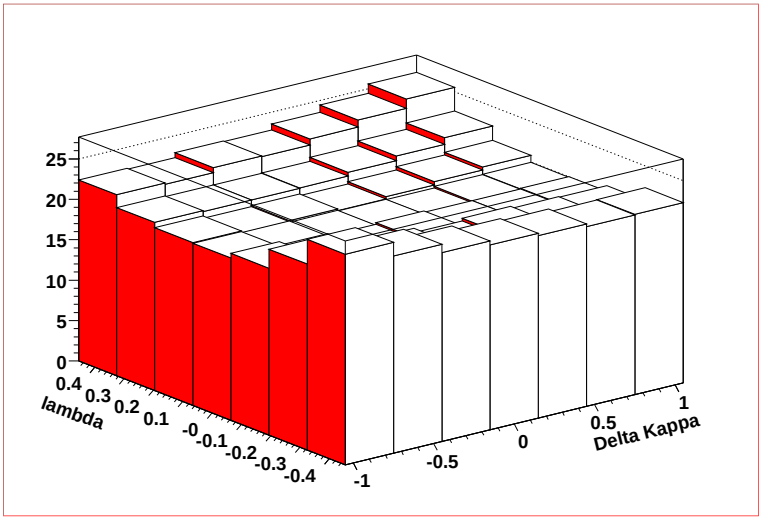

Figure 8.2 Binned Negative Log Likelihood for each point in the anomalous coupling grid.

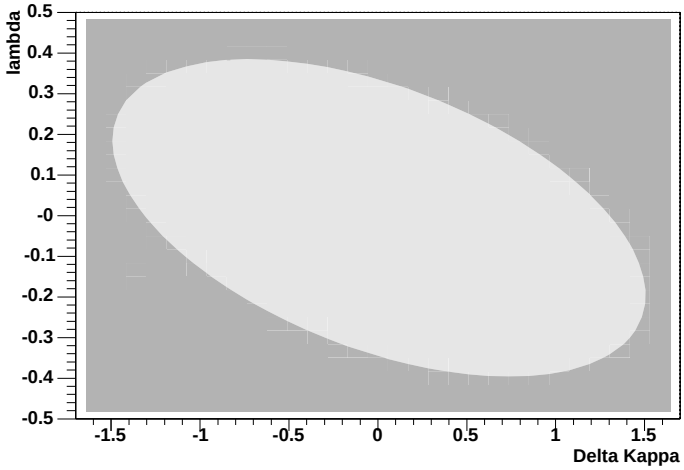

Figure 8.3 95% Confidence Level contour on $\Delta\kappa$ and λ from the fit of the negative log likelihood.

8.2.2 Likelihood in Photon E_T and Charge Signed Rapidity Difference

Figure 8.4 shows the luminosity normalized charge signed rapidity difference for several points within the anomalous coupling grid. There is a large difference between the Standard Model point and the anomalous coupling Monte Carlo. This is especially noticeable in those points with large values of $\Delta\kappa$. It is then reasonable to attempt to gain information by making a two dimensional likelihood in charge signed rapidity difference and photon E_T to attempt to exploit this additional information.

Figure 8.5 shows the two dimensional plot of photon E_T versus charge signed rapidity difference for the selected candidates. Figure 8.6 shows the same distribution, only for the Standard Model Monte Carlo. It is interesting to note that the Standard Model plot suggests that the highest E_T photon candidate is located where the

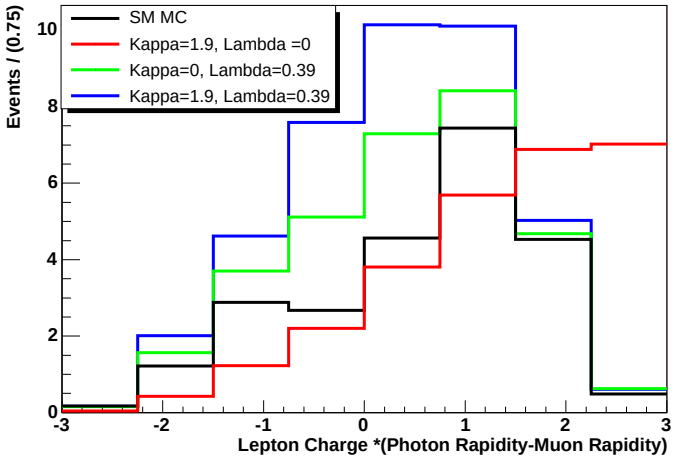

Figure 8.4 Candidate Events binned in photon E_T and charge signed rapidity difference. Standard Model would predict such an event to occur.

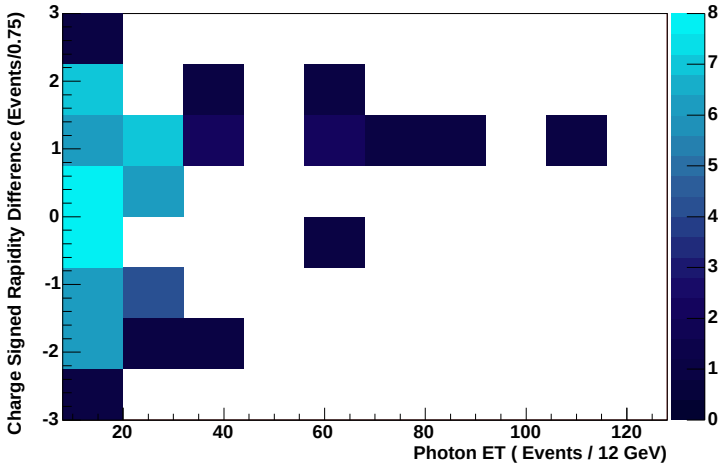

Figure 8.5 Candidate Events binned in photon E_T and charge signed rapidity difference.

Using the same prescription as the one dimensional case, the candidates were

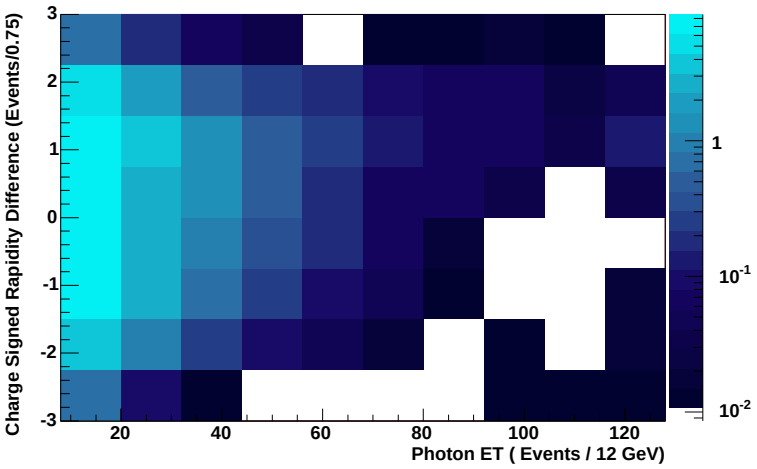

Figure 8.6 Standard Model prediction, binned in photon E_T and charge signed rapidity difference. Note log scale in z.

binned in eight equal bins of charge signed rapidity difference, and ten equal bins of photon E_T. Again, the likelihood was fit, and the 95% confidence level contour generated. From the fit to the likelihood, the limit on $\Delta\kappa$ when λ=0, and the limit on λ when $\Delta\kappa$=0 may be obtained. These limits are: -1.09 $<\Delta\kappa <$ 1.07 for λ=0; -0.27 $< \lambda <$ 0.27 for $\Delta\kappa$=0.

8.3 Rapidity Difference

The efficiencies have been parametrized to take into account η dependent effects, and included in the smearing. Therefore, in comparing the rapidity difference in data (after performing the appropriate background subtraction) with the Monte Carlo these η dependent effects have been taken into account. What remains is to show

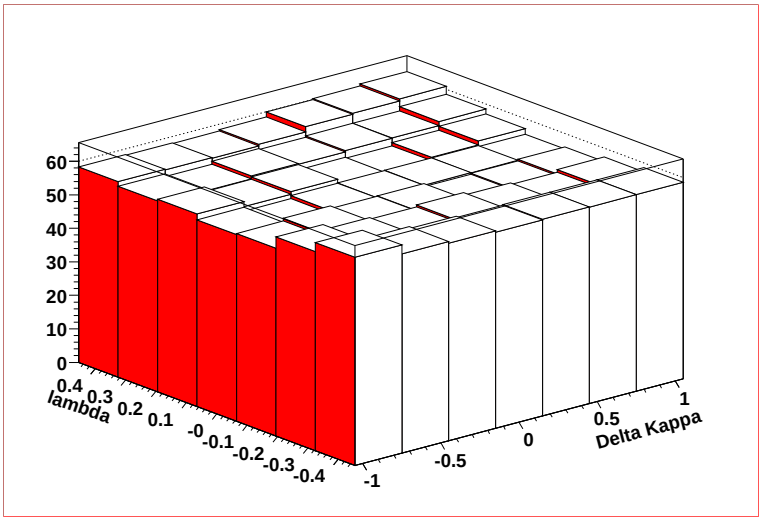

Figure 8.7 Binned Negative Log Likelihood for each point in the anomalous coupling grid, formed in two dimensions.

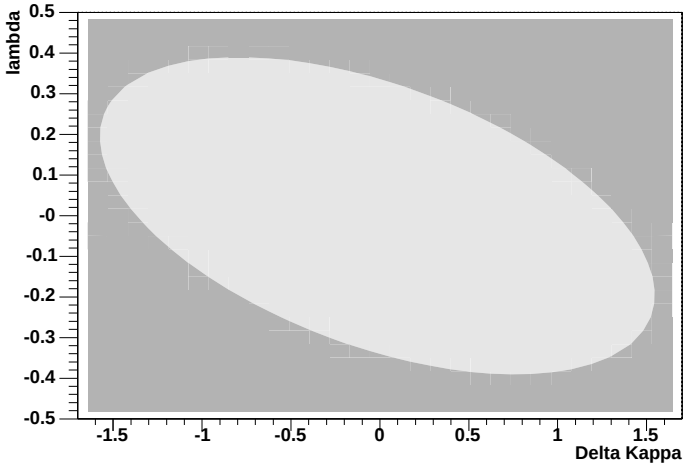

Figure 8.8 95% Confidence Level contour on $\Delta\kappa$ and λ from the fit of the negative log likelihood, formed in two dimensions.

that the rapidity difference most closely resembles the Standard Model couplings (with respect to this distribution) as opposed to other couplings which eliminate the zero.

The couplings shown for contrast with the Standard Model behavior are chosen by setting the different coupling moments to zero. The $U_{EM}(1)$ coupling only ($\kappa = \lambda$=0, no electric quadrupole, or magnetic dipole moments), the magnetic dipole moment equal to zero ($1 + \kappa + \lambda = 0$), and the electric quadrupole moment equal to zero (κ - $\lambda = 0$) were selected. The exact coupling parameters chosen (since the last two have an infinite number of solutions) are summarized along with the results from the χ^2 tests and Kolmogorov tests in Table 8.3. One can see from the χ^2 tests and Kolmogorov tests that the Standard Model point is the most likely. However, the test show that it is not much more likely than the $U_{EM}(1)$ case. See Figure 8.10 for the rapidity difference for each of the selected couplings. With larger statistics it will be possible to use these tests to firmly establish the nature of the distribution ($U_{EM}(1)$ or Standard Model).

κ	λ	χ^2	χ^2 Prob.	Kolmogorov Test
1	0	1.90	0.984	1.0
0	0	2.62	0.956	1.0
-0.5	-0.5	10.0	0.263	0.23
-1	0	5.83	0.667	0.71

Table 8.3 Likelihood for the different anomalous coupling parameters chosen, in bins of charge signed rapidity difference.

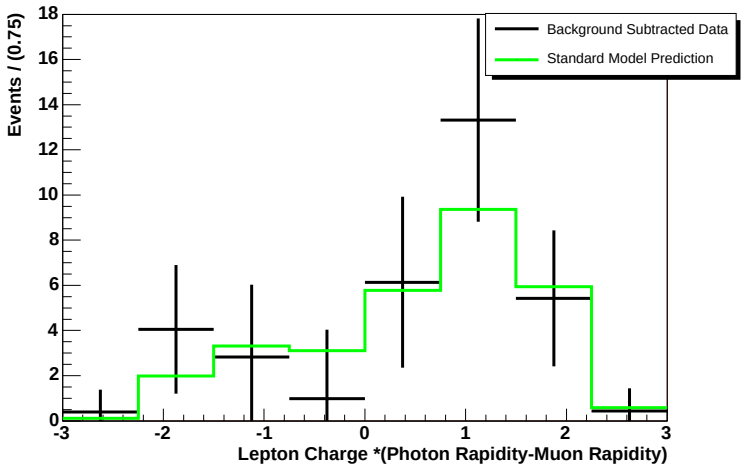

Figure 8.9 Charge Signed Rapidity Difference from Data (background subtracted). Standard Model is shown for comparison.

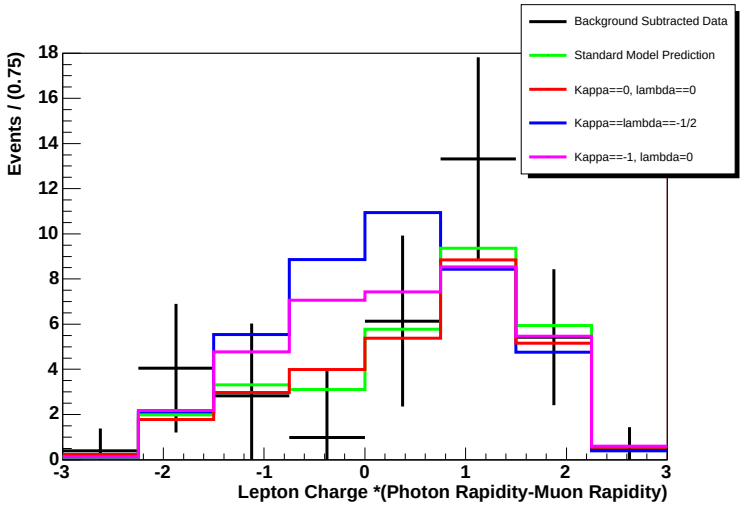

Figure 8.10 Charge Signed Rapidity Difference from Data (background subtracted). Also shown are the anomalous coupling points corresponding to the different coupling moments turned off.

8.4 Summary

The cross section times branching ratio for W$\gamma \rightarrow \mu\nu\gamma$ is calculated to be 15.03 $\pm$ 1.94 (stat) $\pm$ 1.40 (sys) $\pm$ 0.98 (lumi) pb, in good agreement with the Standard Model prediction of 16.19 $\pm$ 0.40 (PDF uncertainty) pb. Limits on anomalous Wγ couplings have been set at 95% confidence level. The one dimensional limits obtained from the likelihood fit are: -1.05 $<\Delta\kappa <$ 1.04 for λ=0 and -0.28 $< \lambda <$ 0.27 for $\Delta\kappa$=0. The rapidity difference from the data has been shown, as well as the consistency of the data with the Standard Model.

Appendix A
Cross Section Error Calculation

The equation for the cross section is shown in Equation 8.1. The statistical error on the cross section is:

$$\Delta\sigma_{p\overline{p}\rightarrow W\gamma+X} \times Br(\mu\nu\gamma + X)(stat) = \sqrt{N} \times \frac{(1 - \frac{R_{\frac{Z\gamma}{W\gamma}} \times A_{Z\gamma} \times \epsilon_{vetoZ\gamma}}{A_{W\gamma} \times \epsilon_{vetoW\gamma}} - \frac{B_{\tau\rightarrow\mu} \times A_{\tau\gamma}}{A_{W\gamma}})}{A_{W\gamma} \times \epsilon \times \epsilon_{vetoW\gamma} \times (L_1\epsilon_{L1^1}\epsilon_{L2^1} + L_2\epsilon_{L1^2}\epsilon_{L2^2} + L_3\epsilon_{L1^3}\epsilon_{L2^3})}. \quad (A.1)$$

As previously stated, care must be taken with the terms which appear multiple times so that the proper systematic error may be calculated. Since this equation has been written in terms of independent quantities, by taking the partial derivatives with respect to these factors, the full systematic error on the cross section may be derived:

$$\begin{aligned}
&\Delta\sigma_{p\overline{p}\rightarrow W\gamma+X} \times Br(\mu\nu\gamma + X)(sys) = \\
&-\Delta N_{leX} \times \frac{(1 - \frac{R_{\frac{Z\gamma}{W\gamma}} \times A_{Z\gamma} \times \epsilon_{vetoZ\gamma}}{A_{W\gamma} \times \epsilon_{vetoW\gamma}} - \frac{B_{\tau\rightarrow\mu} \times A_{\tau\gamma}}{A_{W\gamma}})}{A_{W\gamma} \times \epsilon \times \epsilon_{vetoW\gamma} \times (L_1\epsilon_{L1^1}\epsilon_{L2^1} + L_2\epsilon_{L1^2}\epsilon_{L2^2} + L_3\epsilon_{L1^3}\epsilon_{L2^3})} \\
&-\Delta N_{Wj} \times \frac{(1 - \frac{R_{\frac{Z\gamma}{W\gamma}} \times A_{Z\gamma} \times \epsilon_{vetoZ\gamma}}{A_{W\gamma} \times \epsilon_{vetoW\gamma}} - \frac{B_{\tau\rightarrow\mu} \times A_{\tau\gamma}}{A_{W\gamma}})}{A_{W\gamma} \times \epsilon \times \epsilon_{vetoW\gamma} \times (L_1\epsilon_{L1^1}\epsilon_{L2^1} + L_2\epsilon_{L1^2}\epsilon_{L2^2} + L_3\epsilon_{L1^3}\epsilon_{L2^3})} \\
&-\Delta R_{\frac{Z\gamma}{W\gamma}} \times \frac{(N - N_{Wj} - N_{leX}) \times \frac{A_{Z\gamma} \times \epsilon_{vetoZ\gamma}}{A_{W\gamma} \times \epsilon_{vetoW\gamma}}}{A_{W\gamma} \times \epsilon \times \epsilon_{vetoW\gamma} \times (L_1\epsilon_{L1^1}\epsilon_{L2^1} + L_2\epsilon_{L1^2}\epsilon_{L2^2} + L_3\epsilon_{L1^3}\epsilon_{L2^3})} \\
&-\Delta A_{Z\gamma} \times \frac{(N - N_{Wj} - N_{leX}) \times \frac{R_{\frac{Z\gamma}{W\gamma}} \times \epsilon_{vetoZ\gamma}}{A_{W\gamma} \times \epsilon_{vetoW\gamma}}}{A_{W\gamma} \times \epsilon \times \epsilon_{vetoW\gamma} \times (L_1\epsilon_{L1^1}\epsilon_{L2^1} + L_2\epsilon_{L1^2}\epsilon_{L2^2} + L_3\epsilon_{L1^3}\epsilon_{L2^3})} \\
&-\Delta \epsilon_{vetoZ\gamma} \times \frac{(N - N_{Wj} - N_{leX}) \times \frac{R_{\frac{Z\gamma}{W\gamma}} \times A_{Z\gamma}}{A_{W\gamma} \times \epsilon_{vetoW\gamma}}}{A_{W\gamma} \times \epsilon \times \epsilon_{vetoW\gamma} \times (L_1\epsilon_{L1^1}\epsilon_{L2^1} + L_2\epsilon_{L1^2}\epsilon_{L2^2} + L_3\epsilon_{L1^3}\epsilon_{L2^3})}
\end{aligned}$$

$$
\begin{aligned}
&-\Delta B_{\tau\to\mu}\times\frac{(N-N_{Wj}-N_{leX})\times\frac{A_{\tau\gamma}}{A_{W\gamma}}}{A_{W\gamma}\times\epsilon\times\epsilon_{vetoW\gamma}\times(L_1\epsilon_{L1^1}\epsilon_{L2^1}+L_2\epsilon_{L1^2}\epsilon_{L2^2}+L_3\epsilon_{L1^3}\epsilon_{L2^3})}\\
&-\Delta A_{\tau\gamma}\times\frac{(N-N_{Wj}-N_{leX})\times\frac{B_{\tau\to\mu}}{A_{W\gamma}}}{A_{W\gamma}\times\epsilon\times\epsilon_{vetoW\gamma}\times(L_1\epsilon_{L1^1}\epsilon_{L2^1}+L_2\epsilon_{L1^2}\epsilon_{L2^2}+L_3\epsilon_{L1^3}\epsilon_{L2^3})}\\
&+\Delta A_{W\gamma}\times\left(\frac{(N-N_{Wj}-N_{leX})}{A_{W\gamma}\times\epsilon\times\epsilon_{vetoW\gamma}\times(L_1\epsilon_{L1^1}\epsilon_{L2^1}+L_2\epsilon_{L1^2}\epsilon_{L2^2}+L_3\epsilon_{L1^3}\epsilon_{L2^3})}\right)\\
&\qquad\times(\frac{R_{\frac{Z\gamma}{W\gamma}}\times A_{Z\gamma}}{A_{W\gamma}^2\times\epsilon_{vetoW\gamma}}+\frac{B_{\tau\to\mu}\times A_{\tau\gamma}}{A_{W\gamma}^2}-\frac{1}{A_{W\gamma}})\\
&-\Delta\epsilon\times\frac{(N-N_{Wj}-N_{leX})\times(1-\frac{R_{\frac{Z\gamma}{W\gamma}}\times A_{Z\gamma}\times\epsilon_{vetoZ\gamma}}{A_{W\gamma}\times\epsilon_{vetoW\gamma}}-\frac{B_{\tau\to\mu}\times A_{\tau\gamma}}{A_{W\gamma}})}{A_{W\gamma}\times\epsilon^2\times\epsilon_{vetoW\gamma}\times(L_1\epsilon_{L1^1}\epsilon_{L2^1}+L_2\epsilon_{L1^2}\epsilon_{L2^2}+L_3\epsilon_{L1^3}\epsilon_{L2^3})}\\
&+\Delta\epsilon_{vetoW\gamma}\times\left(\frac{(N-N_{Wj}-N_{leX})\times(1-\frac{R_{\frac{Z\gamma}{W\gamma}}\times A_{Z\gamma}\times\epsilon_{vetoZ\gamma}}{A_{W\gamma}\times\epsilon_{vetoW\gamma}}-\frac{B_{\tau\to\mu}\times A_{\tau\gamma}}{A_{W\gamma}})}{A_{W\gamma}\times\epsilon\times\epsilon_{vetoW\gamma}\times(L_1\epsilon_{L1^1}\epsilon_{L2^1}+L_2\epsilon_{L1^2}\epsilon_{L2^2}+L_3\epsilon_{L1^3}\epsilon_{L2^3})}\right)\\
&\qquad\times(\frac{R_{\frac{Z\gamma}{W\gamma}}\times A_{Z\gamma}\times\epsilon_{vetoZ\gamma}}{A_{W\gamma}\times\epsilon_{vetoW\gamma}^2}-\frac{1}{\epsilon_{vetoW\gamma}})\\
&-\Delta\epsilon_{L1^1}\times\frac{(N-N_{Wj}-N_{leX})\times(1-\frac{R_{\frac{Z\gamma}{W\gamma}}\times A_{Z\gamma}\times\epsilon_{vetoZ\gamma}}{A_{W\gamma}\times\epsilon_{vetoW\gamma}}-\frac{B_{\tau\to\mu}\times A_{\tau\gamma}}{A_{W\gamma}})}{A_{W\gamma}\times\epsilon\times\epsilon_{vetoW\gamma}\times(L_1\epsilon_{L1^1}\epsilon_{L2^1}+L_2\epsilon_{L1^2}\epsilon_{L2^2}+L_3\epsilon_{L1^3}\epsilon_{L2^3})^2}\times(\epsilon_{L2^1}L_1)\\
&-\Delta\epsilon_{L2^1}\times\frac{(N-N_{Wj}-N_{leX})\times(1-\frac{R_{\frac{Z\gamma}{W\gamma}}\times A_{Z\gamma}\times\epsilon_{vetoZ\gamma}}{A_{W\gamma}\times\epsilon_{vetoW\gamma}}-\frac{B_{\tau\to\mu}\times A_{\tau\gamma}}{A_{W\gamma}})}{A_{W\gamma}\times\epsilon\times\epsilon_{vetoW\gamma}\times(L_1\epsilon_{L1^1}\epsilon_{L2^1}+L_2\epsilon_{L1^2}\epsilon_{L2^2}+L_3\epsilon_{L1^3}\epsilon_{L2^3})^2}\times(\epsilon_{L1^1}L_1)\\
&-\Delta\epsilon_{L1^2}\times\frac{(N-N_{Wj}-N_{leX})\times(1-\frac{R_{\frac{Z\gamma}{W\gamma}}\times A_{Z\gamma}\times\epsilon_{vetoZ\gamma}}{A_{W\gamma}\times\epsilon_{vetoW\gamma}}-\frac{B_{\tau\to\mu}\times A_{\tau\gamma}}{A_{W\gamma}})}{A_{W\gamma}\times\epsilon\times\epsilon_{vetoW\gamma}\times(L_1\epsilon_{L1^1}\epsilon_{L2^1}+L_2\epsilon_{L1^2}\epsilon_{L2^2}+L_3\epsilon_{L1^3}\epsilon_{L2^3})^2}\times(\epsilon_{L2^2}L_2)\\
&-\Delta\epsilon_{L2^2}\times\frac{(N-N_{Wj}-N_{leX})\times(1-\frac{R_{\frac{Z\gamma}{W\gamma}}\times A_{Z\gamma}\times\epsilon_{vetoZ\gamma}}{A_{W\gamma}\times\epsilon_{vetoW\gamma}}-\frac{B_{\tau\to\mu}\times A_{\tau\gamma}}{A_{W\gamma}})}{A_{W\gamma}\times\epsilon\times\epsilon_{vetoW\gamma}\times(L_1\epsilon_{L1^1}\epsilon_{L2^1}+L_2\epsilon_{L1^2}\epsilon_{L2^2}+L_3\epsilon_{L1^3}\epsilon_{L2^3})^2}\times(\epsilon_{L1^2}L_2)\\
&-\Delta\epsilon_{L1^3}\times\frac{(N-N_{Wj}-N_{leX})\times(1-\frac{R_{\frac{Z\gamma}{W\gamma}}\times A_{Z\gamma}\times\epsilon_{vetoZ\gamma}}{A_{W\gamma}\times\epsilon_{vetoW\gamma}}-\frac{B_{\tau\to\mu}\times A_{\tau\gamma}}{A_{W\gamma}})}{A_{W\gamma}\times\epsilon\times\epsilon_{vetoW\gamma}\times(L_1\epsilon_{L1^1}\epsilon_{L2^1}+L_2\epsilon_{L1^2}\epsilon_{L2^2}+L_3\epsilon_{L1^3}\epsilon_{L2^3})^2}\times(\epsilon_{L2^3}L_3)\\
&-\Delta\epsilon_{L2^3}\times\frac{(N-N_{Wj}-N_{leX})\times(1-\frac{R_{\frac{Z\gamma}{W\gamma}}\times A_{Z\gamma}\times\epsilon_{vetoZ\gamma}}{A_{W\gamma}\times\epsilon_{vetoW\gamma}}-\frac{B_{\tau\to\mu}\times A_{\tau\gamma}}{A_{W\gamma}})}{A_{W\gamma}\times\epsilon\times\epsilon_{vetoW\gamma}\times(L_1\epsilon_{L1^1}\epsilon_{L2^1}+L_2\epsilon_{L1^2}\epsilon_{L2^2}+L_3\epsilon_{L1^3}\epsilon_{L2^3})^2}\times(\epsilon_{L1^3}L_3)
\end{aligned}
\tag{A.2}
$$

Since the errors in this expression are uncorrelated, they are added in quadrature to obtain the final systematic error. The luminosity error is a 6.5% fractional error that is kept separate from the other systematics since it is common to all DØ analyses (that require luminosity measurement), and uncorrelated to the analysis being performed.

References

1. F. Halzen and A. Martin. "Quarks and Leptons: An Introductory Course in Modern Particle Physics." John Wiley and Sons Inc., 1984.

2. B. Abbott *et al.*, "Studies of WW and WZ production and limits on anomalous WWγ and WWZ couplings,". Phys. Rev. D **60**, 072002 (1999).

3. C. J. Goebel, F. Halzen, J. P. Leveille, "Angular zeros of Brown, Mikaelian, Sahdev and Samuel and the factorization of tree amplitudes in gauge theories,". Phys. Rev D **23**, 2682 (1981).

4. T. Han, "Exact and Approximate Radiation Amplitude Zeros- Phenomenological Aspects,". International Symposium on Vector Boson Self Interactions, AIP Conference Proceedings 350, 224.

5. U. Baur, S. Errede and G. Landsberg, "Rapidity correlations in W γ Production at Hadron Colliders," Phys. Rev. D **50**, 1917 (1994) [arXiv:hep-ph/9402282].

6. P. Abreu *et al.* [DELPHI Collaboration], "Measurement of trilinear gauge boson couplings W W V, (V = Z, gamma) in e+ e- collisions at 189-GeV," Phys. Lett. B **502**, 9 (2001) [arXiv:hep-ex/0102041].

7. Heister *et al.* [ALEPH Collaboration], "Measurement of triple gauge boson couplings at LEP energies up to 189-GeV," Eur. Phys. J. C **21**, 423 (2001) [arXiv:hep-ex/0104034].

8. P. Achard *et al.* [L3 Collaboration], "Measurement of triple gauge boson couplings of the W boson at LEP," Phys. Lett. B **586**, 151 (2004) [arXiv:hep-ex/0402036].

9. G. Abbiendi *et al.* [OPAL Collaboration], "Measurement of charged current triple gauge boson couplings using W pairs at LEP," Eur. Phys. J. C **33**, 463 (2004) [arXiv:hep-ex/0308067].

10. F. Abe *et al.* [CDF Collaboration], "Measurement of W - photon couplings with CDF in p - anti-p collisions at s**(1/2) = 1.8-TeV," Phys. Rev. Lett. **74**, 1936 (1995).

11. "The DØ Detector ("The NIM paper")", FERMILAB-Pub-93/179-E (1994).

12. "The DØ Upgrade: The Detector and Its Physics", FERMILAB-Pub-96-357-E (1996).

13. "The CDF and D0 Upgrades for Run II.", Ann. Rev. Nucl. Part. Sci. **50**, 71-117 (2000).

14. K. Hagiwara *et al.*, Phys. Rev. D 66, 010001 (2002). (Specifically http://pdg.lbl.gov/2002/hadronicrpp_page2.pdf)

15. D. Lincoln. "A Large Statistics Study of the Performance and Yields of Generation-6 VLPCs (HISTE-VI)", Nuclear Physics B (Proc. Suppl.) **78**, 281-286 (1999).

16. "The DZERO Fiber Tracker Technical Design Report", (URL: `http://d0server1.fnal.gov/useres/stephan/www/CFT_TDR/CFT_TDR.ps`)

17. D. Chapin *et al.* "The DZERO Level 3 Data Aquisition System,". Proceedings from Computing in High Energy and Nuclear Physics, 2003. [arXiv:physics/0307070]

18. O. Peters, "Muon Segment Algorithm", http://www-d0.fnal.gov/nikhef/muon_reco/segmentreco/

19. F. Deliot, "The Fit Algorithm in muo_trackreco", http://www-d0.fnal.gov/ deliot/fitalg.ps.

20. C. Clement *et al.*, "MuonID Certification for p14", DØ Note 4350, 2004.

21. L. Cevalier *et al.*, "Track Parameter Error Matrix Propagation in Matter and Magnetic Field, Error Matrices Combination,". DØNote in preparation, preliminary document available at http://www-clued0.fnal.gov/ tuchming/myprop.ps.

22. F. Fleuret, "DØ Electron/Photon Analysis Package EMAnalyze" http://www-d0.fnal.gov/d0dist/dist/packages/em_analyze/v01-02-22/doc/EMAnalyze_doc.ps

23. K. Hagiwara *et al.*, Phys. Rev. D 66, 010001 (2002).

24. G. C. Blazey *et al.*, "Run II Jet Physics,". Proceedings of the Run II QCD and Weak Boson Physics Workshop, hep-ex/0005012.

25. G. Borissov, "Ordering a Chaos or ...Technical Details of AA Tracking." http://www-d0.fnal.gov/atwork/adm/d0_private/2003-02-28/adm_talk.ps

26. A. Garcia-Bellido *et al.*, "Primary Vertex certification in p14," DØ Note 4320, 2004.

27. A. Schwartzman and M. Narain, "Probabilistic Primary Vertex Selection,". DØ Note 4042, 2002.

28. U. Bassler and G. Bernardi, "Towards a Coherent Treatment of Calorimetric Energies: Missing Transverse Energy, Jets, E.M. Objects and T42 Algorithm," DØ Note 4124, 2002.

29. EMCertification version 5.0, at http://www-d0.fnal.gov/phys_id/emid/d0_private/certification/main_v5_0.html

30. D. Whiteson. "Global Track Finding at Level 3,". DØ Note 3808, 2001.

31. U. Baur and E. L. Berger, "Probing The W W Gamma Vertex At The Tevatron Collider," Phys. Rev. D **41**, 1476 (1990).

32. D. Chapin *et al.*, "Measurement of Z$\rightarrow$ e^+e^- and W$\rightarrow$ $e^{\pm}\nu$ Cross Sections with $|\eta| < 2.3$," DØ Note 4403, 2004.

33. Private communication with P. Telford concerning PMCS charged particle parameters (note in progress).

34. Private communication with E. Nurse, concerning muon id efficiencies (note in progress).

35. A. Askew, " Parametrizing the Local Muon Resolution in p13 Data for PMCS", DØ Note 4314, 2003

36. A. Alton *et al.* "Measurement of Wγ events in D0 Run II Data,". DØ Note 4410, 2004.

37. A. Alton *et al.*, "Photon Identification for DØ Run II Data,", DØ Note 4487, 2004.

38. A. Alton, A. Askew, Y. Maravin. "Study of Zγ events in DØ Run II Data.", DØ Note 4488, 2004.

39. S. Abachi *et al.*, "Isolated Photon Cross Section in the Central and Forward Rapidity Regions in $p\overline{p}$ Collisions at $\sqrt{s}$ = 1.8 TeV". Phys. Rev. Lett. **77**, 5011, 1996.

40. U. Baur and E. L. Berger, "Probing the weak boson sector in Z gamma production at hadron colliders," Phys. Rev. D **47**, 4889 (1993).

41. Private Communication with T. Yasuda concerning likelihood calculation.